

POLITECNICO DI TORINO

MASTER's Degree Course in Aerospace Engineering - Propulsive  
System

MASTER's Degree Thesis

**Development and validation of an  
inverse method for heat transfer  
estimation in LRE-like cooling  
channels**



**Supervisors**

Prof. Sandra PIERACCINI

Prof. Miguel A. MENDEZ

Dr. Maria T. SCELZO

**Candidato**

Giada BRANDI

APRIL 2023

**POLITECNICO DI TORINO**

**MASTER's Degree in Aerospace Engineering -  
Propulsive System**



**MASTER's Degree Thesis**

**Development and validation of an inverse  
method for heat transfer estimation in  
LRE-like cooling channels**

**Supervisors**

**Prof. Sandra PIERACCINI**

**Prof. Miguel A. MENDEZ**

**Dr. Maria T. SCELZO**

**Candidate**

**Giada BRANDI**

**APRIL 2023**

## Abstract

Liquid Rocket Engines (LREs) are widely used in space propulsion because of their versatility to enable frequent thrust variation maneuvers. The performance of these engines depends on the combustion chamber cooling system which generally consists of small channels manufactured on the nozzle.

At the von Karman Institute for fluid dynamics (VKI) an experimental campaign will take place to investigate the heat transfer in small cooling channels. The experiments, the working fluid and working ranges, are designed in flow similarity with the LRE cooling channels. The final aim is to investigate the effect of the augmented roughness derived by additive laser manufacturing on the cooling performances. The experimental facility, TROPIC, is a closed loop installation with capabilities of varying independently pressure, temperature, and mass flow rate of ethanol to meet the conditions required by the flow similarity. The test section is made of three transparent (quartz) sides and one metallic heated wall. The heat flux, constant and uniform, is provided by Joule effect. Since the wet surface, is not accessible, temperature measurement is performed with shielded thermocouples placed on the back of the electrified heated wall.

In this framework, the purpose of this thesis is to develop an inverse method to retrieve the heat transfer coefficient and the wet surface temperature from the transient measurement of the back wall temperature. First, the analytical 1D transient heat equation is derived with suitable boundary conditions that represent the experimental case. Then, an optimization routine is implemented to identify the mixed boundary condition at the wet wall in single phase flow and at the onset of boiling. The method is validated against FEM simulations of the single phase heat transfer case and against a small scale experiment with an air jet impinging on a heated surface.



# Summary

I razzi a combustibile liquido sono i più utilizzati, soprattutto se la spinta deve essere variata o se devono essere accesi e spenti più volte. Durante la combustione, una miscela di combustibile e ossidante viene bruciata in un involucro per produrre gas ad alta temperatura e pressione. Per ottenere una combustione stabile ed efficiente, è necessario che la camera di combustione sia circondata da canali di raffreddamento.

La maggior parte dei LRE ha punti di funzionamento in cui il propellente è in condizioni supercritiche. Se, invece, le condizioni di pressione a cui operano sono inferiori a quelle critiche, si verifica il fenomeno del *boiling*. La presenza di due fasi nel sistema può portare a un raffreddamento inefficiente e quindi alla fusione della camera di combustione. Per studiare il fenomeno in un mini canale, in similitudine di flusso con quelli di raffreddamento in scala reale, è stato costruito un nuovo impianto sperimentale (TROPIC), commissionato dall'Istituto von Karman (VKI), che ha come fluido di raffreddamento l'etanolo.

Lo scopo del lavoro di tesi riguarda lo sviluppo e la validazione di un metodo inverso da utilizzare per l'impianto TROPIC, il quale consenta di calcolare la temperatura e il coefficiente di scambio termico all'interfaccia tra la camera di combustione e i canali di raffreddamento. Il metodo si basa sull'algoritmo di ricerca diretta Nelder-Mead simplex e mira a minimizzare la norma della differenza tra la temperatura effettiva e quella calcolata con il metodo inverso, utilizzando la soluzione ottenuta dall'equazione del calore. Le soluzioni dell'equazione del calore sono state ottenute sia analiticamente che numericamente. I risultati sono stati validati da precedenti simulazioni FEM. È stato, inoltre, condotto un piccolo esperimento per validare il metodo inverso, condotto nel laboratorio J1 del VKI. Quest'ultimo utilizza come fluido un getto d'aria controllato e accelerato attraverso un ugello piano.

Alla fine, vengono illustrate le conclusioni del metodo inverso e i miglioramenti da apportare allo stesso per un successivo utilizzo ottimale sull'impianto TROPIC.

# Acknowledgements

*“Ricordatevi sempre di guardare le stelle,  
non i vostri piedi”*

- Stephen Hawking



# Table of Contents

<b>List of Tables</b>	VII
<b>List of Figures</b>	VIII
<b>List of Symbols</b>	XII
<b>1 Introduction</b>	1
1.1 Frameworks and motivations . . . . .	1
1.2 Thesis aims and methodology . . . . .	4
1.3 Thesis structure . . . . .	5
<b>2 Problem set</b>	7
2.1 Governing equation . . . . .	8
2.1.1 Dimensionless formulation . . . . .	12
2.2 Analytical solution . . . . .	13
2.2.1 Parameters sensitivity analysis . . . . .	16
2.3 1D numerical solution . . . . .	20
2.3.1 Mesh independence study . . . . .	21
2.3.2 Comparison with analytical solution . . . . .	22
2.4 Inverse method . . . . .	22
<b>3 Experimental methods</b>	25
3.1 Experimental setup . . . . .	25
3.1.1 Equipment . . . . .	25
3.1.2 Measurement techniques . . . . .	28
3.1.3 Experimental procedure . . . . .	33
3.2 Plane Nozzle characterization . . . . .	36
3.3 Uncertainty analysis . . . . .	43
<b>4 Results and validation of the inverse method</b>	45
4.1 Justification of the 1D assumption . . . . .	45

4.2	Temperature measurement improvements . . . . .	48
4.3	Validation of the inverse method with FEM results . . . . .	53
4.4	Validation of the Inverse Method with experiments . . . . .	59
<b>5</b>	<b>Conclusion and future work</b>	<b>65</b>
	<b>Bibliography</b>	<b>68</b>
<b>A</b>	<b>Analytical solution development</b>	<b>71</b>
A.1	1D PDE homogeneous with no source term and homogeneous Neumann BC's in the unit domain and IC=f(x) . . . . .	71
A.2	1D PDE homogeneous with no source term and non homogeneous Neumann BC's in non unit domain with IC . . . . .	73
A.3	1D PDE non-homogeneous with no source term and non homogeneous Neumann BC's in non unit domain with a constant IC . . . . .	75
A.4	1D PDE non-homogeneous with a constant source term, one homogeneous Neumann BC, one homogeneous Dirichlet BC in non unit domain with a constant IC . . . . .	76
A.5	pdpede Solution process . . . . .	78
<b>B</b>	<b>Calibration of instruments</b>	<b>81</b>
B.1	Hot wire calibration . . . . .	81
B.2	Validyne calibration . . . . .	82
B.3	Thermocouples calibration . . . . .	84
<b>C</b>	<b>MATLAB code</b>	<b>87</b>

# List of Tables

2.1	the table shows the eigenvalues and their bases for 10 different modes	14
2.2	Results of sensitivity study . . . . .	20
4.1	Test cases for 2D analysis . . . . .	46
4.2	FEM simulation parameters . . . . .	54
4.3	Configuration for FEM simulations . . . . .	54
4.4	Comparison between Neumann non-homogeneous bottom BC and the homogenous one . . . . .	56
4.5	Experimental results against the inverse method results in h . . . .	61

# List of Figures

1.1	Three floor TROPIC facility . . . . .	3
1.2	Test section components . . . . .	3
1.3	Test section dimensions . . . . .	4
1.4	A test case in similarity with the TROPIC facility . . . . .	5
2.1	Block diagram of the problem set . . . . .	7
2.2	Geometrical domain of the inconel bar and reference system . . . . .	8
2.3	Reference system on the inconel bar glued to the macor piece . . . . .	10
2.4	Heat fluxes on the bar . . . . .	11
2.5	Comparison of solutions between Neumann homogeneous and non-homogeneous BCs . . . . .	12
2.6	Temperature changes inside the inconel bar at different times . . . . .	17
2.7	Sensitivity analysis (in time) on $\alpha[\frac{m^2}{s}]$ . . . . .	17
2.8	Sensitivity analysis (in time) on $h[\frac{W}{m^2K}]$ . . . . .	18
2.9	Sensitivity analysis (in time) on $k[\frac{W}{mK}]$ . . . . .	18
2.10	Sensitivity analysis (in time) on $T_{amb}[K]$ . . . . .	19
2.11	Sensitivity analysis (in time) on $Q_{source}[W]$ . . . . .	19
2.12	Mesh independence study . . . . .	22
2.13	Comparison of both solutions with Neumann bottom boundary conditions . . . . .	23
2.14	Simplex algorithm scheme (source: Simplex Image) . . . . .	24
3.1	Photo of the experimental setup . . . . .	26
3.2	Scheme of the experimental setup . . . . .	26
3.3	(a) Inconel bar with cylinder of insulant ceramic and planar nozzle, (b) power supply, (c) compressed air line and regulation manometer . . . . .	27
3.4	Pressure transducer (membrane M42) and demodulator . . . . .	28
3.5	Calibration curve of pressure transducer (membrane M42) . . . . .	28
3.6	Velocity of the flow using Bernoulli's equation . . . . .	30
3.7	Type K sheeted thermocouples, with mineral internal insulation and sensing diameter 1mm . . . . .	30

3.8	Example of calibration curves for the thermocouples used in this work	31
3.9	Hot wire anemometer is the sensor used to measure the velocity of a fluid	32
3.10	Calibration curve of the hot wire anemometer	32
3.11	On the left, the LabVIEW Development Environment. On the right, the chart displayed on the user interface	33
3.12	Acquisition system used for the voltages of pressure transducer and hot wire	34
3.13	Acquisition system used for the voltage of the thermocouples	34
3.14	Thermocouples mounted on the setup	35
3.15	Temperature history measured from thermocouples	35
3.16	Flow around a finite-length cylinder (figure from [5])	36
3.17	Cork walls to prevent the re-circulation region	37
3.18	Planar jet flow from Ref. [7]	37
3.19	Nusselt number in function of the Reynolds number for different correlations	40
3.20	Discharge coefficient at different flow velocities	41
3.21	Change of the velocity over the pressure of the nozzle, for each axial distance from the exit of the nozzle	41
3.22	Experimental calculation of jet temperatures	42
3.23	On the right, the graph shows how the temperature of the flow changes as its velocity changes. On the left, the change in flow pressure with the velocity is shown	42
4.1	Geometrical domain of the reference system	46
4.2	2D solution taken at different values in the y-direction	47
4.3	2D solution taken at different values in the y-direction	47
4.4	Graphs obtained with the command Pdeplot	48
4.5	Measurement improvements setup	49
4.6	Test section schematic setup for measurement improvements	50
4.7	Flat (left) or round (right) thermocouples are used to take measurements of the back temperature	50
4.8	The insulator (macor) with (left) and without(right) air chamber	50
4.9	Temperature offset in the three thermocouple mounting system	51
4.10	Offset measurements (with the test section glued to the macor)	52
4.11	Offset measurements (with the test section not glued to the macor)	52
4.12	Offset measurements on the test section glued to the macor	53
4.13	BC scheme applied to the model used for the FEM simulations	54
4.14	Probes for heat transfer and temperature values used in the FEM simulations	55
4.15	ANSYS results Cases 1 (b) and 2 (a) of the 4.3 with NH BC	55

4.16	ANSYS results Cases 3(a) and 4(b) of the table 4.3 with NH BC . .	56
4.17	$\alpha$ values from table 4.3 . . . . .	57
4.18	Case 4: Object function value at each iteration. Initial guess values $h = 1500 \frac{W}{m^2K}$ and $\alpha = 2.8 * 10^{-6} \frac{m^2}{s}$ . . . . .	57
4.19	Case 4: Final values (shown in the table 4.3) obtained from the optimization process . . . . .	57
4.20	Case 3: Object function value at each iteration. Initial guess values $h = 1500 \frac{W}{m^2K}$ and $\alpha = 2.8 * 10^{-6} \frac{m^2}{s}$ . . . . .	58
4.21	Case 3: Final values (shown in the table 4.3) obtained from the optimization process . . . . .	58
4.22	Thermocouples arrangement to find h using direct method . . . . .	60
4.23	Back temperature values from the experimental test cases . . . . .	60
4.24	Front temperature values from the experimental test cases . . . . .	60
4.25	Scaled temperature over scaled time for experimental result of h . .	60
4.26	$\alpha$ values obtained from the experimental results after applying the inverse method . . . . .	61
4.27	Experimental h in function of u with 68% CI error bars, in comparison with inverse method prediction . . . . .	62
4.28	Experimental h in function of u with 95% CI error bars, in comparison with inverse method prediction . . . . .	63
4.29	Experimental difference between the back and macor temperature .	64
4.30	Convective heat flux 4.2 . . . . .	64
4.31	Experimental correlation between Re and Nu for the planar jet case under consideration . . . . .	64
B.1	Oscilloscope(a) and anemometer (b) . . . . .	81
B.2	Calibration nozzle . . . . .	82
B.3	Hot wire calibration curve . . . . .	83
B.4	Instruments used for the validyne calibration . . . . .	83
B.5	Validyne calibration curve . . . . .	84
B.6	Instruments used for thermocouple calibration . . . . .	85
B.7	Thermocouples calibration curve . . . . .	86



# List of Symbols

## Acronyms

VKI: von Karman Institute

FM: frequency

AM: amplitude

TROPIC: Heat Transfer Phenomena in 3D Printed Channels

## Abbreviation

BC: boundary condition

IC: initial condition

LRE: Liquid Rocket Engines

CI: confidence interval

## Roman symbols

h: heat transfer coefficient [ $\frac{W}{m^2K}$ ]

k: thermal conductivity [ $\frac{W}{mK}$ ]

Q: heat source [W]

c: specific heat [ $\frac{J}{kgK}$ ]

T: temperature [K]

x: thickness dimension of the bar [m]

y: length dimension of the bar [m]

z: width dimension of the bar [m]

$q''$ : heat flux  $\frac{W}{m^2}$

$\dot{q}$ : volumetric heat flux  $\frac{W}{m^3}$

## Greek symbols

$\alpha$ : thermal diffusivity [ $\frac{m^2}{s}$ ]

$\rho$ : density of the material [ $\frac{kg}{m^3}$ ]

## Sub and Superscripts

$\infty$ : ambient condition

M: macor

IN: inconel

$\hat{\phantom{x}}$ : scaled quantities

0: initial value

i: initial condition

f: final condition

back: related to the back side of the inconel bar glued to the macor piece

front: related to the side of the inconel bar in front of the flow

s: source

IM: inverse method

NH: non homogeneous

H: homogeneous

exp: experiment

nc: natural convection

fc: forced convection

l: left side

r: right side

# Chapter 1

## Introduction

### 1.1 Frameworks and motivations

Liquid Rocket engines (LREs) are the most widely used especially if there is a need to vary thrust or if they need to be turned on and off several times. Solid fuel rockets, once activated, cannot be turned off nor can their thrust be varied at will. Special chemical mixtures such as hydrazine, which contain fuel and comburent, are used for space flight. Conveyed into the combustion chamber, they are activated by an electrical discharge. Initially, various mixtures were used as fuels, but eventually it was determined which fuels and their comburents were most suitable. The most commonly used are the kerosene-oxygen combination (actually the most common fuel used by modern jets), hydrogen-oxygen (both in liquid form) or strongly acidic chemical propellants (very toxic). Oxygen and hydrogen are usually in liquid form at cryogenic temperatures. The advantage of cryogenic propellants is that they can also be used to cool the rocket itself. Liquid hydrogen and oxygen do not need a primer because they detonate as soon as they come into contact.

The combustion process occurs in an enclosure when a fuel mixture is activated. The product of combustion is high-temperature, high-pressure gases that seek an escape route. Resisting walls make the gases rebound. These gases discharge their energy in the opposite direction through the exhaust nozzle. If there is a bottleneck before the exhaust nozzle, the pressure in the cylinder increases and with it the thrust on the head. In firearms, the combustion chamber and barrel are made of very thick special steel to resist pressure and high temperatures. In aerospace thrusters, cooling is achieved by directing a flow of air or liquid against the outer walls of the cylinder. Rockets, on the other hand, cannot be made with excessive casing thicknesses.

The cooling circuit of the combustion chamber is a prerequisite for the safe and

reliable operation of LRE. Most liquid rocket engines operate at system pressures at which propellants is in supercritical condition, which means that there are no distinction between a liquid and a gaseous phase. On the other hand, if the operating pressure conditions are lower than the critical coolant pressure, *boiling* occurs and results in a local breakdown of the cooling efficiency. Overheating of the chamber wall may occur. This can negatively affect the stability of the engine's operation. Hence, managing the cooling performance at any operating point of the engine is a key requirement for the design of liquid rocket engines. To investigate the heat transfer phenomena in subcritical conditions, a new experimental facility has been built and commissioned at the von Karman Institute (VKI) and presented in figure 1.1. The project is called TROPIC which stands for Heat TRansfer Phenomena in 3D Printed Channels.

The facility is a closed-loop installation that works with ethanol. The line is connected to a filling tank, to the vacuum pump and to the gas nitrogen line. A centrifugal pump and a flow regulation valve are used to impose the ethanol mass flow rate. Before the test, the fluid temperature is set by means of the heater. During the experiments, the fluid temperature is further increased in the test section and then it returns to the initial conditions using the heat exchanger. The accumulator membrane deforms to accommodate the change in fluid density (specific volume).

The test section (see figure 1.2) is a rectangular mini-channel in flow similarity with typical cooling channels of an LRE, using storable propellants. A thin-walled channel floor in inconel 718 (1) is fitted to a housing (2) made of macor which is a ceramic that is both thermally and electrically insulating. This housing itself provides grooves to accommodate O-ring seals and interfaces with a glass channel section (3), which is kept in place by another brass flange (4). The length of the channel floor section is 330 mm. Electrical power to heat the floor is provided by two electrodes (5) connected to the DC power supply (16V/800A). The inlet section and outlet section (6) of the setup have been manufactured using selective laser melting (SLM). The test section is installed vertically in VKI's facility in order to minimize effects of buoyancy on the boiling behavior (for details Ref. [1]).

The channel has a cross section of  $h \times w = 3 \text{ mm} \times 12 \text{ mm}$ . In order to limit heat conduction towards the corners of the channel and the quartz side walls. To maximize the probability of boiling starting along the central axis of the channel, only a 6 mm - wide is heated floor. The rest of the channel floor is made of macor as shown in the figure 1.3. In the figure it is also possible to see that the macor provides housing for the back wall temperature measurement sensor. Since the wet wall is not accessible for direct temperature measurement, the flow heat transfer coefficient must be estimated from the back wall temperature using an inverse method.

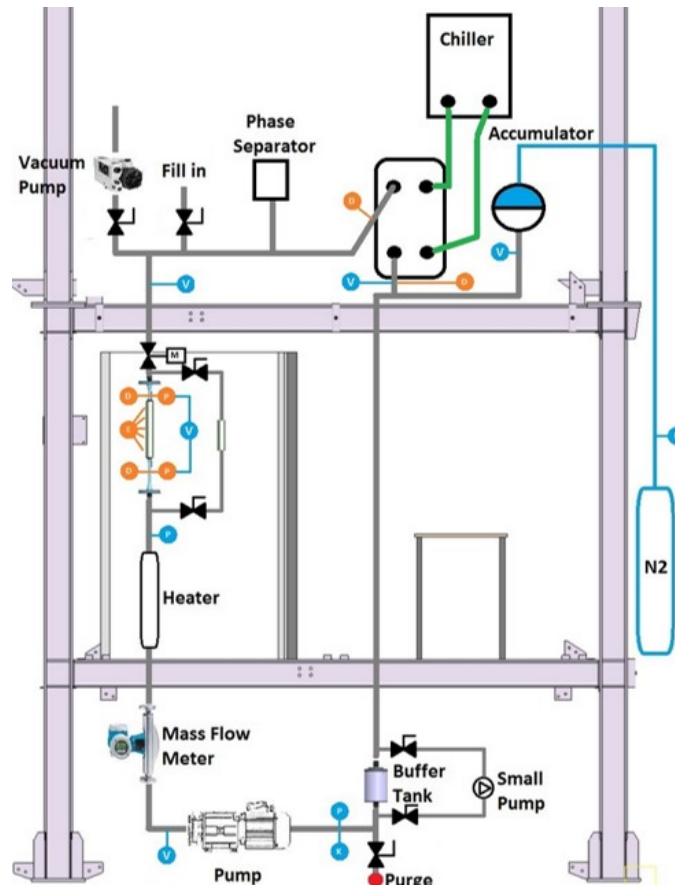


Figure 1.1: Three floor TROPIC facility

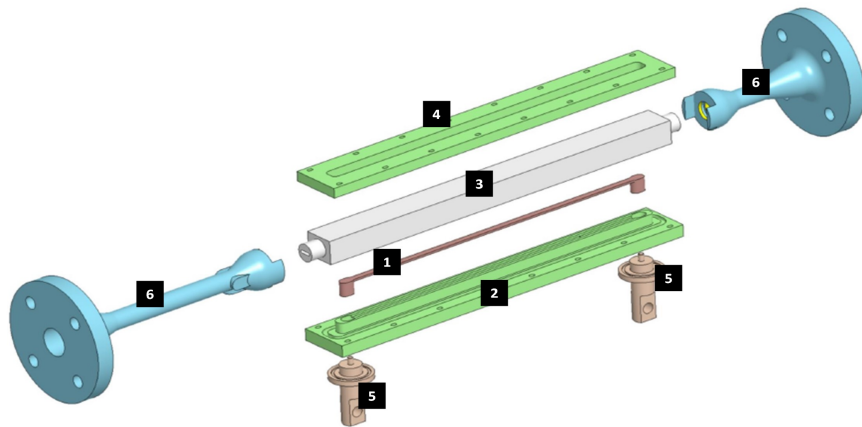


Figure 1.2: Test section components

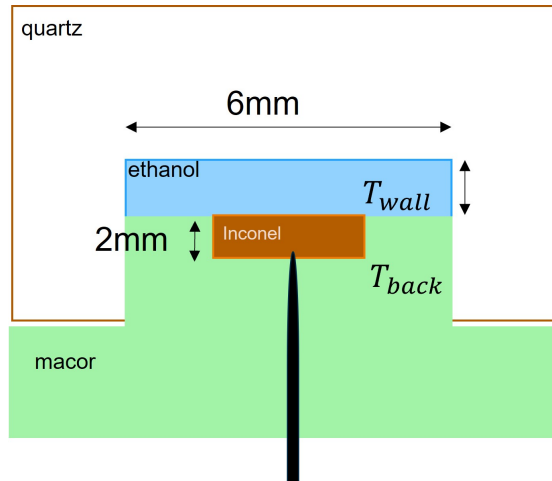


Figure 1.3: Test section dimensions

## 1.2 Thesis aims and methodology

The aim of the thesis is to develop and validate an **inverse method** for the TROPIC experimental campaign. The inverse method aims to minimize the error between the true (measured) value of temperature and the one obtained as an output of the mathematical model. The objective function to be minimized provides the heat transfer coefficient as an output variable. That links the effect (measured temperature) to the cause (the heat transfer coefficient). To validate the inverse method,  $h$  is calculated experimentally.

The mathematical model suitable for this problem is the 1D heat equation. Two different types of solutions have been studied: analytical and numerical. Both are obtained by having the dimensionless form, which provides that the code can be easily adapted for each test case. Then, a numerical solution of the 2D transient heat equation is obtained to verify that the 1D approximation is sufficient to have an acceptable solution.

Several thermocouples mounting systems have been analyzed to limit the effect of the insulant macor block on the wall temperature measurements. In an effort to reach a similarity with the TROPIC facility, a simple and controlled test case is realized. To validate the inverse method the test section is the actual inconel 718 bar and the cooling was done with a planar nozzle jet flow. The simplified model shown in the figure 1.4 consists of a planar jet nozzle that provides air cooling to the inconel bar. The bar is heated by a power supply with a constant electrical value. The goal is to estimate the front wall temperature (known also

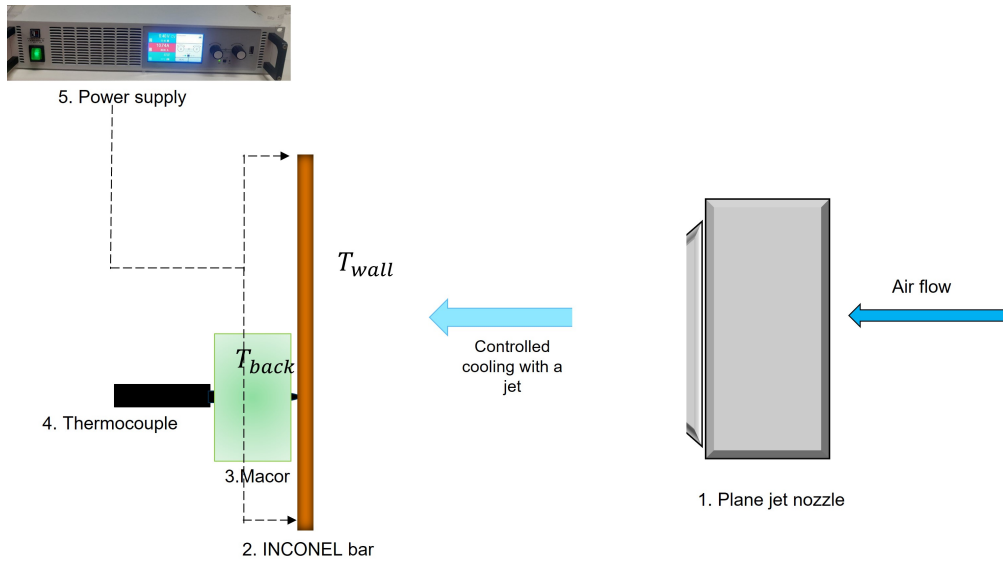


**Figure 1.4:** A test case in similarity with the TROPIC facility

as wet temperature) and the heat transfer coefficient ( $h$ ) from the back wall temperature measurement, and to compare them with experimental values. The back thermocouple is mounted onto a macor cylinder to mimic the TROPIC test section. An additional thermocouple is placed on the cooled surface to determine the heat transfer coefficient experimentally.

### 1.3 Thesis structure

The thesis is structured starting with an introduction to the problem at hand (Chapter 1) and the reasons related to the choice of dimensions, materials, and test cases.

Chapter 2 presents the mathematical formulation of the problem under consideration. It starts with an explanation of the inverse method and the governing equation of the heat flux. The Chapter presents the analytical and numerical solutions with an independence study of the numerical solution from the mesh. Then, the sensitivity of the solution to the principal variables of the heat equation is studied. In the end, the optimization method chosen for this work is explained.

In the third Chapter, the experimental facility used to validate the inverse

method is shown. It starts with a description of the experimental setup, with the necessary calibrations and characterizations. In particular, in the characterization of the nozzle, a hint of literature related to the heat transfer of planar jets on a flat surface is given. Then, the procedure used for the experiment is shown. The method used for uncertainty analysis is described at the end.

The fourth Chapter presents the analysis of the results. First of all, it discusses the improvements made to reduce the temperature measurement errors. Then, the 1D assumption is justified: the 2D solution shows that the approximation made to the one-dimensional ( $x$ ) is consistent. The heat spread in the other directions ( $y$  and  $z$ ) can be considered negligible. At the end, the validation of the inverse method is provided. first with previous FEM results and then with experiments carried out in this work.

The last chapter includes conclusions drawn from the study and future prospects.

The Appendix reports the analytical results of the heat equation, unidimensional and transient, for different BCs and ICs (A); (B) shows the calibration methods and instructions used for the instrument calibrations; and (C) reports the main MATLAB code used for the work.

# Chapter 2

## Problem set

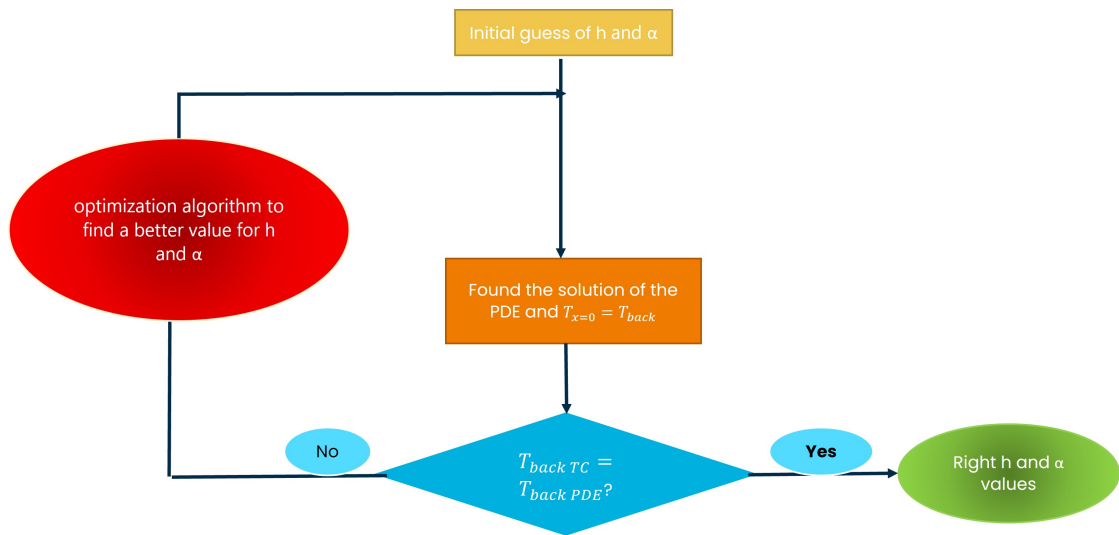


**Figure 2.1:** Block diagram of the problem set

The methodology used in this work to develop the inverse method is shown in figure 2.1. The inverse method seeks to use available information about the effect of the system to reconstruct the characteristics of the source. In practice, this is done by creating a mathematical model of the system that describes the link between the source and the output, and by using optimization techniques to determine the properties of the source that best fit the observed data.

In this work, the mathematical model is the heat equation, the source is the unknown boundary condition, i.e. the flow heat transfer coefficient and the output is the back wall temperature measurement. This chapter describes the mathematical model, its implementation and the optimization technique.

## 2.1 Governing equation

The heat equation is a partial differential equation that describes the temperature variation in time and space within a homogeneous body (see [2] for more details). With respect to the geometry shown in figure 2.2, The first law of thermodynamics

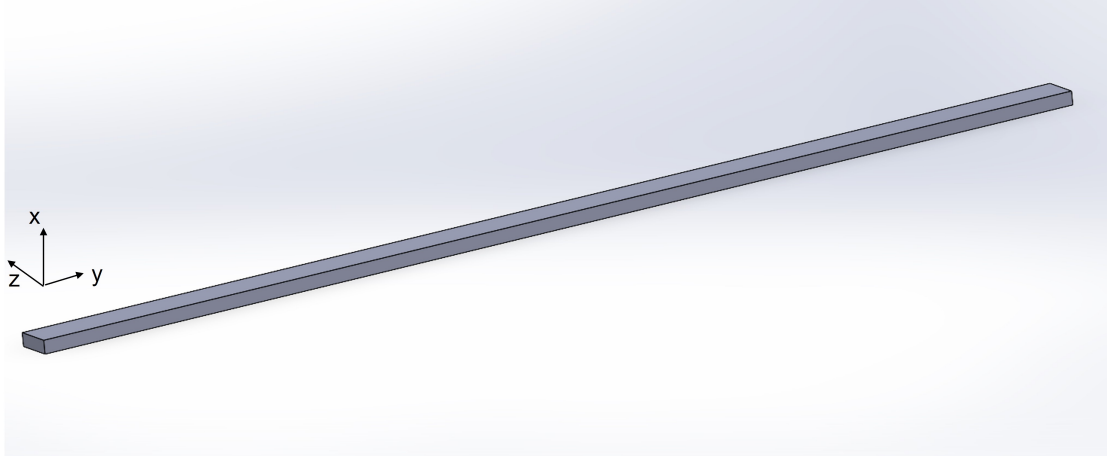


**Figure 2.2:** Geometrical domain of the inconel bar and reference system

in the x direction reads as follows:

$$q_x - q_{x+\Delta x} - L = \frac{\partial E}{\partial t} \quad (2.1)$$

where  $q_x$  is the heat transfer rate, E is the internal energy and L is the external work done on the system.

The internal energy is defined as:

$$E = (\rho S \Delta x) u \quad (2.2)$$

where  $\rho$  is the density of the solid material,  $\Delta x$  is the is a slice of the thickness of the bar, and S is the surface. In fact  $\rho S \Delta x$  is the mass of the system and u is the internal energy which is proportional to the temperature gradient:

$$du = c dT \quad (2.3)$$

where the coefficient c is the specific heat of the solid. Combining Equations 2.2 and 2.3 one could write

$$\frac{\partial E}{\partial t} = \rho S c \Delta x \frac{\partial T}{\partial t} \quad (2.4)$$

In this statement it has been assumed that the temperature variation along the bar is sufficiently small, so that the specific heat may be treated as a constant.

The work transfer rate of eq. 2.1 could be written as:

$$-L = (S\Delta x)\dot{q} \quad (2.5)$$

recognizing  $\dot{q}[\frac{W}{m^3}]$  as the volumetric rate of internal heat generation in the solid.

The third assumption made is that  $q_x$  is proportional to the local temperature difference in the x direction,  $q_x = \frac{kS}{\Delta x}(T_x - T_{x+\Delta x})$ , where  $k$  is the *thermal conductivity* of the inconel bar. In the limit  $\Delta x \rightarrow 0$ , the assumed expression for the local heat current in the x direction becomes:

$$q_x = -kS \frac{\partial T}{\partial x} \quad (2.6)$$

This is known as the **Fourier law** of heat conduction. Finally Eq. 2.6 can be used to rewrite Eq. 2.1 using the Taylor series:

$$q_{x+\Delta x} = q_x + \frac{\partial q_x}{\partial x} \Delta x = -S \left[ k \frac{\partial T}{\partial x} + \frac{\partial}{\partial x} \left( k \frac{\partial T}{\partial x} \right) \Delta x \right] \quad (2.7)$$

Hence, the first law, Eq.2.1, becomes a partial differential equation for the temperature function  $T(x, t)$ :

$$\frac{\partial}{\partial x} \left( k \frac{\partial T}{\partial x} \right) + \dot{q} = \rho c \frac{\partial T}{\partial t} \quad (2.8)$$

The first term is related to the longitudinal conduction which is the net transfer of heat. The word "net" is related to the difference between the heat that arrives by the current and the one that leaves the bar. The term  $\dot{q}$  is the internal volumetric heat generation. On the right side there is the thermal inertia which is the retarding effect. The group  $\rho c$  is the thermal inertia per unit of sample volume of the system. If the variation of temperature along the bar is small enough that the thermal conductivity may be treated as a constant, the one dimensional heat equation assumes a simpler form:

$$\frac{\partial^2 T}{\partial x^2} + \frac{\dot{q}}{k} = \frac{1}{\alpha} \frac{\partial T}{\partial t} \quad (2.9)$$

where  $\alpha = \frac{k}{\rho c} = [\frac{m^2}{s}]$  is the *thermal diffusivity* of the conducting material. It represents a measure of how fast heat moves through the material. The variables  $k, \rho, c$  are independent from the temperature, this leads to have  $\alpha$  as a constant. This assumption is confirmed in Ref. [3] which shows that the thermal diffusivity of inconel 718 varies only 4 % per kelvin degree in the range [20 - 100 °C].

The heat equation is not enough to determine the temperature profile in a conducting solid bar. In problems where the temperature field is time dependent the problem solver needs the *initial condition* (IC) and the *boundary conditions* (BC) that characterize the given heat transfer configuration.

For the present case, the imposed IC is a uniform temperature throughout the bar, equal to the ambient temperature. Instead, the BC can concern the temperature (Dirichlet BC), the heat flux (Neumann BC) or the relationship between the temperature and the heat flux (mixed or Robin BC).

In the simpler case of steady state conduction the temperature distribution depends only on the position inside the conducting body. The heat equation does not contain the transient term  $\frac{\partial T}{\partial t}$ , hence the specification of an initial condition is not required.

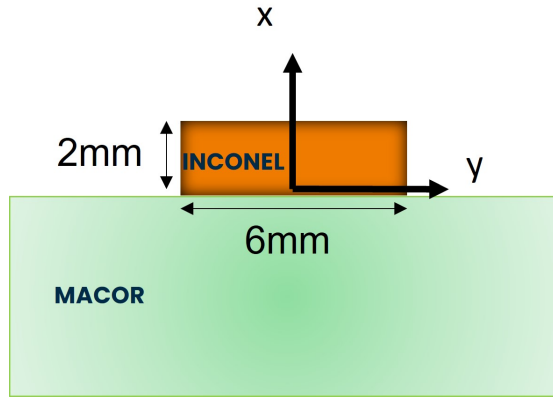


**Figure 2.3:** Reference system on the inconel bar glued to the macor piece

Figure 2.4 shows a scheme of the conductive bar that is studied in this work. The orange rectangle corresponds to the region of interest (see the cut section in figure 2.3). The boundary condition at  $x = 2 \text{ mm}$ , at the top of the inconel bar, is forced convection with the air jet (ethanol flow in the TROPIC facility) defined as:

$$-k \frac{\partial T}{\partial x} = h(T_{\infty} - T_{L_x}) \quad (2.10)$$

where  $T_{\infty}$  is the ambient temperature and instead  $T_{x=2mm}$  is the temperature of the upper wall of the bar. Convective heat transfer is the process executed by the flow which acts as a carrier for the energy that it delivers to a solid wall.

At  $x = 0 \text{ mm}$ , the boundary condition is imposed on the temperature gradient, i.e. heat flux. If the macor block is a perfect insulant material, a homogeneous Neuman condition is considered:

$$-k \frac{\partial T}{\partial x} = 0 \quad (2.11)$$

However, in this case, a non-homogeneous BC is more suitable to account for the

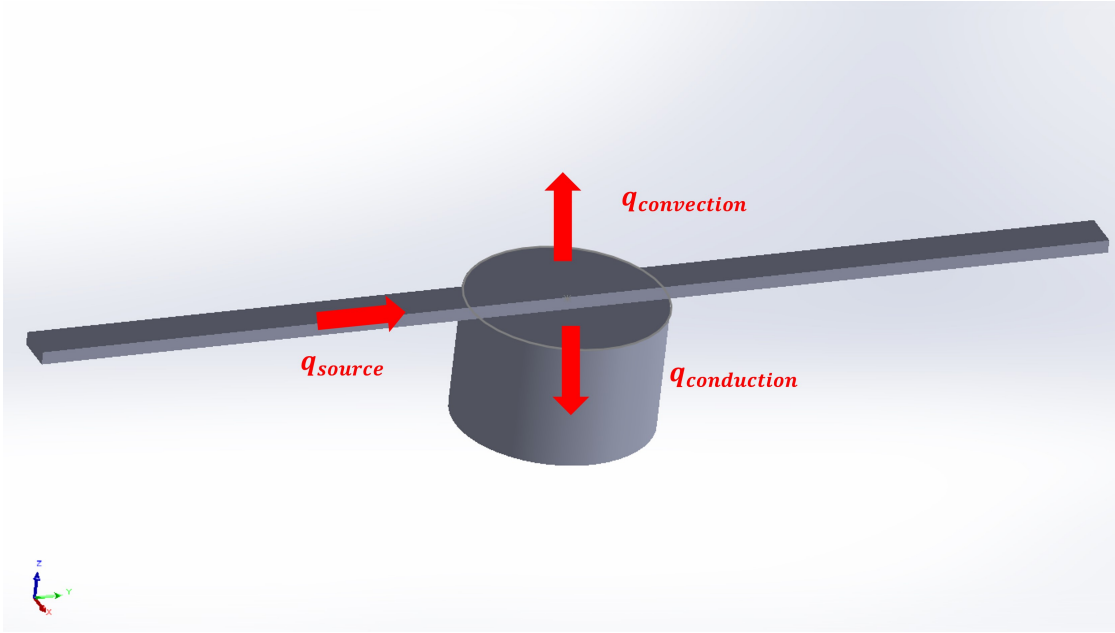


**Figure 2.4:** Heat fluxes on the bar

heat losses through the macor block ( $k_M = 1.4 \frac{W}{mK}$ ). The BC reads as:

$$-k \frac{\partial T}{\partial x} = -q''(t) \quad (2.12)$$

with:

$$q''(t) = \frac{k_M}{s_M} (T_{x=0} - T_M) \quad (2.13)$$

where  $k_M$  is the thermal conductivity of the macor piece,  $s_M$  is the thickness of the macor and  $T_M$  is the temperature at the bottom of the macor.

Figure 2.5 shows the effect of the BC at  $x = 0$  mm, on the temperature profile obtained from the equation 2.9. As expected, using a non-homogeneous Neumann boundary condition, the dimensionless temperature values are lower than in the homogeneous condition case. This is because the input heat (the source) is in both cases released by convection, while only in the non-homogeneous Neumann case, the source heat is also partly lost by conduction with the macor. So somehow having the adiabatic condition at the bottom, causes more heat to be retained by the bar rather than dissipated. It is important to highlight that the temperature values achieved are purely indicative.

The case shown in figure 2.5 is only indicative to justify the solutions obtained using two different BCs. It has approximate parameters, such as: the  $Q_{source} = 55W$ ,  $\alpha = \alpha_{IN} = 3.48e^{-6} \frac{m^2}{s}$ ,  $h = 2000 \frac{W}{m^2K}$ . The initial temperature is set at  $18^\circ C$  and the ambient temperature is set at  $17^\circ C$ .

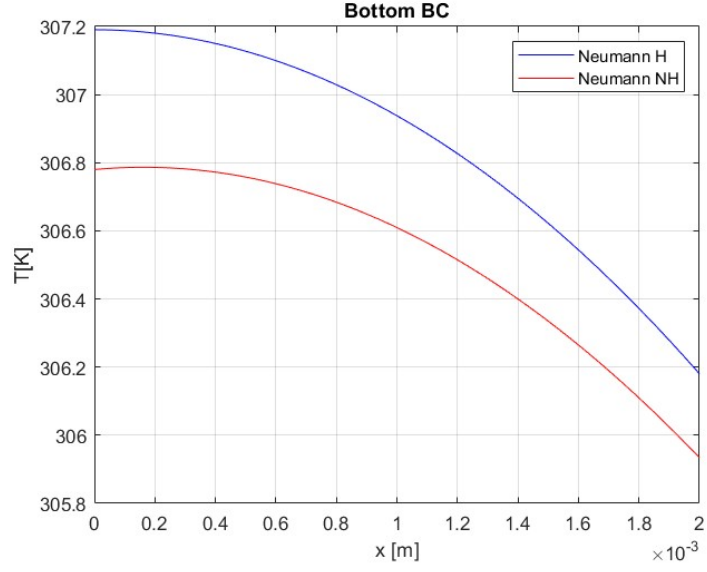


**Figure 2.5:** Comparison of solutions between Neumann homogeneous and non-homogeneous BCs

### 2.1.1 Dimensionless formulation

Eq. 2.14 summarizes the problem to be solved with its boundary and initial conditions:

$$\begin{cases} \frac{1}{\alpha} \frac{\partial T(x,t)}{\partial t} = \frac{\partial^2 T(x,t)}{\partial x^2} + \frac{\dot{q}_s}{k} \\ \left(\frac{\partial T}{\partial x}\right)_{0,t} = 0 \\ \left(\frac{\partial T}{\partial x}\right)_{L,t} = -\frac{h}{k}(T_\infty - T_L) \\ T(x,0) = T_0 \end{cases} \quad (2.14)$$

By scaling the quantities:

$$\begin{cases} \hat{x} = \frac{x}{L} \\ \hat{t} = \frac{t}{t_{ref}} \\ \hat{\theta} = \frac{T(x) - T_\infty}{\Delta T} \end{cases} \quad (2.15)$$

the system 2.14 becomes:

$$\begin{cases} \frac{1}{\alpha} \frac{\Delta T}{t_{ref}} \frac{\partial \hat{\theta}(\hat{x}, \hat{t})}{\partial \hat{t}} = \frac{\Delta T}{L^2} \frac{\partial^2 \hat{\theta}(\hat{x}, \hat{t})}{\partial \hat{x}^2} + \frac{\dot{q}_s}{k} \\ \left(\frac{\partial \hat{\theta}}{\partial \hat{x}}\right)_{0, \hat{t}} = 0 \\ \left(\frac{\partial \hat{\theta}}{\partial \hat{x}}\right)_{1, \hat{t}} = -\frac{hL}{k} \hat{\theta}(1) \\ \hat{\theta}(\hat{x}, 0) = \hat{\theta}_0 \end{cases} \quad (2.16)$$

where  $\frac{hL}{k} = Nu$  is the jet flow Nusselt number. Multiplying the equation by  $\alpha \frac{t_{ref}}{\Delta T}$  and defining the reference time as  $t_{ref} = \frac{L^2}{\alpha}$  it obtains:

$$\begin{cases} \frac{\partial \hat{\theta}(\hat{x}, \hat{t})}{\partial \hat{t}} = \frac{\partial^2 \hat{\theta}(\hat{x}, \hat{t})}{\partial \hat{x}^2} + 1 \\ \left(\frac{\partial \hat{\theta}}{\partial \hat{x}}\right)_{0, \hat{t}} = 0 \\ \left(\frac{\partial \hat{\theta}}{\partial \hat{x}}\right)_{1, \hat{t}} = -Nu \hat{\theta}(1) \\ \hat{\theta}(\hat{x}, 0) = \hat{\theta}_0 \end{cases} \quad (2.17)$$

where  $\Delta T = \dot{q}_s \frac{\alpha^* t_{ref}}{k}$ . It is worth noticing that by scaling the variables, the problem simplifies since the source term has a unit value and the Robin condition is homogeneous.

## 2.2 Analytical solution

Eq. 2.17 can be solved with the technique of separation of variables, with a solution of the form:

$$\hat{\theta}(\hat{x}, \hat{t}) = \sum_{n=0}^{\infty} X_n(\hat{x}) T_n(\hat{t}) \quad (2.18)$$

The first ODE in space is:

$$X_n(\hat{x}) = c_1 \cos(k_n x) + c_2 \sin(k_n x) \quad (2.19)$$

and then substituting the BCs:

$$\begin{cases} X'_n(\hat{x}) = -c_1 k_n \sin(k_n x) + c_2 k_n = 0 \implies c_2 = 0 \\ -c_1 k_n \sin(k_n) + c_2 k_n \cos(k_n) = -Nu c_1 \cos(k_n) \implies \tan(k_n) = \frac{Nu}{k_n} \end{cases} \quad (2.20)$$

Hence the solution reads as:

$$\begin{cases} X_n(\hat{x}) = c_1 \cos(k_n x) \\ T_n(\hat{t}) = -k_n^2 T_n(\hat{t}) + 1 \end{cases} \quad (2.21)$$

Using Galerkin projection (see Ref. [4])

$$\sum_{n=0}^{\infty} T_n(\hat{t}) \cos(k_n x) = \sum_{n=0}^{\infty} -k_n^2 T_n(\hat{t}) \cos(k_n x) + \sum_{n=0}^{\infty} 1 \cos(k_n x) \quad (2.22)$$

the solution reads:

$$T_n(\hat{t}) = \frac{q_n}{k_n^2} + b_n e^{-k_n^2 \hat{t}} = c_n e^{-k_n^2 \hat{t}}. \quad (2.23)$$

To summarize, the scaled temperature solution becomes:

$$\hat{\theta}(\hat{x}, \hat{t}) = \sum_{n=0}^{\infty} c_n e^{-k_n^2 \hat{t}} \cos(k_n x) \quad (2.24)$$

and then using the IC

$$\hat{\theta}(\hat{x}, 0) = \sum_{n=0}^{\infty} c_n \cos(k_n x) dx \quad (2.25)$$

It is important to recognize that the eq. 2.25 is a Fourier series (periodic function). The general equation (2.26) is derived from projecting the periodic function (Fourier series) onto a space of finite functions (for the present case between 0 and 1). This yields an algebraic system that can be solved numerically to find the coefficients of the series ( $c_n$ ) used to approximate the periodic function; now it is important to know that the  $c_n$ 's coefficients are **not** given by the formula as usual:

$$c_n = \frac{2}{1} \int_0^1 \hat{\theta}(\hat{x}, 0) \cos(k_n x) \quad (2.26)$$

The reason for this is that the  $k_n$ 's are not equally spaced, as shown in table 2.1, because they are the solutions of the second boundary condition shown in the system 2.20.

n	$k_n$	$b_i$
1	93.7500	0
2	1.9659e+03	-0.0154
3	3.4055e+03	0.0308
4	4.9046e+03	-0.0463
5	6.4328e+03	0.0617
6	7.9759e+03	-0.0770
7	9.5275e+03	0.0924
8	1.1084e+04	-0.1078
9	1.2644e+04	0.1231
10	1.4207e+04	-0.1384

**Table 2.1:** the table shows the eigenvalues and their bases for 10 different modes

To verify that the series is orthogonal, we must verify that the integral of the product of the bases  $b_i$  of the first ten modes is convergent to zero.

It is demonstrated that the coefficient's matrix is orthogonal but non-orthonormal so it is necessary to examine 2.25 on its own. Multiplying by  $\cos(k_m x)$  and integrating over  $[0, 1]$  gives

$$\int_0^1 \hat{\theta}_0 \cos(k_m x) dx = \sum_{n=1}^{\infty} c_n \int_0^1 \cos(k_m x) \cos(k_n x) dx$$

For  $n \neq m$  it is possible to have

$$\int_0^1 \cos(k_m x) \cos(k_n x) dx$$

by imposing  $\tan(k_n) = \frac{Nu}{k_n}$  for each of  $k_m$  and  $k_n$  lead the last equation to be identically satisfied. Therefore, when  $n = m$ , it obtains the following:

$$\int_0^1 \hat{\theta}_0 \cos(k_n x) dx = c_n \int_0^1 \cos^2(k_n x) dx \quad (2.27)$$

that leads to

$$c_n = \frac{\int_0^1 \hat{\theta}_0 \cos(k_n x) dx}{\int_0^1 \cos^2(k_n x) dx} = 4\hat{\theta}_0 \frac{\sin(k_n)}{\sin(2k_n) + 2k_n} \quad (2.28)$$

This is a general formula that works for all bases orthogonal and non-orthogonal. For the same reason there is a need to rewrite the source in terms of Fourier series:

$$1 = \sum_{n=0}^{\infty} q_n \cos(k_n x) \quad (2.29)$$

$$q_n = \frac{\int_0^1 \cos(k_n x) dx}{\int_0^1 \cos^2(k_n x) dx} = 4 \frac{\sin(2k_n)}{\sin(k_n) + 2k_n} \quad (2.30)$$

This causes the equation 2.24 to become:

$$\hat{\theta}(\hat{x}, \hat{t}) = \sum_{n=0}^{\infty} \left( \frac{q_n}{kn^2} + b_n e^{-k_n^2 \hat{t}} \right) \cos(k_n x) \quad (2.31)$$

Where:

$$b_n = c_n - \frac{q_n}{k_n^2} = 4 \frac{\sin(2k_n)}{\sin(k_n) + 2k_n} \left[ \hat{\theta}_0 - \frac{1}{k_n^2} \right] \quad (2.32)$$

The final solution comes from the equation 2.31 by substituting the equations 2.28 and 2.30.

The solution changes with the time as shown in figure 2.6 until it reaches the steady state. It can be seen that by fixing the time instant as the time equal to the end of the transient, the analytical solution match perfectly the steady state solution; while for 5 s the transition is not yet concluded so the solutions do not

match the stationary solution (see figure 2.6). It is visible that the solution reaches the steady state after 30 seconds.

In the steady state case the main equation becomes:

$$\frac{\partial^2 \hat{\theta}(\hat{x}, \hat{t})}{\partial \hat{x}^2} + 1 = \frac{\partial \hat{\theta}(\hat{x}, \hat{t})}{\partial \hat{t}} \quad (2.33)$$

integrating twice

$$\hat{\theta}(\hat{x}) = -\frac{\hat{x}^2}{2} - c_1 \hat{x} + c_2$$

Then, using the BCs it is possible to obtain the unknown coefficients ( $c_1$  and  $c_2$ )

$$\text{if } x = 0 \implies c_1 = 0$$

and

$$\text{if } x = 1 \implies c_2 = -\frac{1}{Nu} \left(1 + \frac{Nu}{2}\right)$$

Changes in the scaled solution over time is shown in the figure 2.6.

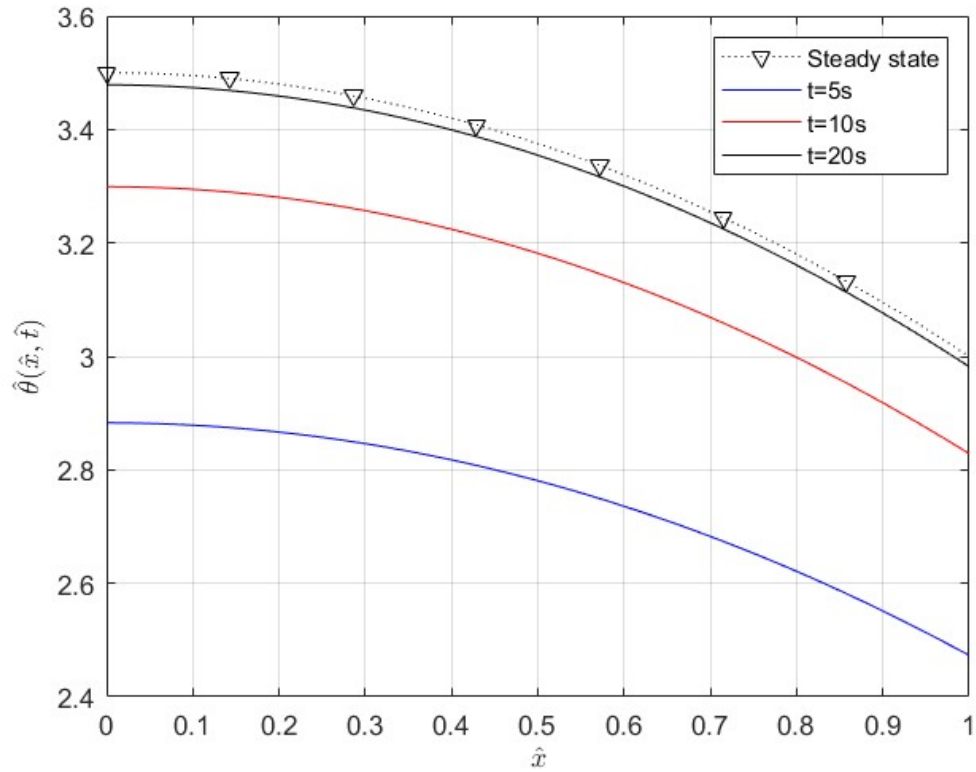
## 2.2.1 Parameters sensitivity analysis

This section shows how the solution varies as some key parameters change.

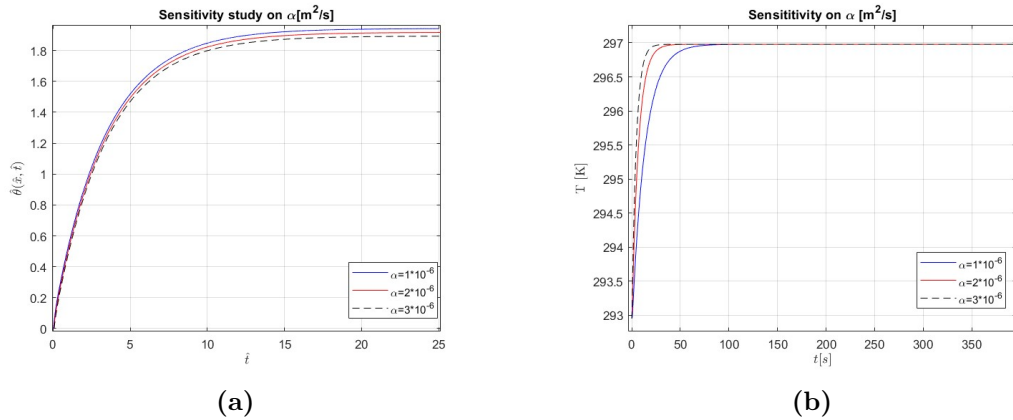
Figure 2.7 shows the effect of the thermal diffusivity on the temperature history at  $\hat{x} = 1$ . Specifically, if thermal diffusivity increases, the temperature solution diffuses more rapidly in the bar and the temperature profile flattens over time (figure 2.7a). Conversely, if thermal diffusivity decreases, heat diffusion in the bar is less efficient and the temperature solution propagates more slowly. In figure 2.7b it is possible to see that for lower  $\alpha$  values the transient time is bigger.

Figure 2.8 shows the effect of the heat transfer coefficient on the  $\hat{\theta}$  at  $T$ . In general, as the heat transfer coefficient changes, the temperature solution varies proportionally to the difference between the temperature of the surface and its surroundings (jet temperature for the case study). If  $h$  increases, the inconel top surface has a higher heat exchange with the jet, thus the surface temperature is lower (figure 2.8b).

Figure 3.15 shows the effect of the thermal conductivity on the temperature solution. If the material becomes more capable of conducting heat, the temperature solution will increase more rapidly (this could be seen from the slope of the curves shown in the figure 2.9b). Conversely, if the thermal conductivity decreases, the temperature solution will increase more slowly. In figure 2.9b it is possible to see that the transient time is not constant for all values of  $k$  chosen. This can also be



**Figure 2.6:** Temperature changes inside the inconel bar at different times



**Figure 2.7:** Sensitivity analysis (in time) on  $\alpha [\frac{m^2}{s}]$

explained by the fact that thermal diffusivity is, by definition, directly proportional to thermal conductivity; in fact, when  $\alpha$  increases the temperature values, reached

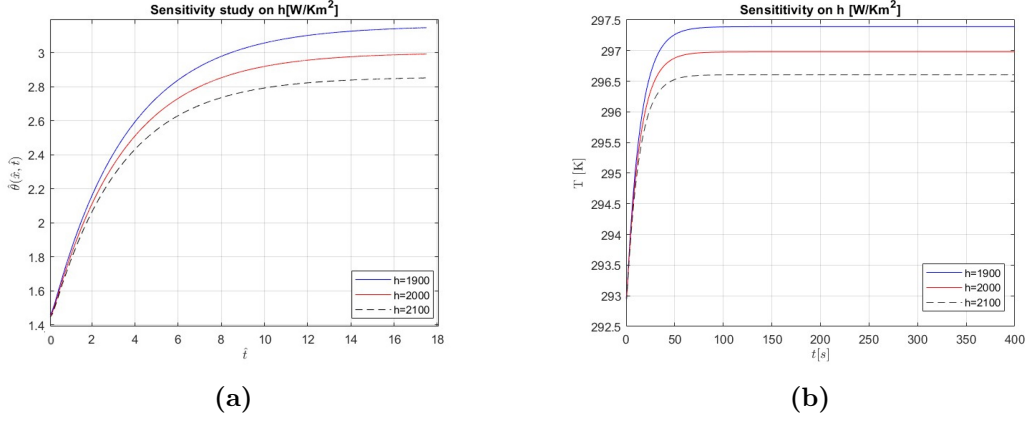


**Figure 2.8:** Sensitivity analysis (in time) on  $h[\frac{W}{m^2K}]$

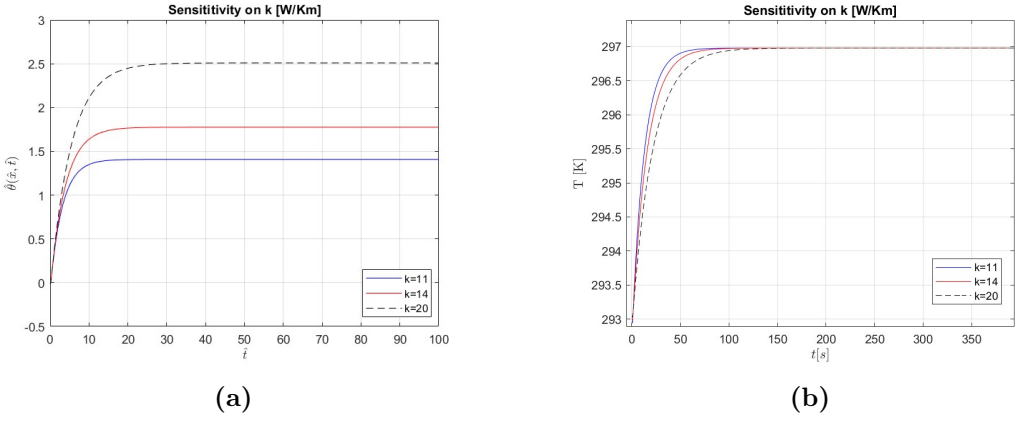


**Figure 2.9:** Sensitivity analysis (in time) on  $k[\frac{W}{mK}]$

by the top surface of the inconel bar, also increases. Equally it happens when the  $k$  increases. It is worth reminding, that in the derivation of the analytical solution of the governing equation, the thermal conductivity is not a function of temperature.

If the jet temperature increases, the solution of the heat equation will show an increase in temperature throughout the system (figure 2.10b). From the same figure it is inferred that if the jet temperature decreases, the temperature of the top surface is less because the body is cooled more. Moreover, if the jet temperature increases the difference between the initial temperature  $T_0$  and  $T_\infty$  decreases. Hence, the value of  $\hat{\theta}_0$  decreases (see the equation 2.15), is shown in figure 2.10a. In the same figure it is possible to see that when the solution reaches the steady state, the  $T_\infty$  does not affect the scaled temperature values.

The figure 2.11a draws the scaled temperature values ( $\hat{\theta}$ ) at  $\hat{x} = 1$  for different  $Q_{source}$ s. The initial time the temperature at the top side of the bar varies with the

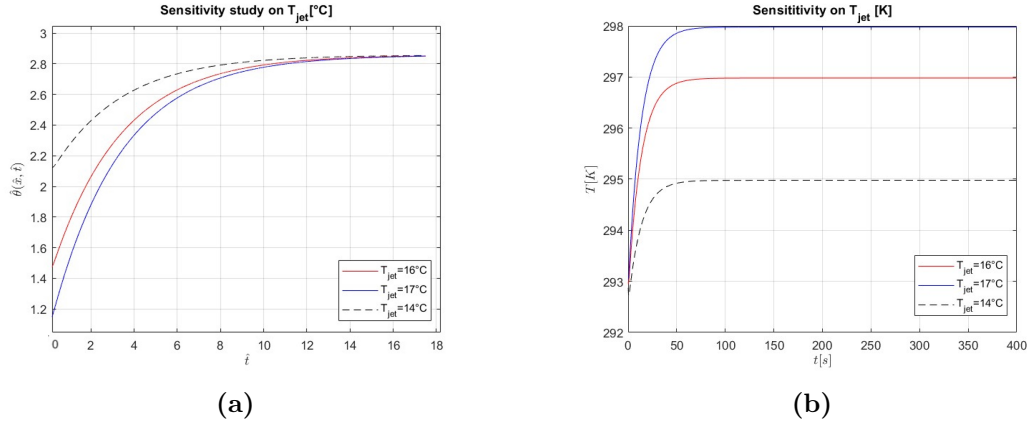


**Figure 2.10:** Sensitivity analysis (in time) on  $T_{amb}[K]$

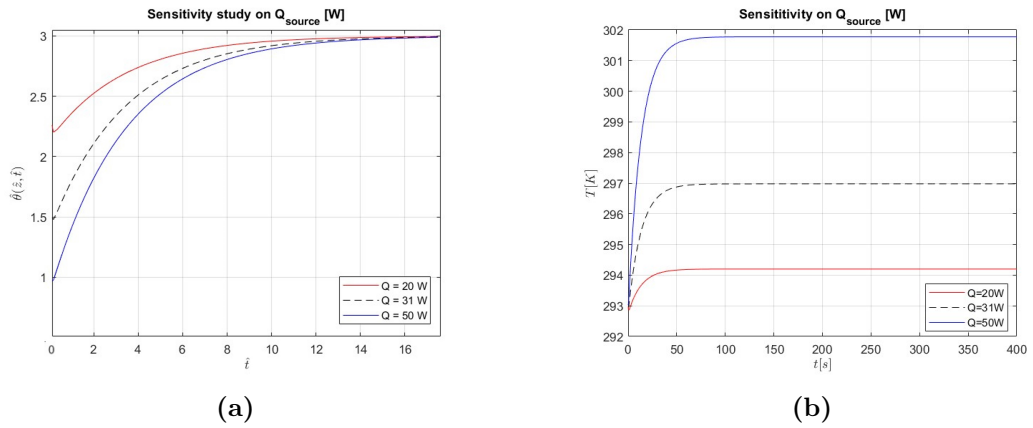


**Figure 2.11:** Sensitivity analysis (in time) on  $Q_{source}[W]$

change in the source since  $\hat{\theta}_0$  is inversely proportional to the value of the volumetric source (see the equation 2.15). In the same figure it is possible to see that the effect of  $Q_{source}$  on  $\hat{\theta}$  vanishes when the solution reaches steady state, referred to the definition of  $\hat{\theta}$ . Instead, from the figure 2.11b, the effects of  $Q_{source}$  on the final temperature are clearly visible. It is logical that a larger source allows for a higher surface temperature due to the fact that in the same time interval it gives more heat to the inconel bar. The transient time depends on the variable in question.

The summary of the sensitivity analysis is described in table 2.2. In it, it is clear that the parameter that most influences the solution is the ambient temperature. The table 2.2 presents how a 20% change in each of the parameters under consideration, corresponds to a percentage changes in the solution, expressed in terms of  $\delta T$ .

	$\Delta$ [%]	$\delta T$ [%]
$Q_{source}$	20	0.525
$T_\infty$	20	1.07
$h$	20	0.412
$\alpha$	20	$\sim 0$
$k$	20	$\sim 0$

**Table 2.2:** Results of sensitivity study

## 2.3 1D numerical solution

To verify the analytical solution is correct, a numerical approximation of the heat equation is solved. The *pdepe* function is a Matlab built-in FEM solver for PDE equations (the code is reported in the Appendix C). This function solves initial-boundary value problems in one spatial variable  $x$  and one time  $t$ .

The *pdepe* function uses a combination of spatial and temporal discretization techniques to solve partial differential equations. The function approximates the spatial derivatives of the solution using finite differences, that is, by approximating the derivative at one point as a linear combination of solution values at neighboring points. The accuracy of the solution depends on the size of the grid, i.e., the number of nodes that are used. For this work, the nodes are equally spaced, i.e. the discretization grid is uniform.

The Adams-Bashforth-Moulton method is used to discretize equations in time. It combines two methods: the Adams-Bashforth method and the Adams-Moulton method. The Adams-Bashforth method uses a multi-step formula to approximate the solution at the next instant from the solution at the previous instant. The Adams-Moulton method uses an implicit formula. Specifically, the method uses the Adams-Bashforth formula for a number of initial instants, and then switches to using the Adams-Moulton formula for the rest of the time. The Adams-Bashforth-Moulton type method is very efficient at finding the solution when it varies slowly over time. However, it can be unstable when the solution varies rapidly in time, particularly if the time step size is too large.

Once the partial differential equations have been discretized, *pdepe* solves the system of discrete equations using a numerical integration algorithm. This algorithm tries to find an approximate solution for each grid point.

The solver is designed to handle equations of the form:

$$c(x, t, u, u_x)u_t = x^{-m} \frac{\partial}{\partial x} [x^m f(x, t, u, u_x)] + s(x, t, u, u_x) \quad (2.34)$$

where  $u(x, t)$  is the solution defined within a domain  $[x_l, x_r]$  evolving in the finite time range  $[t_i, t_f]$ . Observe that the Laplacian operator can be written in Cartesian ( $m=0$ ), Cylindrical ( $m=1$ ) or Spherical ( $m=2$ ) coordinates. The coefficient  $f(x, t, u, u_x)$  is a flux term while  $s(x, t, u, u_x)$  is a source term.

The boundary conditions can be described in the form:

$$p(x, t, u) + q(x, t)f(x, t, u, u_x) = 0 \quad (2.35)$$

For the present case, the BC at  $x = 0$  mm is

$$\partial_{\hat{x}} \hat{\theta}(0) = 0$$

implemented with  $q_l = 1$  and  $p_l = 0$  in 2.35. At  $x = 2$  mm the BC is

$$\partial_{\hat{x}} \hat{\theta}(1) = -Nu \hat{\theta}(1)$$

where  $p_r = \frac{hL}{\lambda} u_r$  and  $q_r = 1$ .

### 2.3.1 Mesh independence study

A mesh independence study aims at determining the accuracy of the solution with respect to the computational grid used (mesh). It involves solving the numerical problem with different computational grids, gradually increasing the mesh resolution, and analyzing how the solution varies as the mesh density changes.

The goal of the mesh independence study is to establish the optimal computational grid for the numerical problem.

The process of studying mesh independence can be divided into three main stages:

- Different computational grids with different mesh densities are generated
- For each computational grid generated, the numerical problem is solved
- The results obtained with different computational grids are compared to each other and the discretization error is evaluated

In figure 2.12 it can be seen that the solution does not change using a mesh with 1000 uniform grid points.

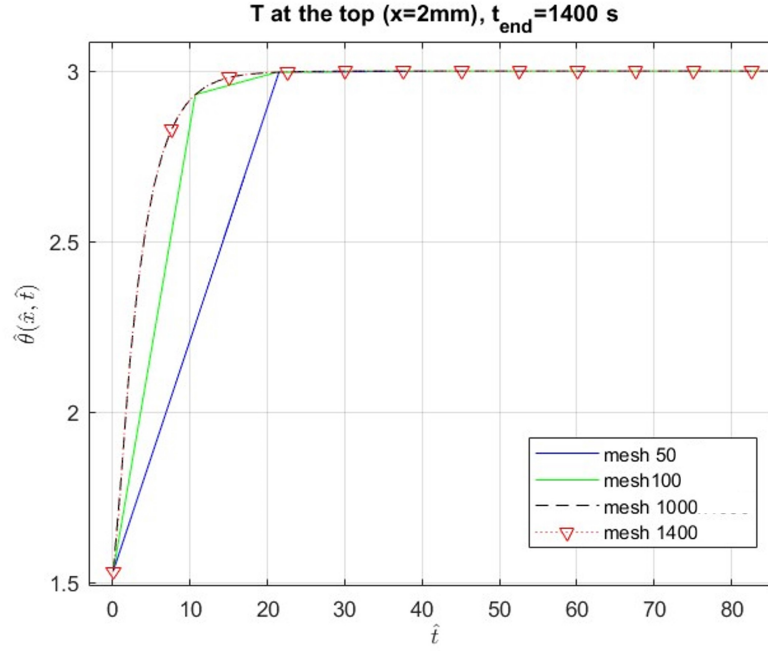


Figure 2.12: Mesh independence study

### 2.3.2 Comparison with analytical solution

Figure 2.13 shows the comparison between the analytical solution and the numerical solution obtained with 1000 grid points.

The difference is negligible. However, the computational cost of the numerical solution is twice that of the analytical one. The analytical solution has a computational time equal to 0.260239 *seconds*; instead for the numerical solution it is 0.679719 *seconds*.

## 2.4 Inverse method

It is worth reminding that in this work, the inverse method is used to retrieve the values of the heat transfer coefficient  $h$  and the thermal diffusivity  $\alpha$  of the system.

As it is shown in figure 2.1, reasonable values for the two variables are given as a starting guess to solve the heat equation. The optimization algorithm aims at minimizing the objective function  $e$  defined as:

$$e = \|T_{0,t} - T_{back}\|_2 \quad (2.36)$$

where  $T_{back}$  is the temperature history measured by the back thermocouple and  $T_{0,t}$  is the temperature at the bottom ( $x=0$ ) of the bar, found by solving the PDE.

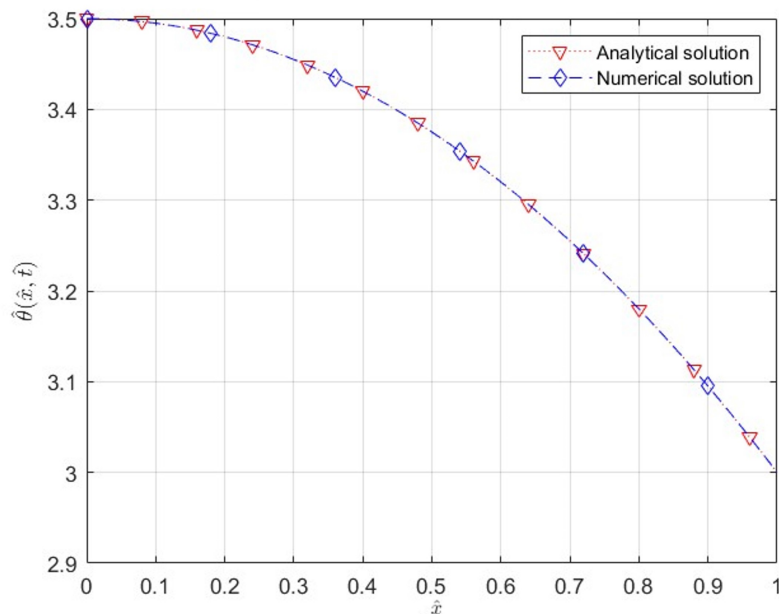


**Figure 2.13:** Comparison of both solutions with Neumann bottom boundary conditions

Once the minimum difference is found, the loop exits with two output values:  $\alpha$  and  $h$ .

The same process might be done with a simple iterative process. However this solution requires the range of the output values, which are unknown for the case at hand. Moreover, the inverse method algorithm requires evaluating the objective function many times to find the minimum, resulting in a large number of iterations for the guess value. Then, for some inverse method algorithms, such as the bisection method or the secant method, a search interval must be specified. Using a trial-and-error non-informed iterative loop to generate a search interval can be time-consuming and inefficient. In some cases, this process might lead to getting stuck in local minima instead of finding the global minimum of the objective function. For these reasons, there are more efficient and sophisticated inverse method algorithms, such as the Nelder-Mead algorithm (or Simplex algorithm) which is implement in the Matlab function *fminsearch*.

The Simplex algorithm starts with a set of points called Simplex, which contain the starting point and other points that are randomly generated near it. The algorithm then tries to move the Simplex toward the minimum of the objective function by changing the positions of the points within the Simplex iteratively.

During each iteration of the algorithm, the function is evaluated at the points

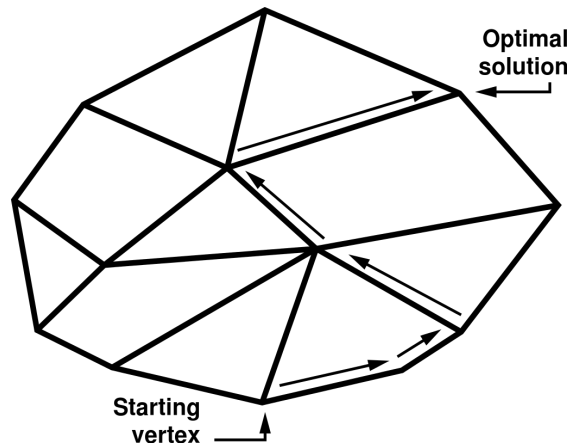


**Figure 2.14:** Simplex algorithm scheme (source: Simplex Image)

in the Simplex. Based on the evaluation results, the algorithm decides which point in the Simplex should be replaced with a new point that is closer to the minimum. This process is repeated until the algorithm finds a point that corresponds to a sufficiently low value of the function, or until the maximum number of iterations allowed is reached. Then the `fminsearch` function returns the value of the output variables. Additional options can be specified to customize the algorithm, such as the maximum number of iterations allowed, the tolerance for convergence, and the termination criterion.

# Chapter 3

## Experimental methods

The goal of the experiments is to validate the inverse method described in Chapter 2. In this Chapter, the experimental setup used in the research project is described in detail. Moreover, the measurement techniques, the calibration and characterization of all the instrumentation used and the procedure to perform the experiments are shown. At the end, the methodology for the experimental uncertainty quantification is described.

### 3.1 Experimental setup

The selected test case is a turbulent planar air jet impinging on an inconel bar, which is electrically heated.

The setup is shown in Figure 3.1 and schematically in Figure 3.2. It is composed by: the planar jet nozzle (1), the inconel bar (6), the power supply (5) and the compressed air line (8). The measurements are carried out with a differential pressure transducer (Validyne) (2), a hot wire anemometer (7) and type K thermocouples (4). The data are recorded with the National Instrument acquisition system (3).

#### 3.1.1 Equipment

To maintain the similarity with the TROPIC experiment, the test section includes the actual inconel 718 bar of dimensions 2x6x330 mm. Additionally, a cylinder of macor ceramic is glued on the bottom of the inconel bar, to mimic the insulation block of the TROPIC test section and the thermocouple mounting system (as shown in figure 3.3 (a)). The macor cylinder has a diameter of 30 mm and a thickness of 19 mm, and it is pierced to allow the back thermocouple to pass through and measure the back wall temperature. This temperature value required to apply the inverse method.

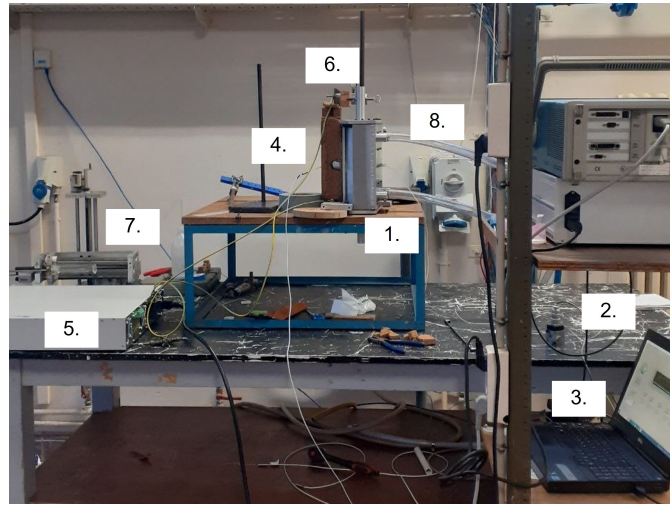


**Figure 3.1:** Photo of the experimental setup

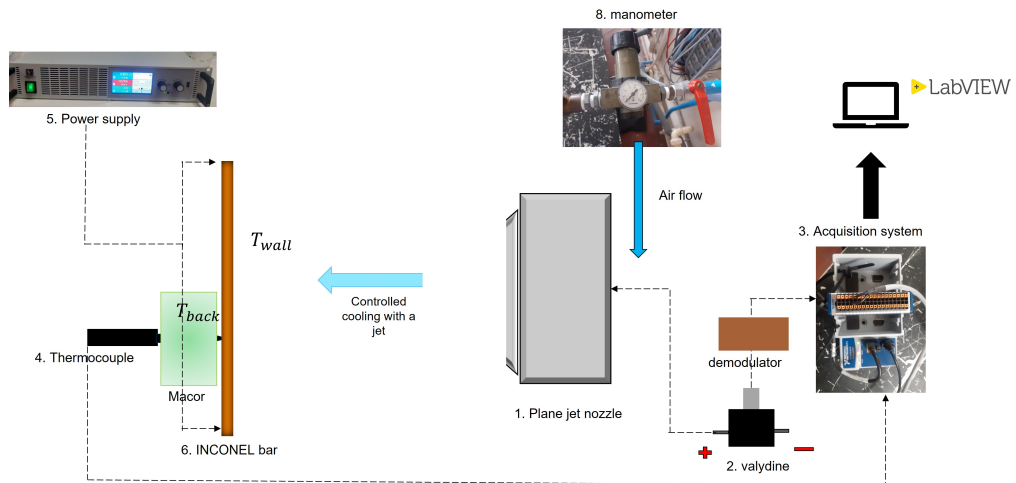


**Figure 3.2:** Scheme of the experimental setup

The bar is heated by two electrodes linked to the power supply (figure 3.3(b)) which provides constant power to the system. A power supply is an electronic device that converts incoming electrical power into the form needed to the electronic devices. The power supply has to receive an input from a source ; usually in the form of AC (alternating current) or DC (direct current) voltage. If the input power is AC voltage, it must be rectified into DC voltage. The pulsating DC voltage is then smoothed out using a filter circuit, which removes the high-frequency components of the voltage and provides a more stable DC voltage. The filtered DC voltage is then regulated to the desired level using a voltage regulator circuit.

This ensures that the output voltage of the power supply remains constant even if the input voltage or load changes. The regulated DC voltage is output from the power supply to power electronic devices or systems. The output power may be in the form of a fixed voltage or adjustable voltage depending on the design of the power supply. For the experiments of this work a power of 31 W is set, delivered with a current of 30 A.

The air jet impinging on the bar is generated by a planar nozzle (Figure 3.3 (a)). The nozzle is composed by three chambers, but for the purpose of these experiments only the central one is used. The longitudinal dimension of the nozzle is 250 mm and the width can be modified between 0 mm and 3 mm. For these experiments the width is set at 1.5 mm. Section 3.2 presents the characterization of the nozzle jet. The nozzle is fed with the 7 bar compressed air line. The air pressure is manually regulated with a valve and measured by a manometer as shown in Figure 3.3 (c). The red handle is an on-off ball valve used in emergency case or to stop the passage of the flow immediately. To set the pressure, the black knob clockwise is rotated. All the other butterfly valves on the line are kept open during the experiment to make sure that the inlet flow is regulated by the one knob that is acted on.

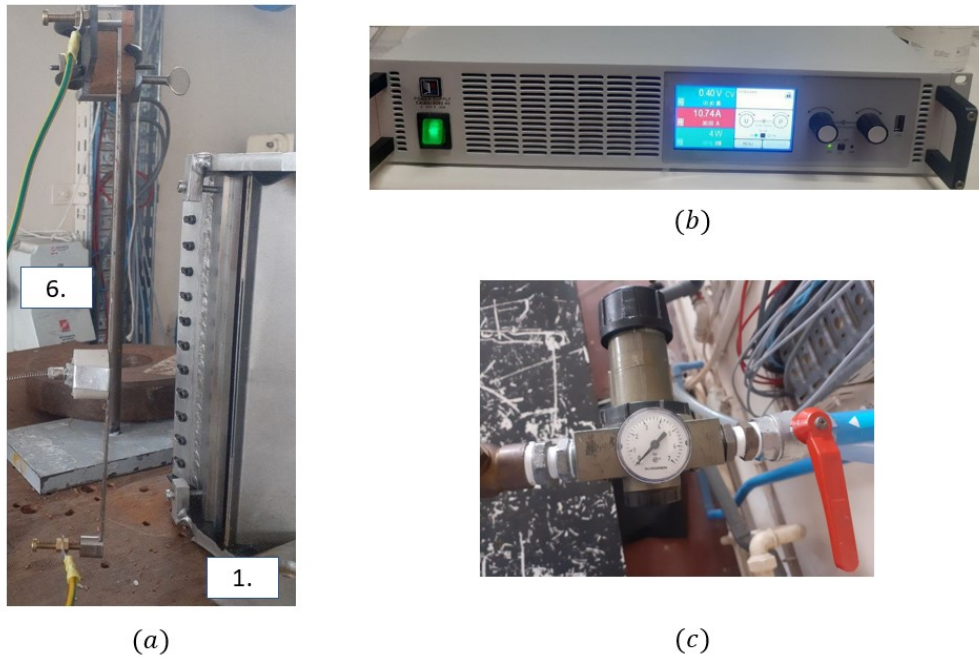


**Figure 3.3:** (a) Inconel bar with cylinder of insulant ceramic and planar nozzle, (b) power supply, (c) compressed air line and regulation manometer

### 3.1.2 Measurement techniques

During the experiments, jet pressure and velocity are measured as well as the surface temperature on the inconel bar.

#### Pressure transducer

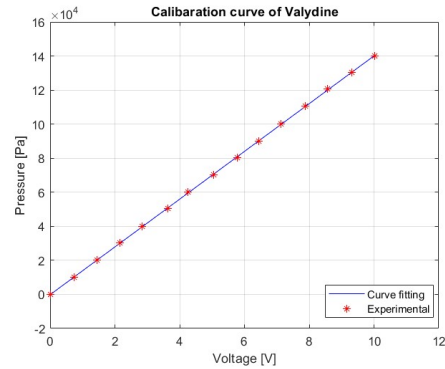


**Figure 3.4:** Pressure transducer (membrane M42) and demodulator **Figure 3.5:** Calibration curve of pressure transducer (membrane M42)

The pressure measurement device consists of a transducer and a demodulator (Figure 3.4). A pressure transducer usually consists of a membrane that flexes in response to the applied pressure, moving a sensing element, which is typically a piezoelectric crystal or a strain gauge. It generates an electrical signal that is proportional to the pressure applied to the membrane. The electrical signal is amplified and then converted into a standardized output signal, such as a 0-10V voltage signal. The standardized output signal is then transmitted to a control system, where it can be used to monitor, control, or record the pressure. The pressure sensor chosen for this experiment is a differential pressure transducer (Validyne). This transducer uses a variable reluctance sensing element, which consists of a coil of wire and a magnet. Due to the pressure difference a displacement of the membrane happens, and the distance between the magnet and the coil change. This changes the reluctance of the magnetic circuit, which in turn changes the output voltage of the coil proportionally to the applied pressure and can be measured and converted into a standardized output signal. The demodulator is an electronic component whose function is to extract the modulated voltage signal at the output of the transducer and convert it into an analog or digital signal, ready to be processed by other components of the data acquisition system. In most cases, the pressure signal that is detected by the transducer is frequency (FM) or amplitude (AM) modulated. The demodulator then has the function of

"demodulating" the signal, that is, in general restoring the original signal based on the pressure change. Overall, Validyne pressure transducers are known for their high accuracy, stability, and durability, and are used in a variety of industrial and scientific applications.

For the present experiments, the M42 membrane was chosen, which corresponds to a measurement range of 0-1.4 bar. The range of the diaphragm guarantees a safety margin, to avoid rupture. Prior to use the sensor, this has been calibrated (see the calibration curve figure 3.5) which the procedure is shown in the Appendix (B).

The calibration curve of a pressure transducer is a graph that shows the relation between the pressure applied to the transducer and the corresponding electrical output signal produced. To create a calibration curve, a known reference pressure source is applied and the electrical output is recorded and plotted against the corresponding reference pressure, as in figure 3.5. This curve should be linear, meaning that the output signal increases or decreases in proportion to the applied pressure. The accuracy of the calibration curve depends on the accuracy of the reference pressure source, the precision of the measurement equipment used to record the transducer's output signal, and the stability of the transducer over time. In general, high-quality pressure transducers have a very low measurement uncertainty, typically on the order of a few tenths of a percent of the measurement scale.

To better quantify the accuracy of the calibration the **regression coefficient**  $R^2$  is calculated. This is widely used in statistics because it provides information about the strength of the relation between the independent and dependent variables. A larger  $R^2$  coefficient, closer to one, means that the relation between the variables is well defined; so the instrument is well calibrated. A positive regression coefficient indicates that the two variables are positively related, meaning that as one variable increases, so does the other.

The equation used to find the linear regression coefficient is:

$$R^2 = 1 - \frac{\sum_{i=1}^n (y_i - \hat{y}_i)^2}{\sum_{i=1}^n (y_i - \bar{y}_i)^2} \quad (3.1)$$

where  $\hat{y}_i$  are values of  $y$  (pressure) calculated via the linear regression and  $\bar{y}_i$  is the mean of the measured  $y$ . The calibration of the pressure transducer was done very accurately in fact the regression coefficient is equal to 0.9999.

It is possible to measure the pressure through the nozzle knowing the voltage read from the acquisition system. Once the relative pressure through the nozzle is known, the Bernoulli's equation, can be used to calculate the jet velocity

$$p_e + \frac{1}{2}\rho u_e^2 = p_0 + \frac{1}{2}\rho u_0^2 \quad (3.2)$$

where the subscript  $e$  and  $0$  are respectively referred to the exit of the nozzle, which is taken as atmospheric pressure, and the inlet of it.

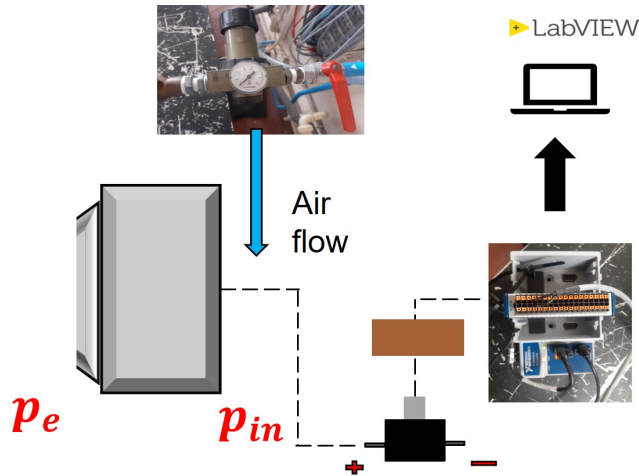


**Figure 3.6:** Velocity of the flow using Bernoulli's equation

It is possible to know the exit flow velocity using the relative pressure as an input of the Bernoulli's equation (as it is shown in figure 3.6). The velocity of the flow is also measured with another instrument, the hot wire anemometer and compared with the values taken from the Validyne. From the ratio of the two measures, it is possible to retrieve a discharge coefficient (DC). The real value of velocity is given by multiplying the velocity of the Validyne with the DC.

### Thermocouple

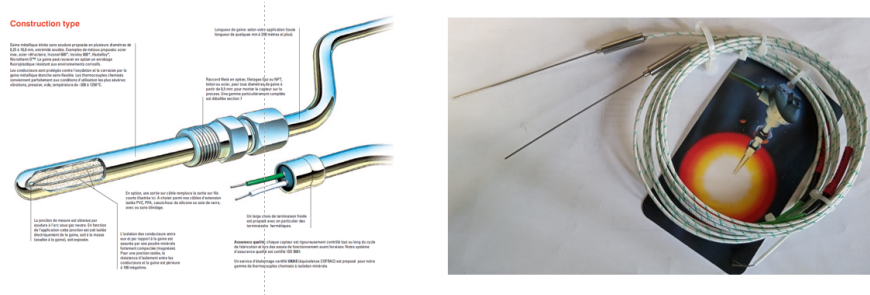


**Figure 3.7:** Type K sheeted thermocouples, with mineral internal insulation and sensing diameter 1mm

The temperature is measured with type K thermocouples shown in figure 3.7. In a Type K thermocouple, two metal alloy wires are joined at one end, while the

other one is connected to a temperature measuring device such as a voltmeter or data acquisition system. The temperature difference between both ends creates a voltage, which is proportional to the temperature difference, according to the Seebeck effect. Type K thermocouple is a temperature sensor that uses two different metals: Nickel and Chromium at the positive leg, while of Nickel and Aluminum at the negative one.

In general, standard type thermocouples (like Type K, Type J) have an uncertainty of about 0.5-1°C at normal ambient temperatures. However, the uncertainty can increase significantly at extreme temperatures or in the presence of electromagnetic disturbances. This uncertainty can be reduced by using appropriate calibration technique and ensuring controlled environmental conditions during measurements.

Moreover, a special sensor configuration is used: since the thermocouples are in contact with the electrified wall, a sheeted sensor has to be used as shown in figure 3.7. The shield is composed by a thin layer of INOX and a layer of mineral electric insulant.

The calibration of the thermocouples was performed as described in Appendix B. In this case, the measured reference temperature is provided by a PT100 and the thermocouple output is read directly in [°C], using the calibration built-in the acquisition system. Figure 3.8 shows one example of thermocouples calibration.

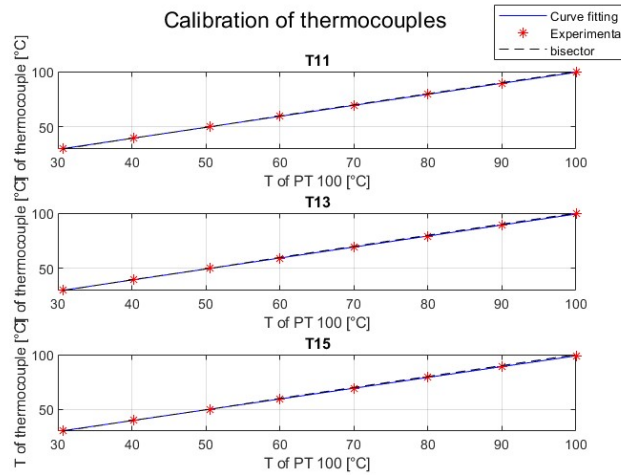


**Figure 3.8:** Example of calibration curves for the thermocouples used in this work

### Hot wire anemometer

The nozzle characterization has been performed with a hot wire anemometer.



**Figure 3.9:** Hot wire anemometer is the sensor used to measure the velocity of a fluid

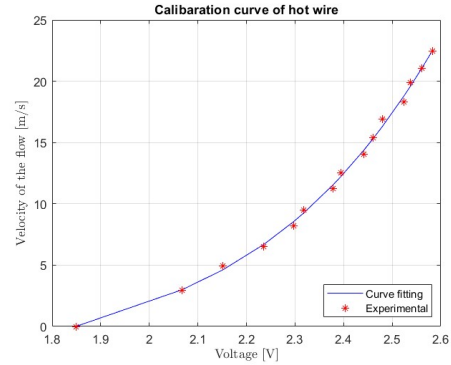


**Figure 3.10:** Calibration curve of the hot wire anemometer

A hot wire anemometer is a sensor that measures the velocity of a fluid by measuring its cooling effect on a fine wire that is heated to a high temperature using an electrical current. The wire is typically made of a material with a high temperature coefficient of resistance, such as tungsten, platinum, or nickel. It causes a cooling effect when the fluid flows over it, due to the heat transfer from the wire (hot body) to the fluid (cold one); faster velocities cause more cooling. The cooling causes a change in the resistance of the wire, which is measured using a Wheatstone bridge circuit. This circuit compares the instantaneous resistance of the wire with a reference resistance, and the difference is proportional to the velocity of the fluid. The output of the circuit is fed to an amplifier, which converts the resistance change into a voltage signal. Then, using the calibration curve, it is possible to retrieve the velocity of the fluid at each voltage.

Figure 3.10 shows the fourth-order calibration curve of the hot wire. The details of the calibration procedure are given in Appendix B. When the instrument is applied to the current case the electrical voltage signal generated by the hot wire is first measured, and then, using the calibration curve, it is possible to retrieve the real flow velocity. Then, the ideal velocity coming from the Bernoulli's equation, using the calibration curve of the Validyne. The accuracy of the measurement depends on the quality of the anemometer's calibration and on its stability over time.

## Acquisition system and LabVIEW

The data acquisition system LabVIEW is used in this work, with its graphical user interface (Figure 3.11).

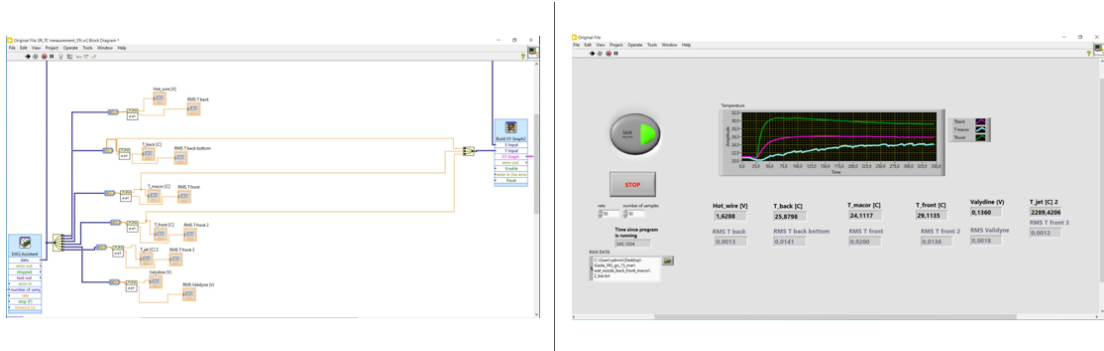


**Figure 3.11:** On the left, the LabVIEW Development Environment. On the right, the chart displayed on the user interface

LabVIEW (Laboratory Virtual Instrument Engineering Workbench) is a software platform that is used for designing and implementing measurement and automation systems. A graphical user interface (GUI) is used to create the acquisition interface by dragging and dropping elements such as buttons, text boxes, and graphs onto a virtual front panel. The acquisition can be done using LabVIEW's built-in tools for data acquisition, as well as the NI Measurement and Automation Explorer (MAX), which allows you to configure and test data acquisition hardware. The modules NI9205 and NI9212, depicted in figures 3.12 and 3.13, are used to collect voltage signals from hot wire and pressure transducer, and the temperature signal from the thermocouples. Then, the data are processed in order to extract useful information. This can be done using LabVIEW's built-in tools for signal processing, such as filters, transforms, and analysis functions. Finally, LabVIEW provides tools for visualizing and reporting data, such as graphs and charts that can be displayed on the user interface, or reports that can be generated and saved to file.

### 3.1.3 Experimental procedure

At the beginning of the experiment, the compressed air supply is connected to the nozzle central chamber. The pressure transducer has to be connected at the back of the nozzle at the plus side (as it is shown in the scheme 3.2) because it works using the relative pressure between the ambient (lower) and the nozzle (higher).

The inconel bar has to be connected to the electrodes of the power supply, which provides the voltage difference between the two ends of the bar. The inconel bar has

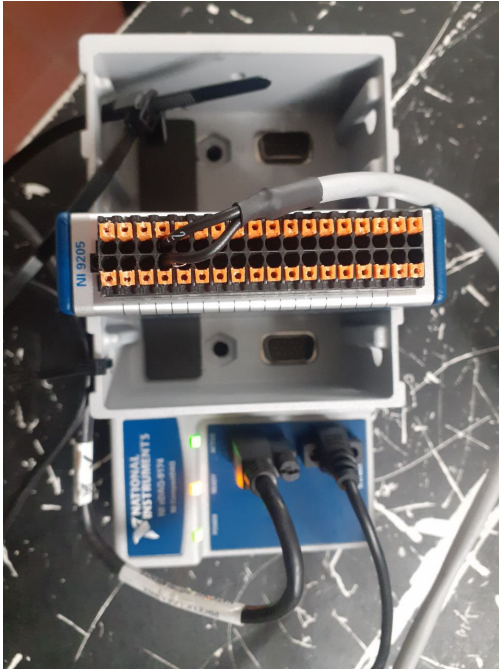


**Figure 3.12:** Acquisition system used for the voltages of pressure transducer and hot wire



**Figure 3.13:** Acquisition system used for the voltage of the thermocouples

an electrical resistivity equal to  $12.5n\Omega m$ , enabling a certain current through the bar. Thanks to the Joule effect the bar starts to heat up at a constant power. The voltage value applied to the bar, and read on the power supply, is approximately 1.3 V, which means a power of 31 W with 30 A of current. A lower amperage value would lead to a small temperature increase and a relatively higher measurement uncertainty. On the other hand, a higher value of current is not possible because of the safety limits set on the power supply.

The thermocouple used to measure the back wall temperature passes through the macor and touches the bottom of the bar. A second thermocouple is placed on the cooled wall of the inconel bar. An additional thermocouple is glued at the back of the macor cylinder to estimate the thermal losses (as explained in figure 3.14).

Before starting the experiment, the data acquisition in LabVIEW is initiated. Afterwards, the air supply is opened and the air pressure is regulated to the desired value via the manometer. Once the power supply is switched on, the temperature of the metallic bar starts to increase. The experiment lasts until the temperature reaches its steady state because the heat transfer at the end of the transient time does not change anymore. Figures 3.15a and 3.15b show typical temperature

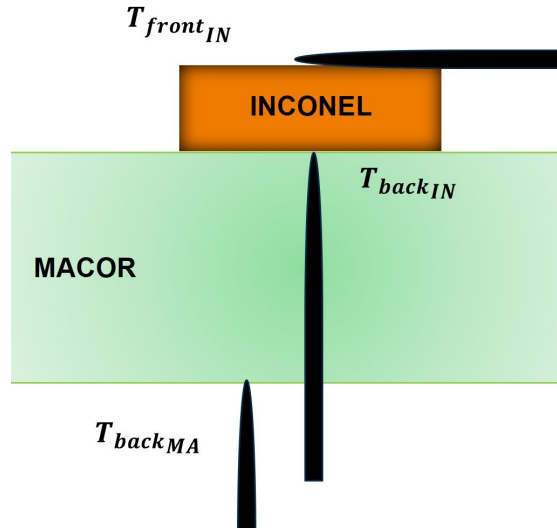


Figure 3.14: Thermocouples mounted on the setup

evolutions: it can be noticed that steady state is reached after approximately 400 seconds.

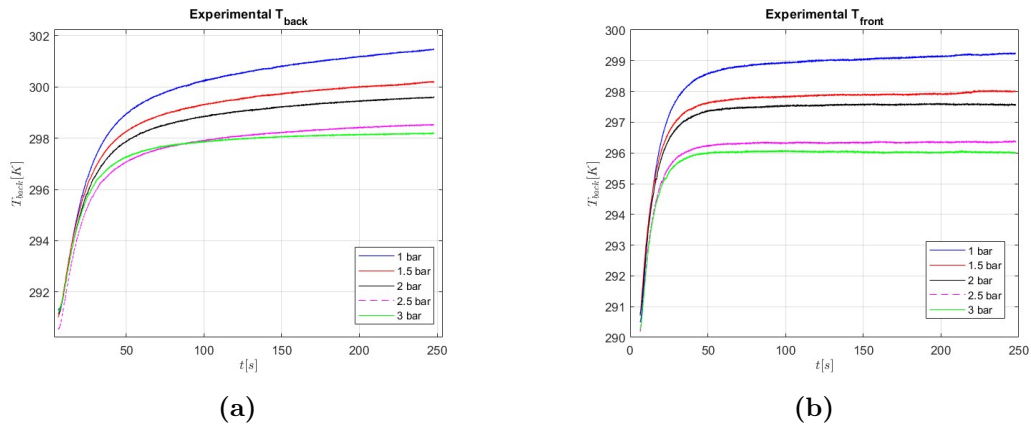
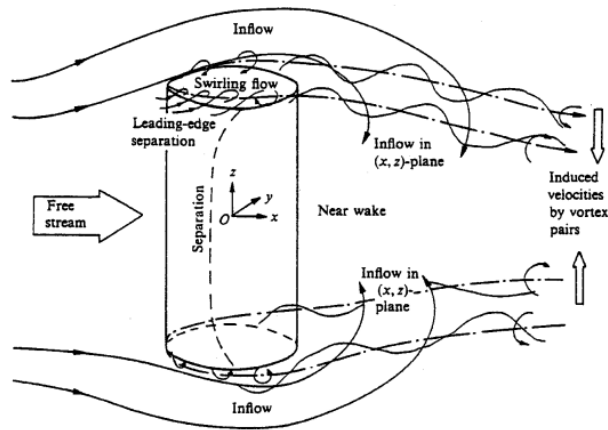


Figure 3.15: Temperature history measured from thermocouples

At the beginning of the experimental experience, the data from the back temperature history are not acquired accurately, because the flow from the nozzle passes around the inconel bar. Hence, the cooling of the back side of the setup was faster and not only related to the frontal cooling (and conduction through the bar), due to the sped-up air from nozzle. This phenomenon is known as **the bluff body problem** and it is shown in the figure 3.16.



**Figure 3.16:** Flow around a finite-length cylinder (figure from [5])

A bluff body is a solid object with a blunt, non-aerodynamic shape that is placed in the fluid stream whose velocity is to be measured. When fluid flows around a bluff body, it creates a series of alternating vortices on the downstream side of the body (see figure 3.16). These vortices are shed at a frequency that is proportional to the fluid flow velocity. The alternating vortices create pressure changes around the bluff body that can be measured using pressure sensors placed at various points in the fluid stream. The pressure changes are proportional to the frequency of vortex shedding and, therefore, the fluid flow velocity.

As it is shown in [6] and reported in the figure 3.16, behind the 3D body a re-circulation region flows around the cube. This phenomenon influences the value of temperature measured by the back thermocouple. To prevent the back of the inconel bar from being disturbed, cork walls are inserted into the test section to isolate the back of the bar from recirculating air.

As it is shown in figure 3.17, the cork is glued adjacent to the bar thickness to avoid flow separation behind the heated bar.

## 3.2 Plane Nozzle characterization

A plane jet nozzle consists of a flat orifice designed to produce a flat jet of fluid that can be used for different applications, such as cooling. The jet is typically characterized by high velocities, which can range from a few meters per second to several hundreds meters per second, depending on the pressure and flow rate of the fluid.

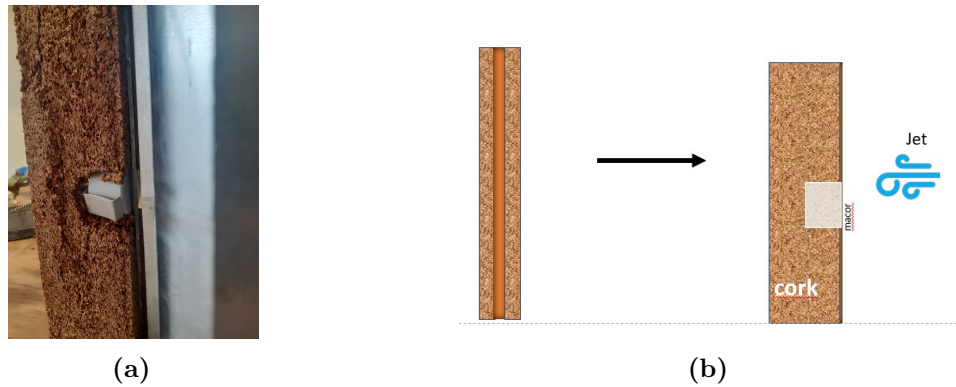


Figure 3.17: Cork walls to prevent the re-circulation region

A typical planar jet flow is shown in the figure, 3.18 where:  $y$  is the coordinate

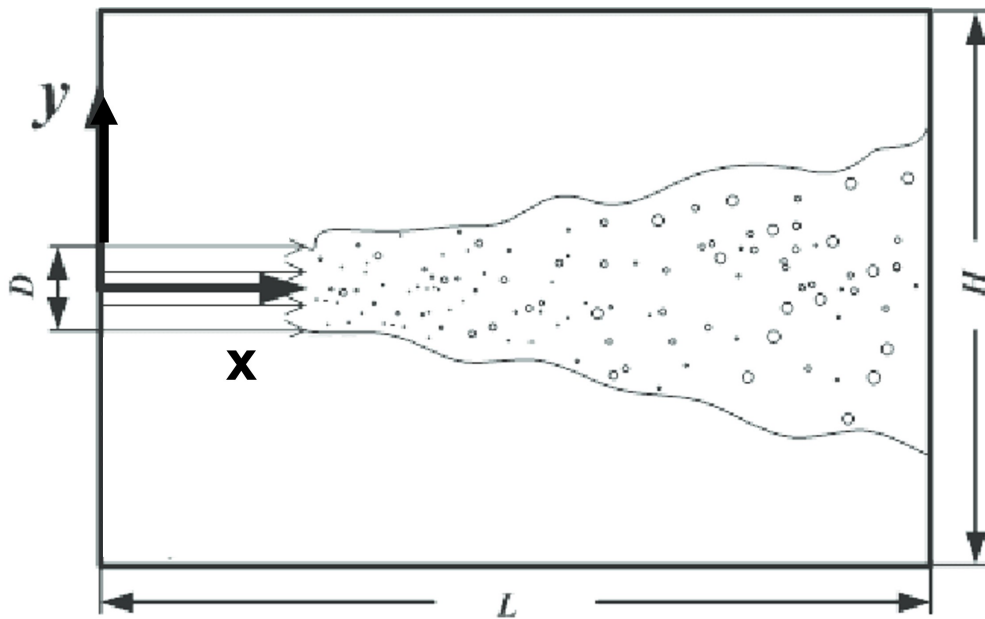


Figure 3.18: Planar jet flow from Ref. [7]

from stagnation point normal to jet axis [m];  $x$  is the distance between nozzle exit and solid surface [m];  $d_h$  hydraulic diameter of the slot ( $d_h = 2D$ ) [m];  $D$  is the width of the slot nozzle [m];  $R = \frac{y}{d_h}$  is the dimensionless radial distance from stagnation point; instead  $H = \frac{x}{d_h}$  is the dimensionless axial distance from the nozzle.

Heat transfer of impinging planar jets have been widely studied for different industrial applications. Several correlations for the Nusselt number have been developed. A list of experimental correlations found through a careful literature search is cited below.

The Ref. [8] reports

$$Nu_x = 0.569 Re_x^{1/2} Pr^{0.276} \quad (3.3)$$

where  $Re_x$  is the plate Reynolds number based on jet velocity ( $\frac{u_j x}{\nu}$ );  $x$  is the streamwise position measured from the stagnation plane. The range of applicability is  $0.7 \leq Pr \leq 10$ .

Another empirical correlation is given by Ref. [9] which reports an equation for Nusselt number in case of Single slot nozzle

$$\frac{Nu}{Pr^{0.42}} = \frac{1.53}{\frac{y}{d_h} + \frac{x}{d_h}^{1.33} + 1.39} Re^m \quad (3.4)$$

where  $m = 0.695 - \left[ \frac{y}{d_h} + \frac{x}{d_h}^{1.33} + 3.06 \right]^{-1}$ . The range of validity is for  $3000 \leq Re \leq 90000$ ,  $2 \leq \frac{y}{d_h} \leq 25$  and  $2 \leq \frac{x}{d_h} \leq 10$ . The same paper reports that for the term:  $\frac{y}{d_h} = 0$  the correction may differ from measured ones (3.4) from 45 – 50%.

From Ref. [10] the Nu is calculated as:

$$Nu = Re^{0.76} Pr^{0.42} \left[ a + b \frac{x}{d_h} + c \left( \frac{x}{d_h} \right)^2 \right] \quad (3.5)$$

where  $a, b, c$  are constant coefficients that depend on the specific case. These coefficients are:

$$a = [506 + 13.3R - 19.6R^2 + 2.41R^3 - 9.04 * 10^{-2}R^4] * 10^{-4}$$

$$b = [32 - 24.3 + 6.53R^2 - 0.694R^3 + 2.57 * 10^{-2}R^4] * 10^{-4}$$

$$c = -3.85 * 10^{-4} (1.147 + R)^{-0.0904}$$

From Ref. [11] is found that, for  $Re=12000$ , the correlation for the stagnation point is:

$$Nu_0 = a \frac{Re^{0.5}}{\left(\frac{x}{d_h}\right)^c} \quad (3.6)$$

where  $a$  and  $c$  are constant coefficients shown in Table 1 of the same Ref. [11].

Ref. [12] case seems very close to the present scenario. The correlation found by the authors is:

$$Nu = 0.09225 Re^{0.7} e^{-0.37\left(\frac{x}{d_h}\right)} \quad (3.7)$$

From Ref. [13], the following correlation is valid for  $0.7 \leq Pr \leq 3$  and is applicable to the stagnation point

$$Nu_0 = 0.7212 \epsilon^{0.4} Re^{1/2} Pr^{0.4} \quad (3.8)$$

where  $\epsilon = 1$  for a plate with a uniform heat flux as boundary condition.

Figure 3.19 show the comparison for  $Pr = 0.7579$ ,  $\frac{y}{d_h} = 0$  and  $\frac{x}{d_h} = 3.33$

It could be seen that there is a wide range of variation among the correlations, which means that each correlation is closely related to the case at hand.

An important parameter characterizing the nozzle is the **discharge coefficient (DC)**. The discharge coefficient is a dimensionless factor that relates the actual flow rate of a fluid through a pipe or an orifice to the theoretical flow rate that would occur if the fluid behaved as an ideal fluid with no friction or turbulence. The value of DC depends on various factors: the shape and size of the orifice, the Reynolds number, the nature of the fluid, and the conditions of the flow. It is typically determined experimentally and may vary from one setup to another.

The discharge coefficient can also be calculated as the ratio between the actual velocity and the velocity of the jet (known theoretically), if it behaved like an ideal fluid. The actual velocity derives from the hot wire measurements and the theoretical velocity derives from the pressure measurements via the Bernoulli's equation.

$$DC = \frac{v_{hotwire}}{v_{Validyne}} \quad (3.9)$$

The hot wire was placed in the jet core. The resulting DC is shown in the figure 3.20.

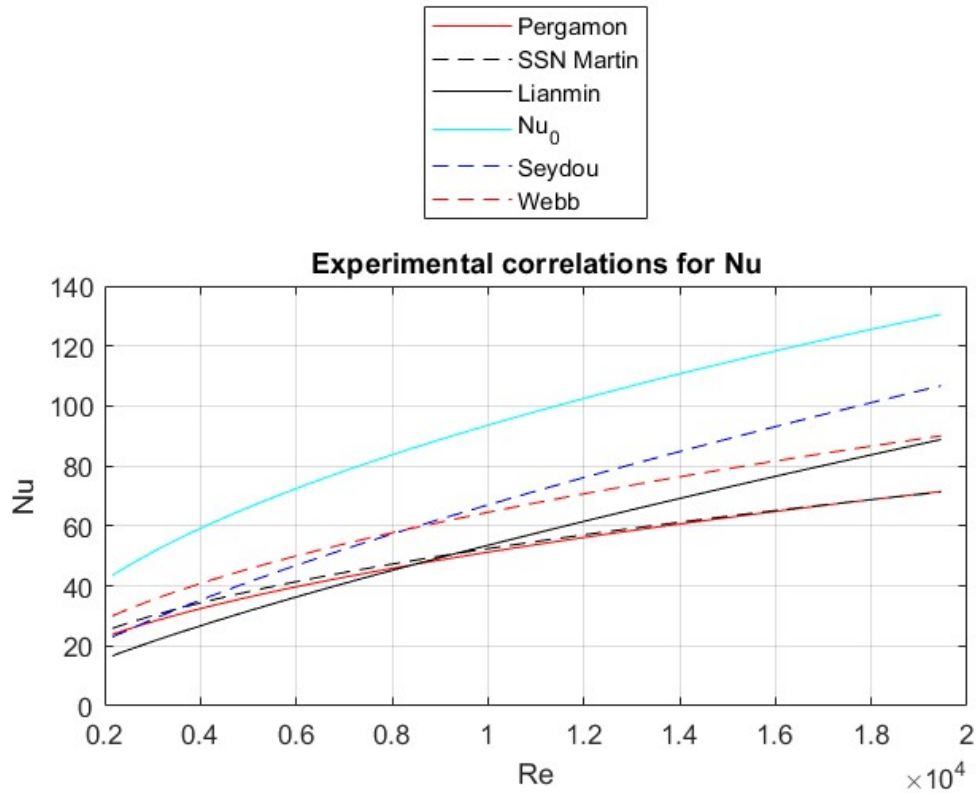


**Figure 3.19:** Nusselt number in function of the Reynolds number for different correlations

According to the literature ([7]), the jet flow is constituted by several region, as shown in figure (3.18). The core region is an area where the jet velocity is mostly constant. The core region has been identified experimentally with hot wire measurements. The hot wire is moved further downstream of the nozzle, up to 60 mm. The results are shown in figure 3.21.

It is clear that the core flow region is between the exit of the nozzle and around 5 mm away from it. This is conform to the literature which declares that the core flow region is from the exit of the nozzle to a distance less than  $H=6$ .

For high distance from the exit of the nozzle (for example see the result of the blue line at 60 mm, in figure 3.21) the velocity heavily decays between that distance and the previous measured distance (30 mm). The experiment is done putting the inconel bar into the core region at a distance of 5 mm from the plane nozzle.

For a fixed upstream pressure, it is possible to see how the flow velocity increases

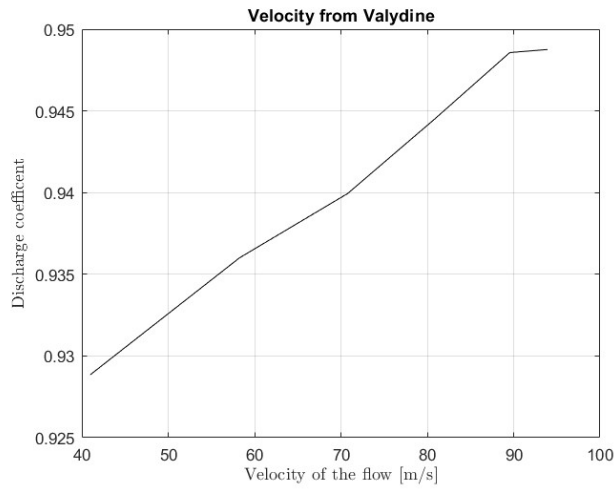


**Figure 3.20:** Discharge coefficient at different flow velocities

with the increase of the pressure of the nozzle shown in figure 3.21.

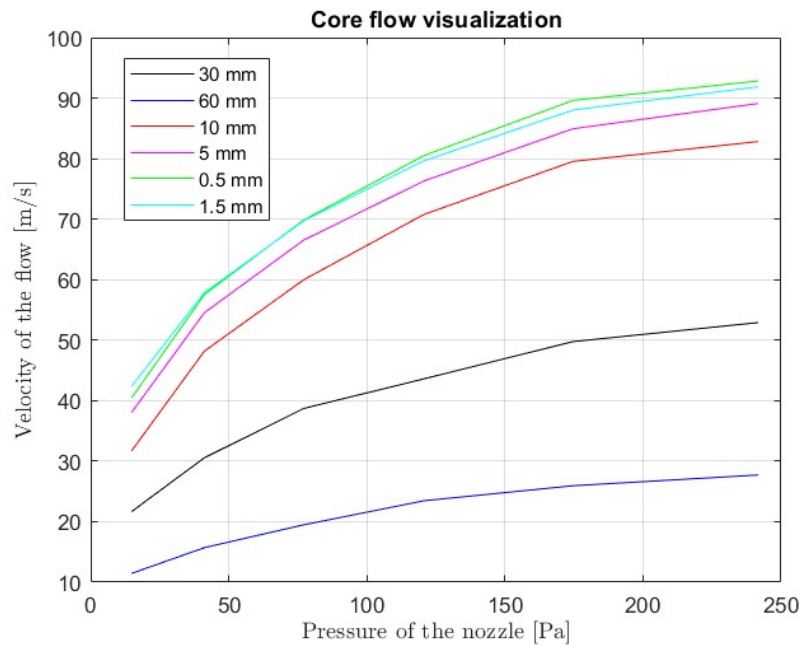


**Figure 3.21:** Change of the velocity over the pressure of the nozzle, for each axial distance from the exit of the nozzle

In order to fully characterize the nozzle, the jet temperature has to be assessed. This value becomes significantly important in the application of the Robin boundary

condition. To measure the actual temperature value of the nozzle jet, a thermocouple is applied to the center of the nozzle (see the figure below 3.22). Measurements are taken for different values of upstream pressure.



**Figure 3.22:** Experimental calculation of jet temperatures

The results of the study are shown in figure 3.23

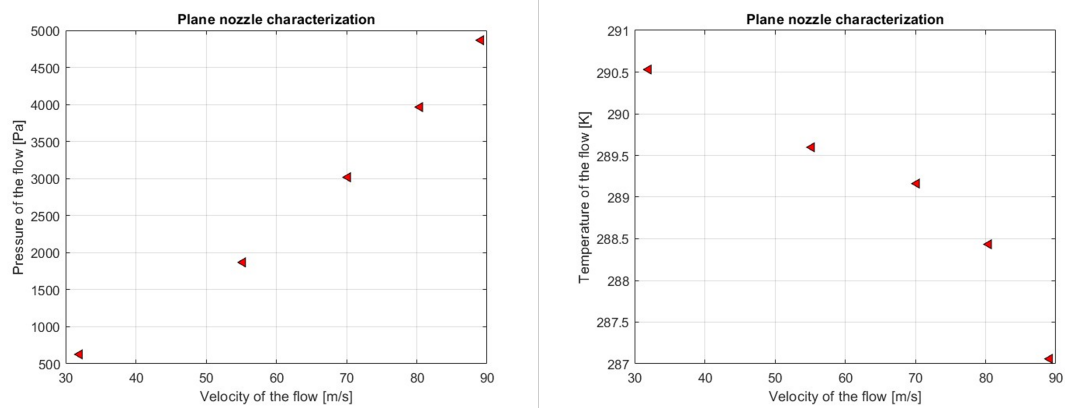


**Figure 3.23:** On the right, the graph shows how the temperature of the flow changes as its velocity changes. On the left, the change in flow pressure with the velocity is shown

The temperature and pressure of a jet depend on several factors such as velocity, density of the fluid and its composition. In general, when a jet expands, its

temperature decreases and its pressure increases, because the volume of fluid decreases; so the density of the fluid and its velocity decrease due to conservation of mass. From the kinetic energy the decrease in jet velocity leads to a decrease in temperature. Instead, the pressure increases because the momentum of the fluid must be conserved. When the jet expands, its cross-sectional area increases, which means that the same momentum must be distributed over a larger area.

### 3.3 Uncertainty analysis

It is important to include an **uncertainty analysis** on the heat transfer coefficient value found experimentally. Uncertainty analysis is a method for assessing the variability of the results of a measurement and for estimating the probability that those results are accurate. It consist in defining a mathematical or statistical model that describes the phenomenon in question and determining the uncertainties associated with each model parameter. These uncertainties are then propagated through the model to calculate the total uncertainty of the final result.

The measurement uncertainty of the power supply (Model EA-PSI 9000 DT) is found from its datasheet and it is equal to  $\pm 3.2W$ . Analogously, for the type K thermocouples with an uncertainty of  $\pm 0.5K$ .

From [14] and [15], the equation used to calculate the errors  $\sigma$  is:

$$\sigma = \sqrt{\sum_{k=1}^n \left( \frac{\partial f}{\partial x_k} \right)^2 \sigma_{x_k}^2} \quad (3.10)$$

where  $f$  is the function onto which the measurement error, is propagated  $x_k$  are the variables found experimentally and  $\sigma_{x_k}$  is the standard deviation related to the instrument used for the measurement. For the case in exam, the goal is to find  $\sigma_h$  using the equation 3.11 (reported and explained also in Chapter 4)

$$h = \frac{q_1}{T_{front} - T_{\infty}} \quad (3.11)$$

knowing the  $\sigma_{T_{front}} = \sigma_{T_{\infty}} = \pm 0.5K$ ; instead  $\sigma_{q_1}$  has to be calculated. The error of measurement on  $h$  is

$$\sigma_h = \sqrt{\left( \frac{\partial h}{\partial q_1} \right)^2 \sigma_{q_1}^2 + \left( \frac{\partial h}{\partial T_{front}} \right)^2 \sigma_{T_{front}}^2 + \left( \frac{\partial h}{\partial T_{\infty}} \right)^2 \sigma_{T_{\infty}}^2} \quad (3.12)$$

In 3.12 it is also necessary to find  $\sigma_{q_1}$  using the equations

$$q_1 = |q_s| - |q_2|$$

and

$$q_2 = \frac{k_{MA}}{s_{MA}}(T_{back_{MA}} - T_{back_{IN}})$$

(also reported in Chapter 4, equations 4.2 and 4.3). The error on  $q_1$  is

$$\sigma_{q_1} = \sqrt{\left(\frac{\partial q_1}{\partial q_s}\right)^2 \sigma_{q_s}^2 + \left(\frac{\partial q_1}{\partial T_{back_{MA}}}\right)^2 \sigma_{T_{back_{MA}}}^2 + \left(\frac{\partial q_1}{\partial T_{back}}\right)^2 \sigma_{T_{back}}^2} \quad (3.13)$$

where  $\sigma_{q_s} = \pm 3.2W$  from the datasheet of the power supply. It is worth noticing that  $k_{MA}$  and  $s_{MA}$  are considered known and constant, thus not influencing the error propagation.

## Chapter 4

# Results and validation of the inverse method

This Chapter presents the results of the work performed. First, a justification for the one-dimensional assumption is given. Then, the improvements made on the thermocouples measurement system are shown. The validation of the inverse method is pursued in two consecutive steps: a first validation with Finite Element Method (FEM) simulations and a second validation with the experimental air jet cooling results. At the end, the results from the uncertainty analysis are shown and a new experimental correlation is proposed.

### 4.1 Justification of the 1D assumption

In order to prove that the problem is one-dimensional, the 2D heat equation is solved with the Matlab model (*ThermalModel*).

Matlab's *ThermalModel* is a set of functions used for thermal modelling and it consists of two main parts: the definition of the thermal model and the thermal analysis of the system. The thermal model definition involves the creation of a one-dimensional geometry of the system in question, which includes information on the geometry, its components materials, the distribution of power dissipation, and any external heat fluxes.

The thermal analysis of the system involves using the thermal model to calculate the spatial distribution of temperature within the system at a given time.

It is important to notice that the  $x$  variable is the thickness of the bar while the direction  $z$  represents the width of the bar, and  $y$  direction is the length as indicated in figure 4.1.

The table 4.1 shows the studied cases . The first column reports the 2 dimensions

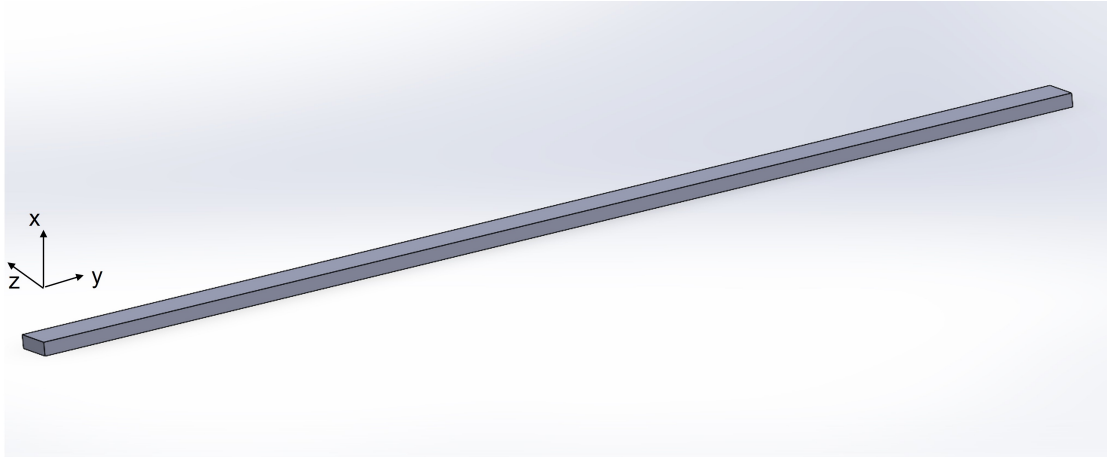


**Figure 4.1:** Geometrical domain of the reference system

2D geometry	adiabatic BC	Robin BC	1 Robin + 1 adiabatic BC
<b>330mmx2mm</b>	1a	1b	1c
<b>6mmx2mm</b>	2a	2b	2c

**Table 4.1:** Test cases for 2D analysis

under consideration: x-y and x-z plane respectively. The second and third columns refer to the symmetric BCs applied at  $z$  or  $y$  equal to 0 and 2 mm of the inconel bar. The final column refers to the non symmetric BCs applied to the same directions (alternatively) of the inconel bar.

The results are shown in figures : 4.2 and 4.3. It is noted that in the 2D solution the temperature trend is simulated for 3 points of dimension  $z$  (width of the bar). For example, let us consider case (2), in which the reference surface is 6 mm x 2 mm. The  $z$  is referred to the 6 mm dimension and the 2D solution is obtained for  $z=0$ ,  $y=Lz/2$  and  $y=Lz$ .

In both figures it can be seen that the one-dimensional assumption is realistic, since there is no considerable heat propagation in other directions, except the direction of the inconel thickness. Only in the case of figure 4.3 (case 2b). It can be seen that a very small part of heat, considered negligible, is conducted along  $z$ . In fact the temperature profiles taken along the length are not completely overlapping as in the other cases (figure 4.2). Nevertheless, the variation can be considered negligible.

This conclusion can also be reached by looking at the solution shown in figure 4.4. As it can be seen from the figure, including two Robin conditions in the 2D solution, causes the 1D and 2D solutions at the initial time to differ more than the

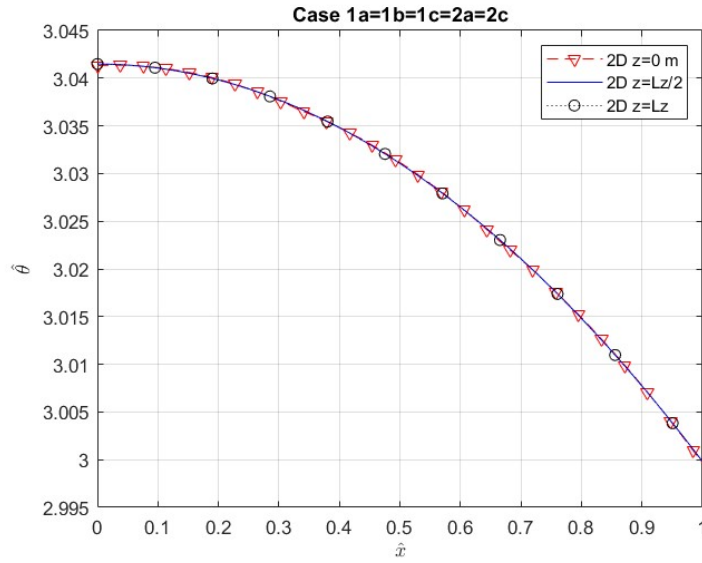


Figure 4.2: 2D solution taken at different values in the y-direction

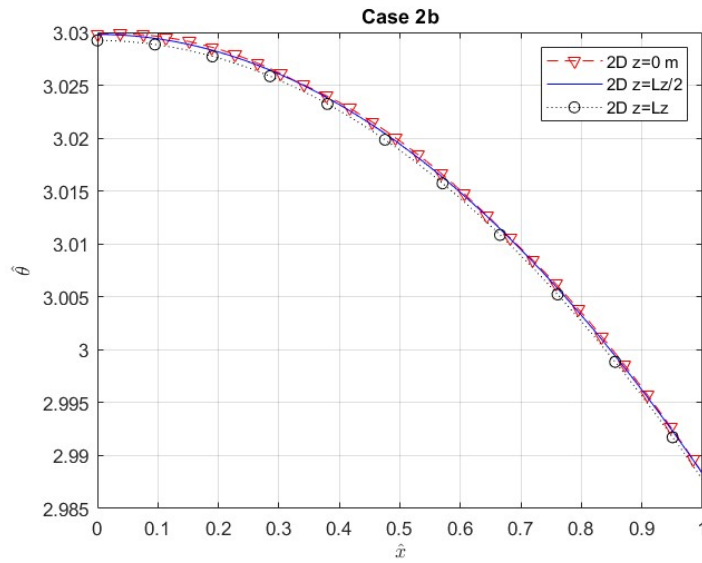


Figure 4.3: 2D solution taken at different values in the y-direction

solutions at the final time. This means that the transient of the 2D solution is faster than the one of the 1D simulation.

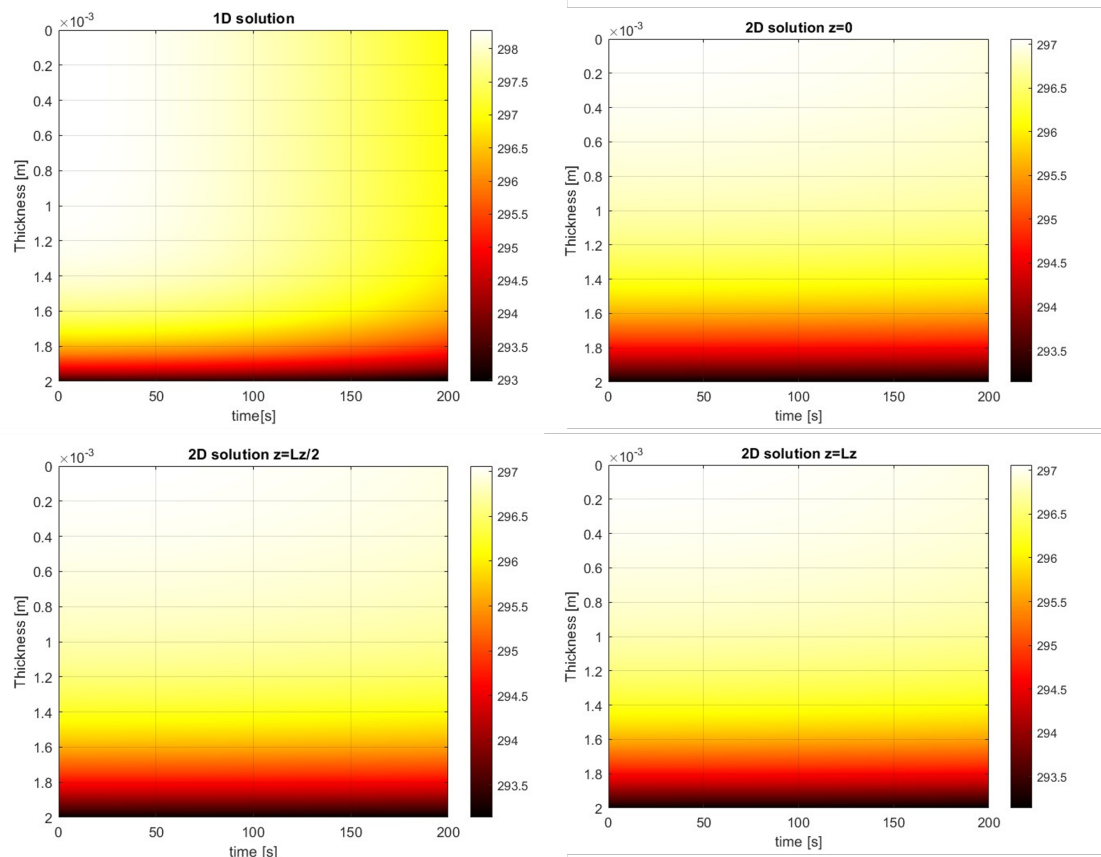
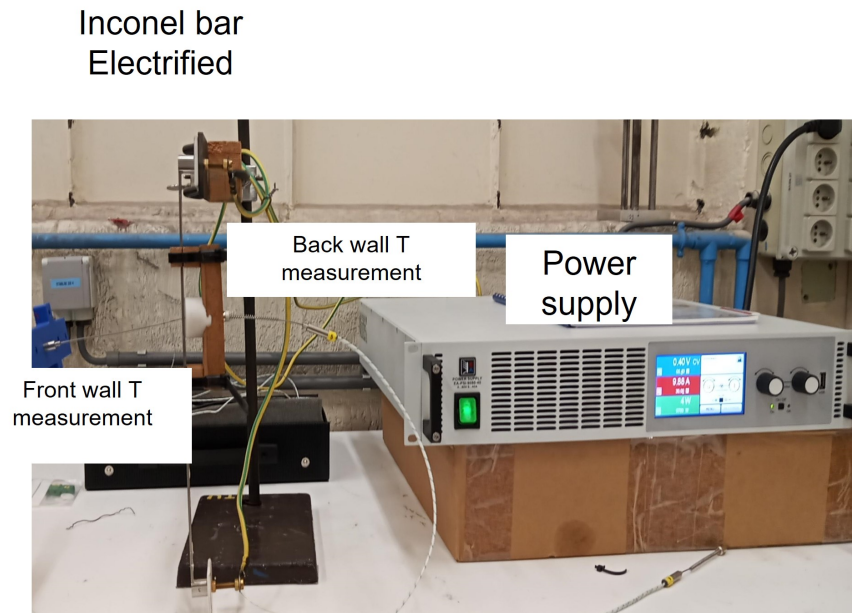


Figure 4.4: Graphs obtained with the command Pdeplot

## 4.2 Temperature measurement improvements

As mentioned earlier, having a correct measurement of back temperature is critical to the calculation of  $h$ . In the experiment under consideration, the presence of the macor negatively affects the measurement, so improvements are made in order to improve the accuracy of the measure. In this section the discussion is about the modifications made to the test section and the instrument used to take measures (thermocouple). The goal is to minimize the macor's effect.

The experimental setup is shown in figure 4.6 and partly described in the previous section. It is formed by the power supply, which generates the potential difference at the ends of the bar and generates a constant heating of the bar. Two thermocouples applied on two sides of the bar, with its acquisition system and test section. The only new instrument is the front thermocouple (see figures 4.6 and 4.5), which is intended to measure the temperature of the front wall.



**Figure 4.5:** Measurement improvements setup

In this case, the heat exchange phenomenon is not related to forced convection, but rather to natural convection. It is demonstrated that in this case the temperature profile across the bar thickness is uniform. Hence the front thermocouple and the back thermocouple should provide the same value of temperature. By placing both thermocouples at the same height on the inconel bar, it is possible to check when and how the back thermocouple measurement is affected by the macor.

Specifically, three different tests have been conducted. The difference between them is not only the change in the geometry of the macor, but also the use of two different thermocouple geometries. The geometry of the macor was modified by adding an air chamber (see figure 4.8 on the left) while the two thermocouples used for back temperature calculation differ in having a flat (see figure 4.7 on the left) or a rounded tip (see figure 4.7 on the right).

The choice of the flat thermocouple is related to the fact that in this way the instrument has a greater contact area with the surface on which temperature is measured (inconel bar).

Three different tests have been done to verify the right behaviour of the back thermocouple:

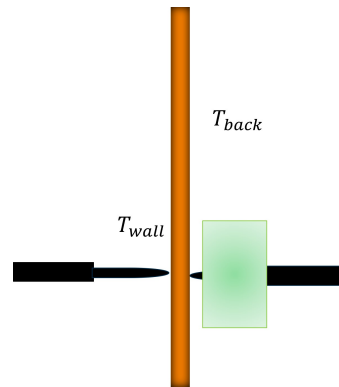


**Figure 4.6:** Test section schematic setup for measurement improvements



**Figure 4.7:** Flat (left) or round (right) thermocouples are used to take measurements of the back temperature



**Figure 4.8:** The insulator (macor) with (left) and without(right) air chamber

1. Flat thermocouple back and macor without air chamber
2. Round thermocouple back and macor without air chamber
3. Flat thermocouple back and macor with air chamber

The results of the investigation are shown in figure 4.9

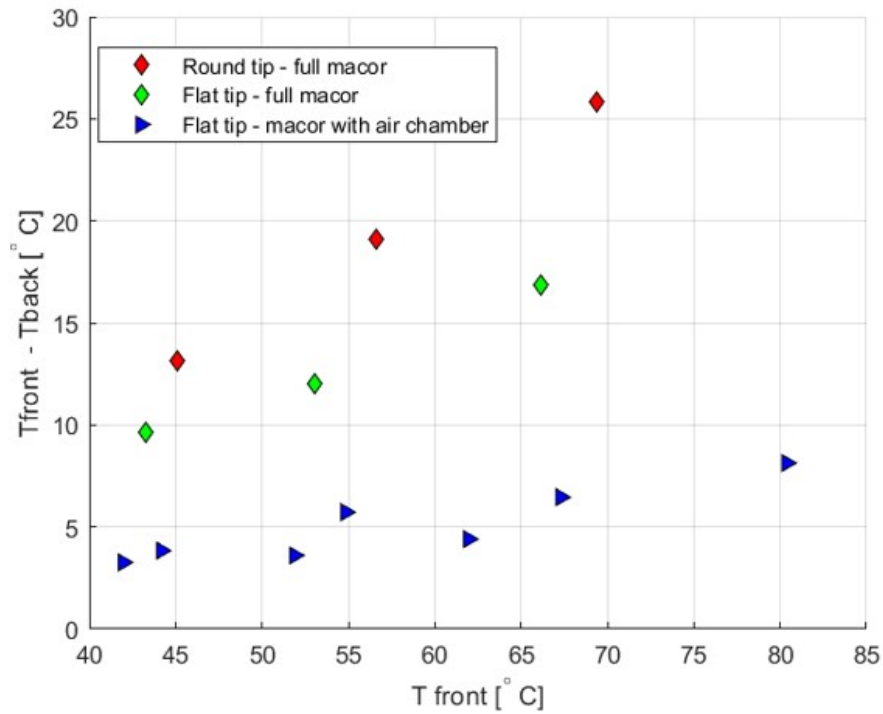


**Figure 4.9:** Temperature offset in the three thermocouple mounting system

The figure 4.9 shows the best configuration. It is the one having the macor with air chamber and using the flat thermocouple to take the measure of the back temperature. This configuration minimizes the difference between two temperatures.

Having an air chamber around an insulating piece could affect temperature measurement. This happens because still air does not conduct heat effectively. In addition, the insulating piece itself could slow down the thermocouple's response to changes in the measurement. In general, using an air chamber around the thermocouple is preferable if greater accuracy in temperature measurements is desired.

Moreover, extensive tests have been conducted to verify the effect of the glue between inconel and macor. The raw data of the experiments are shown in figures 4.10 and 4.11. The data acquired in steady state conditions are used to verify the

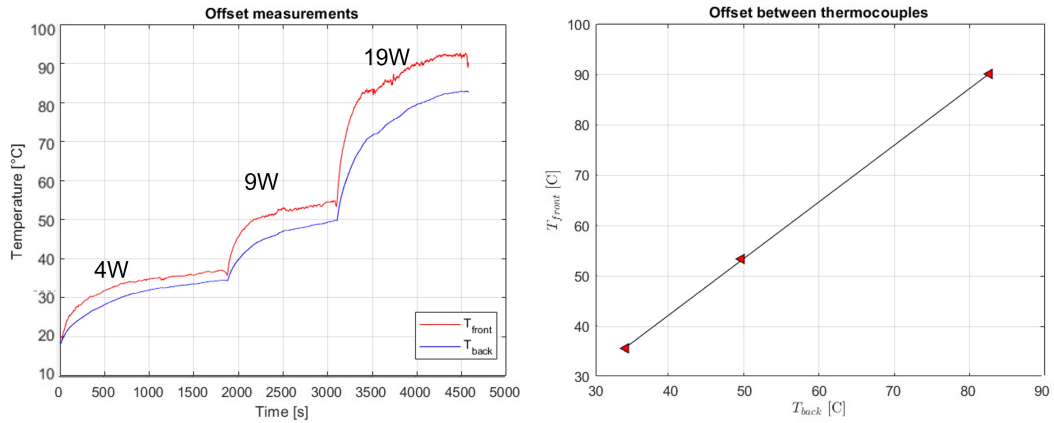


**Figure 4.10:** Offset measurements (with the test section glued to the macor)

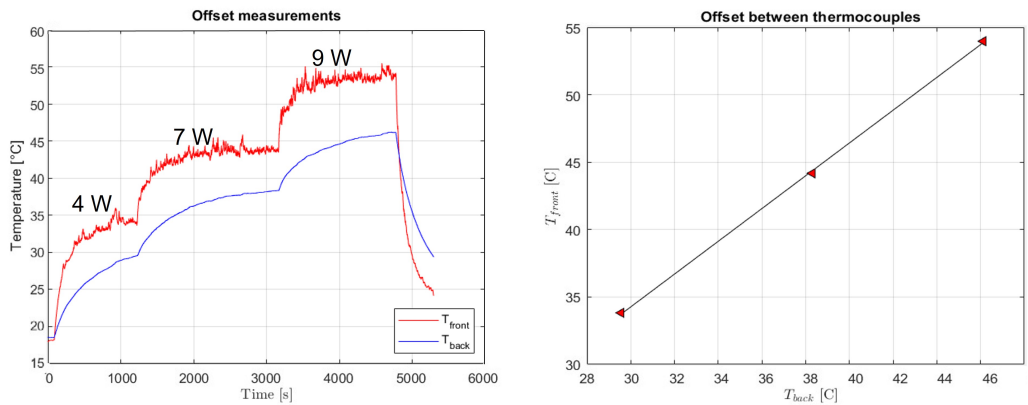


**Figure 4.11:** Offset measurements (with the test section not glued to the macor)

effect of the glue on the measurements offset.

Only steady state points (shown in figure 4.11) were used to do the interpolation, because during the transient the distance between the actual temperature and the back thermocouple is not constant. It can be observed that the slope in the first case is closer to one than the second one: this means that the measurement taken with the inconel glued to the macor is more realistic than without glue. The difference is related to fact that, in the second case, the infinitesimal air gap between the inconel and the macor allows for worse heat transfer because of the

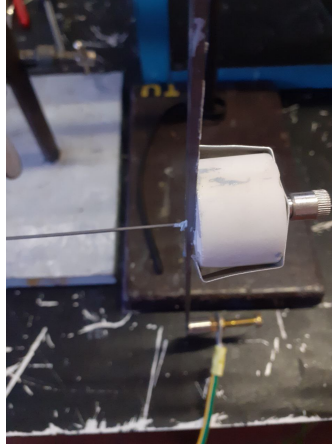


**Figure 4.12:** Offset measurements on the test section glued to the macor

thermal resistance of air. The resulting measurements in the three configurations are reported in figure 4.9 .

### 4.3 Validation of the inverse method with FEM results

The inverse method is validated with previous FEM simulations performed with the transient thermal solver of ANSYS. Table 4.2 shows the simulations parameters and the material properties for the inconel bar (subscript IN) and the macor insulant block (subscript MA). The initial temperature is  $T_0$  and the ambient temperature is  $T_{amb}$ . The heat transfer coefficient for natural convection with the environment ( $h_{nc}$ ) is taken equal to  $25 W/m^2K$ .

The simulations are performed in two steps: first of all a simpler case, where only the inconel bar is simulated; then a second case, where the macor cylinder is added. This is done to verify before the experiments the effect of the macor insulant on the thermal history of the inconel bar. Table 4.3 shows the parameters and the configuration of the four cases.

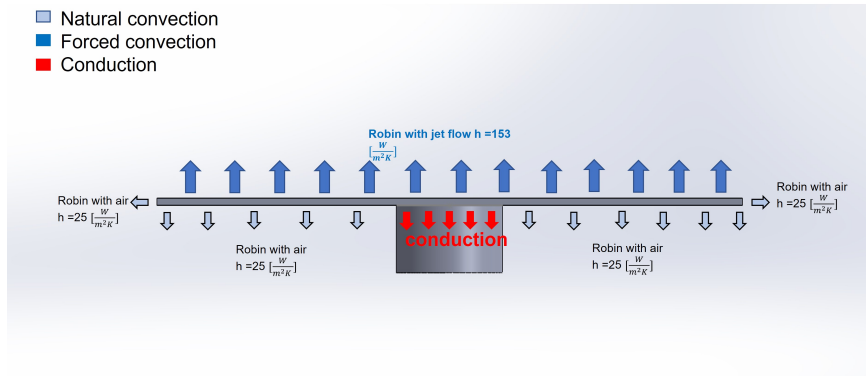
The BCs are applied as shown in figure 4.13. Natural convection condition is added for the remaining sides of the 3D bar and of the macor insulant block. A uniform volumetric heat source ( $Q$ ) is imposed in the inconel bar to model the power provided to the test section by Joule effect.

Several virtual probes are used to retrieve the results of interest from the FEM simulations. The position of the probes is shown in figure 4.14. The heat losses towards the macor are measured by a probe (show in the figure 4.14) at the interface

parameters	values
$T_0$ [°C]	21.65
$T_{amb}$ [°C]	21.65
$\rho_{MA}$ [ $\frac{kg}{m^3}$ ]	2515
$k_{MA}$ [ $\frac{W}{m^2K}$ ]	1.4
$c_{MA}$ [ $\frac{J}{kgK}$ ]	789.3
$\rho_{IN}$ [ $\frac{kg}{m^3}$ ]	7390
$k_{IN}$ [ $\frac{W}{m^2K}$ ]	12
$c_{IN}$ [ $\frac{J}{kgK}$ ]	435
$h_{nc}$ [ $\frac{W}{m^2K}$ ]	25

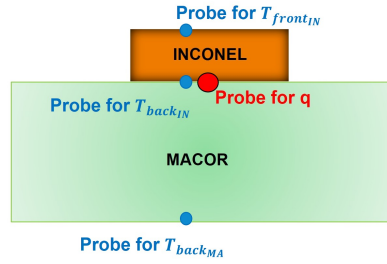
**Table 4.2:** FEM simulation parameters

	configuration	$h_{fc}$ [ $W/m^2K$ ]	$Q$ [ $W/m^3$ ]
<b>Case 1</b>	Inconel	25	$1.667e^6$
<b>Case 2</b>	Inconel	4000	$1.667e^8$
<b>Case 3</b>	Inconel + Macor	153	$1.667e^6$
<b>Case 4</b>	Inconel + Macor	2000	$1.667e^8$

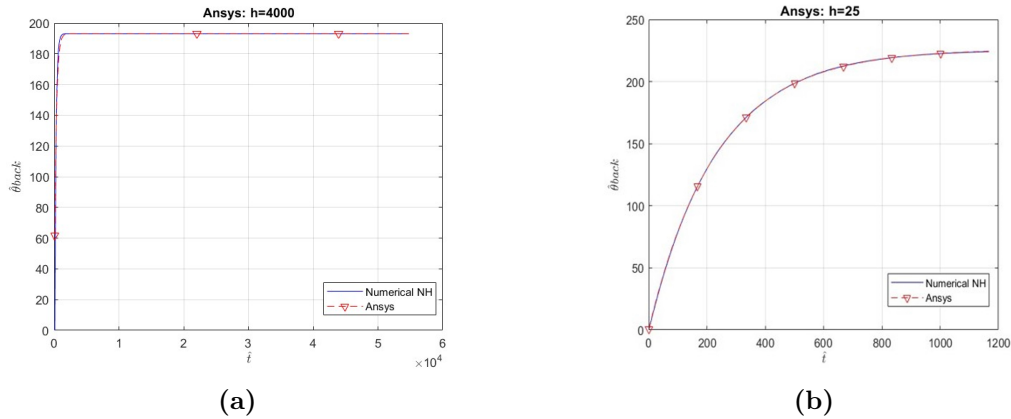
**Table 4.3:** Configuration for FEM simulations

**Figure 4.13:** BC scheme applied to the model used for the FEM simulations

between the macor and the inconel bar. The temperature of the bar is monitored at the top (the wall side cooled by the flow) and at the bottom (the wall side in contact with the macor).

Figure 4.15 shows the comparison between the inverse method and the FEM results, when only the inconel bar is simulated: case 1 and case 2. The comparison proves the correct implementation of the inverse method in term of  $\hat{\theta}$  versus  $\hat{t}$ .



**Figure 4.14:** Probes for heat transfer and temperature values used in the FEM simulations



**Figure 4.15:** ANSYS results Cases 1 (b) and 2 (a) of the 4.3 with NH BC

Figure 4.16 show the comparison between the FEM results and the inverse method for the cases 3 and 4. The difference in  $\hat{\theta}_{back}$  between the two figures consists in the fact that the simulations are done with different source values. The inverse method is run with both homogeneous (H) and non homogeneous (NH) boundary conditions at the bottom side of the inconel bar. Table 4.4 shows how the heat transfer coefficient, predicted by the inverse method, varies as the bottom boundary condition changes. As visible, in the case where h has a larger value (forced convection), a homogeneous BC is acceptable. The errors are calculated by taking as reference the value of h considered in the FEM simulation.

Figures 4.16 show that the transient time predicted by the FEM is greater than the numerical one obtained from solving the PDE and applying the inverse method. This is due to the presence of the macor, which increases the thermal inertia of the system. For this reason, the inverse method is used to optimize both h and  $\alpha$  of the system. The table 4.3 shows how the value of  $\alpha$ , provided by the inverse method, is between the one of inconel and the one of macor, when the simulation is done taking into account both materials. The same conclusion is shown in figure

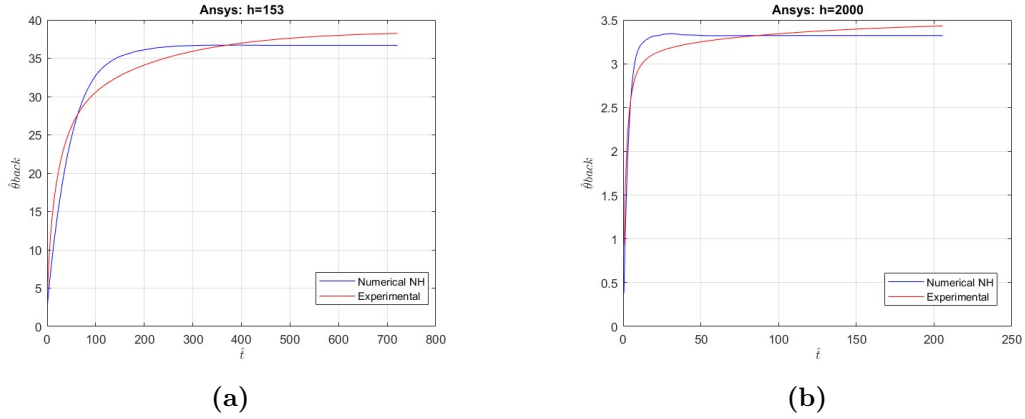


**Figure 4.16:** ANSYS results Cases 3(a) and 4(b) of the table 4.3 with NH BC

ANSYS	$h_{NH}$	Error %	$\alpha_{NH}$	$h_H$	Error %	$\alpha_H$
Case 1	25.91	3.53	$3.34e^{-6}$	25.38	1.5	$3.36e^{-6}$
Case 2	4099.5	2.4	$4.15e^{-6}$	4150.4	3.62	$4.09e^{-6}$
Case 3	130.5	14	$2.08e^{-6}$	165.25	6.2	$1.47e^{-6}$
Case 4	1936.0	3.2	$1.23e^{-6}$	2125.9	5.92	$1.104e^{-6}$

**Table 4.4:** Comparison between Neumann non-homogeneous bottom BC and the homogenous one

4.17. This means that the measurement is affected by the presence of the insulating material. This conclusion can also be derived from the cases in figure 4.17: for the cases with inconel only (1 and 2) the thermal diffusivity from the inverse method is equal to that of inconel. While for the simulations with the macor (3 and 4) the value is included in between the  $\alpha$  of both materials. In the first two cases the inverse method fits the numerical solution obtained from the FEM results perfectly, unlike the other two cases.

Figures 4.18 and 4.20 show the value of the object function in Eq. 2.36 for the cases 3 and 4 respectively at each iteration of the optimization algorithm. This is done using MATLAB 'optimiset' command, which is an options structure that is passed to the optimization function *fminsearch*. It can be noted that after less than 5 iterations for case 3, the minimum value of the objective function (L2 norm) has been found and has a value of 5.8524 K.

Moreover, figures 4.19 and 4.21 show the output variables ( $\hat{\alpha} = \frac{\alpha}{\alpha_{ref}}$  and  $\hat{h} = \frac{h}{h_{ref}}$ ) at the end of the optimization process with  $\alpha_{ref} = 2.8 \cdot 10^{-6} \frac{m^2}{s}$  and  $h_{ref} = 1500 \frac{W}{m^2 K}$ . Both simulations start from dimensionless and unitary values ( $\hat{\alpha} = \hat{h} = 1$ ). For case 4, at the end of the iterations the value of  $h$  is slightly higher than expected

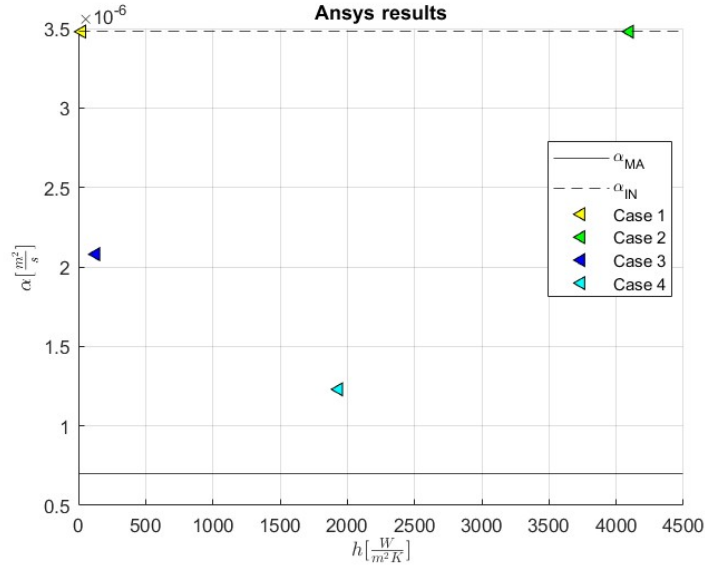


Figure 4.17:  $\alpha$  values from table 4.3

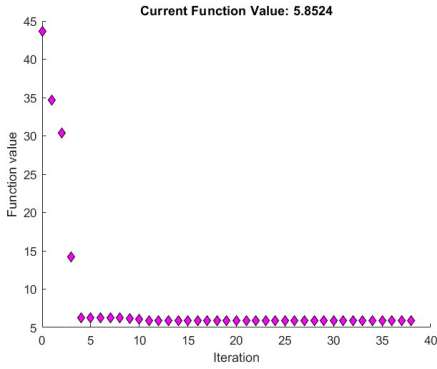


Figure 4.18: Case 4: Object function value at each iteration. Initial guess values  $h = 1500 \frac{W}{m^2K}$  and  $\alpha = 2.8 * 10^{-6} \frac{m^2}{s}$

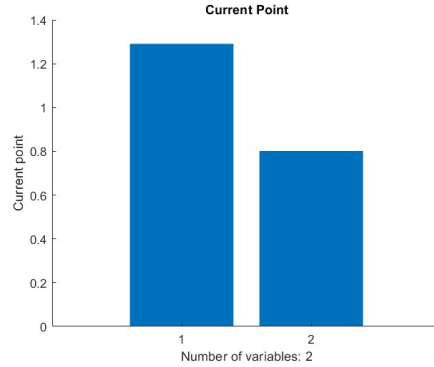
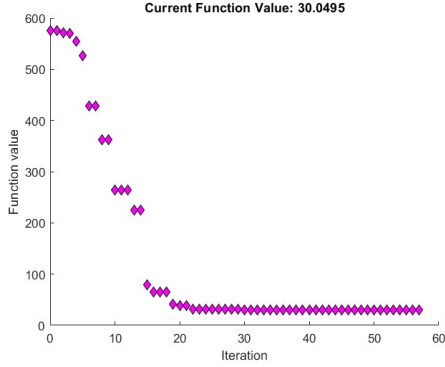


Figure 4.19: Case 4: Final values (shown in the table 4.3) obtained from the optimization process

(value of the bar over the unity), while  $\alpha$  is lower than the initial value. Keeping the same initial guess for the output variables, from the figure 4.21 it is visible that the input  $h$  value is much lower than the initial guess value, unlike  $\alpha$ , which is about the same as the one imposed as input. This means that the  $h$  value is far from the real one imposed in the FEM simulations. In fact, for this case figure 4.20 shows an higher error of the optimization function and it is visible that the error becomes minimal at about the 20th iteration. Instead in figure 4.18, since

the initial guess on  $h$  is close to the real value imposed in the FEM simulations, the error is lower and it drops to almost zero after less than 5 iterations.



**Figure 4.20:** Case 3: Object function value at each iteration. Initial guess values  $h = 1500 \frac{W}{m^2K}$  and  $\alpha = 2.8 * 10^{-6} \frac{m^2}{s}$

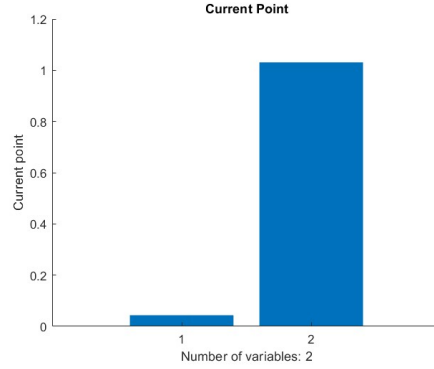


**Figure 4.21:** Case 3: Final values (shown in the table 4.3) obtained from the optimization process

Comparing the thermal diffusivity results, the  $\alpha$  values obtained from case 3 deviate 40% from the inonel value and 66% from the macor value. The case 4 has an  $\alpha$  value far from that of the inonel by 64 % and from the one of the macor by 75%.

## 4.4 Validation of the Inverse Method with experiments

To validate the inverse method, the actual value of  $h$  has been calculated from the experimental apparatus as shown in equation 4.1.

$$h = \frac{q_1}{T_w - T_\infty} \quad (4.1)$$

Moreover,  $T_\infty$  is the jet temperature and  $T_w$  is the front (cooled) temperature of the inconel bar. The thermocouples arrangement is shown in figure 4.22. To calculate the heat transfer coefficient between the inconel bar and the jet flow it is crucial to evaluate the heat transferred from the bar to the jet flow ( $q_1$ ). This can be done using the electrical analogy:

$$q_1 = |q_s| - |q_2| \quad (4.2)$$

where  $q_2$  is the heat lost towards the macor and  $q_s$  is the heat generated by the Joule effect. The value of  $q_2$  is calculated as:

$$q_2 = \frac{k_{MA}}{s_{MA}}(T_{back_{MA}} - T_{back_{IN}}) \quad (4.3)$$

referring to the position of the thermocouples illustrated in Figure 4.22.

The source power  $P$  is calculated as:

$$P = IR^2 \quad (4.4)$$

where  $I$  is the current imposed with the power supply and  $R$  is the electrical resistance of the inconel bar calculated with the second Ohm law. The value of  $q_s$  is then obtained dividing the power by the surface of the inconel bar (33 cm x 6 mm).

It is worth noticing that this method cannot be used in the TROPIC facility because it is not physically possible to insert a thermocouple that measures the wet wall temperature of the inconel bar. This method served only to have experimental values to validate the inverse method.

Comparing the transient time of the raw values of back (4.23) and front (4.24) temperature signals, it is visible that  $T_{front}$  is not affected by the presence of macor, unlike  $T_{back}$ . Moreover, it is possible to see that for low values of flow velocity, the transient time is larger (blue lines). Also, for low velocities the final wall temperature is higher, due to the fact that the heat transfer coefficient is lower.

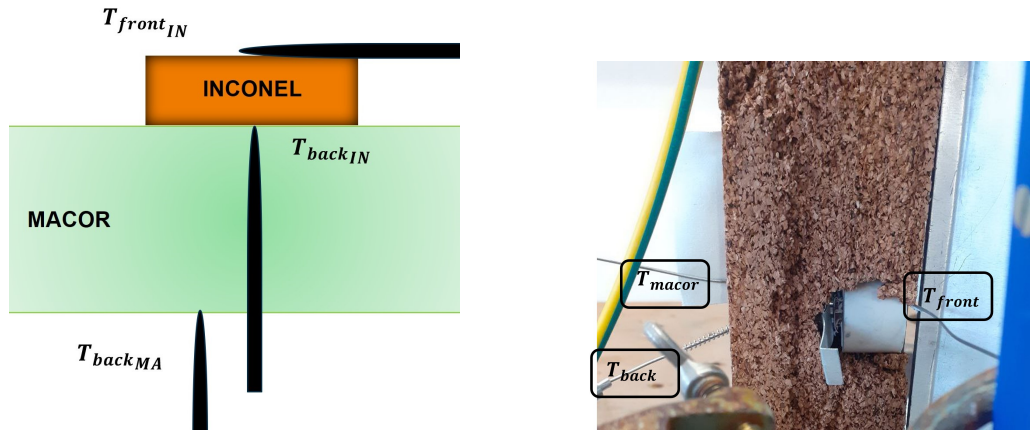


Figure 4.22: Thermocouples arrangement to find  $h$  using direct method

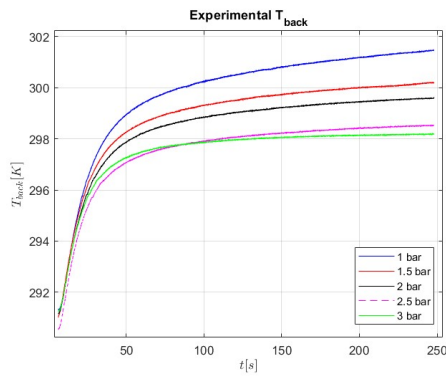


Figure 4.23: Back temperature values from the experimental test cases

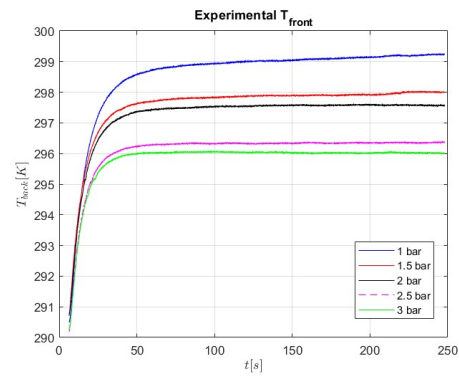


Figure 4.24: Front temperature values from the experimental test cases

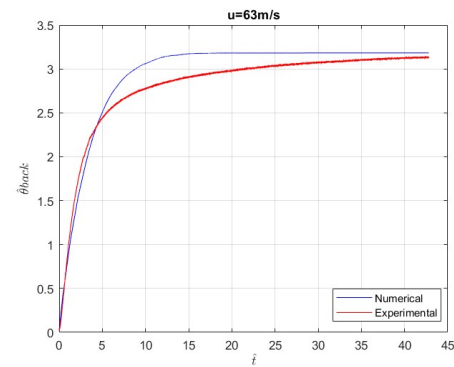
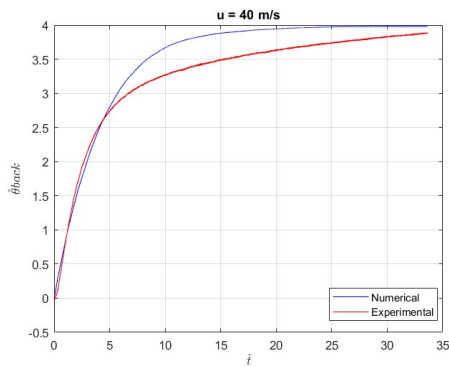
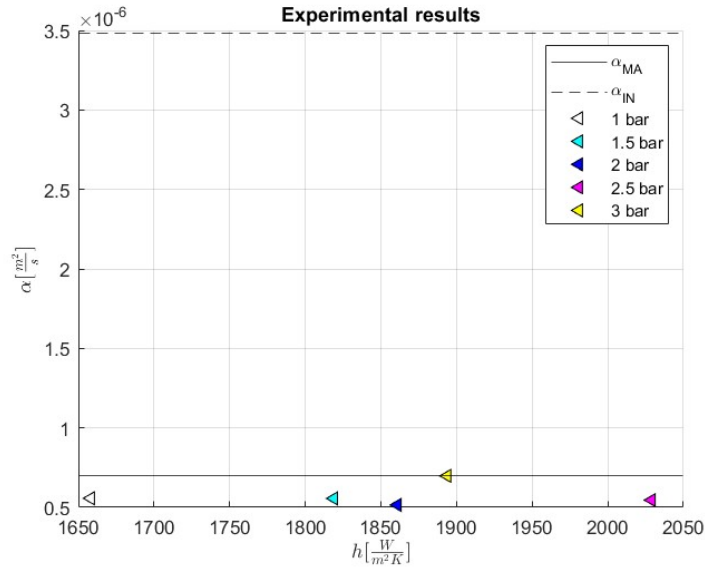


Figure 4.25: Scaled temperature over scaled time for experimental result of  $h$

Table 4.5 shows the comparison between the  $h$  found from the experiments and the results obtained applying the inverse method to the experimental  $T_{back}$  temperature.

The results obtained for  $u = 40\text{m/s}$  and  $u = 63\text{m/s}$  are shown in figure 4.25. Different values of flow velocity yield different heat transfer coefficients. Again, the transient of the experimental solution is slower than the numerical one because the measurements are affected by the presence of the insulator. Also for the experimental cases it is possible to obtain the values of  $\alpha$  calculated by the inverse method and shown in figure 4.26



**Figure 4.26:**  $\alpha$  values obtained from the experimental results after applying the inverse method

<b>u [m/s]</b>	<b>h: Experiment</b>	<b>h: Inverse method</b>	<b>Error [%]</b>
40	1672.67	1658.1	0.87
50	1811.5	1818.8	0.401
58	1812.7	1860.9	2.59
63	1973.7	2028.9	2.72
71	1948.2	1893.8	2.79

**Table 4.5:** Experimental results against the inverse method results in h

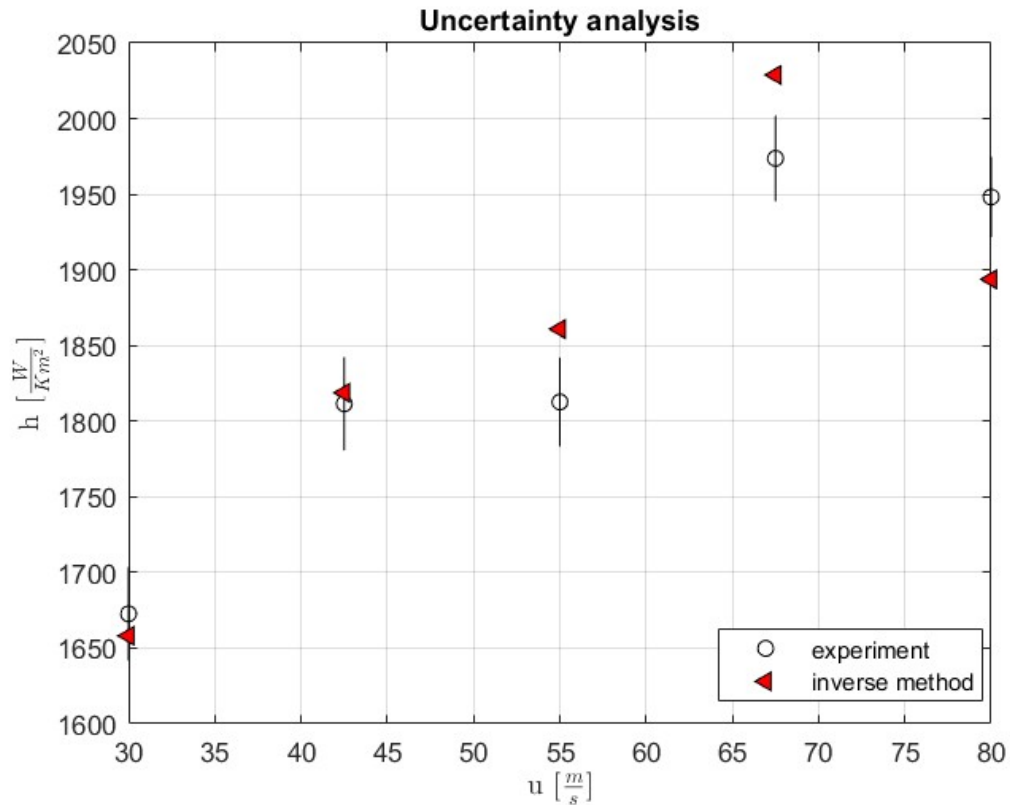


**Figure 4.27:** Experimental  $h$  in function of  $u$  with 68% CI error bars, in comparison with inverse method prediction

A summary of the comparison between the experimental  $h$  and the inverse method output is shown in figure 4.27. The uncertainty on the experimental values is given with 68% confidence interval (CI), assuming a normal distribution of the propagated error. It is visible that only for the first two points the value found by the inverse method is within the uncertainty interval. A 95% confidence interval of the normal distribution yields the results shown in figure 4.28.

The reason why at 3 bar (which correspond to 71 m/s) the value of  $h$  is lower than it should be as it is shown in the experimental values. The heat flux  $q_2$  passing through the macor is more negative than it should be (see the figure 4.29), due to the fact that the  $T_{macor}$  measured experimentally turns out to be higher (eq. 4.3). If the conductive heat turns out to be greater in absolute value, then a greater

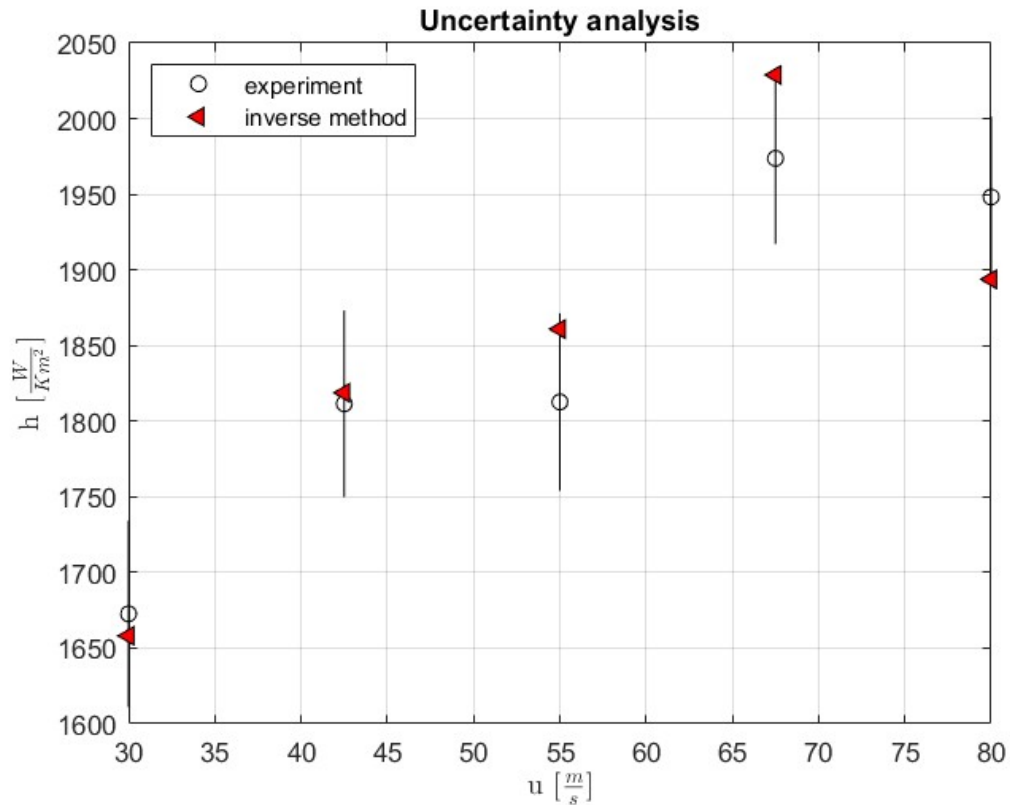


**Figure 4.28:** Experimental  $h$  in function of  $u$  with 95% CI error bars, in comparison with inverse method prediction

value is subtracted from the source. Hence, the convective heat flux  $q_1$  turns out to be less (in equation 4.2) as it is shown in the figure 4.30. This justifies the fact that the experimental value of  $h$  and consequently the value obtained by the inverse method (applied to the experimental results), turn out to be less than desired. This concept has not been investigated, since the purpose of the thesis regards the validation of the inverse method. Nevertheless, the point in question is included in the uncertainty related to the instrument as it is shown in figure 4.28.

According to the correlations listed in Chapter 3 and related to the planar jet nozzle, the relationship between  $Nu$  and  $Re$  is nonlinear, and it is a function of the Reynolds number and the Prandtl number. Figure 4.31 shows that the relation between  $Re$  and  $Nu$ , found by regression, is a power with exponent 0.2788. Since  $Pr$  does not change in these experiments, it is considered as in typical experimental  $Nu$  correlations with the power of 0.4. Thus the final experimental correction is

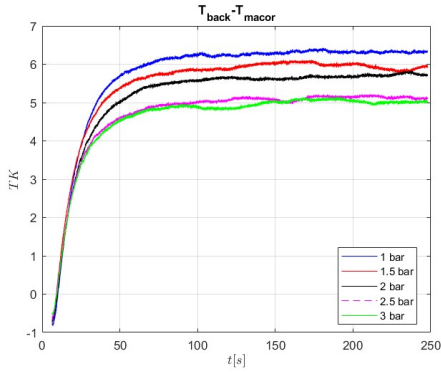


**Figure 4.29:** Experimental difference between the back and macor temperature

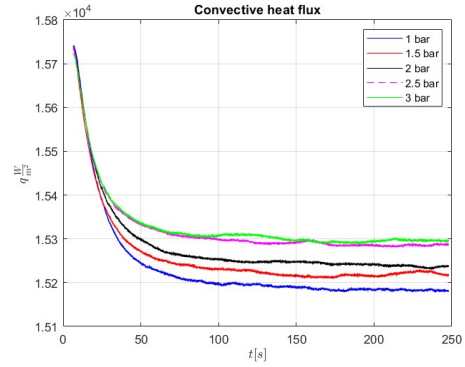


**Figure 4.30:** Convective heat flux 4.2

written in equation 4.5

$$Nu = 19.55Pr^{0.4}Re^{0.2788} \quad (4.5)$$

This result is different from the literature values shown in the figure 3.19 proving that the experimental correlations are closely dependent on the case under consideration.

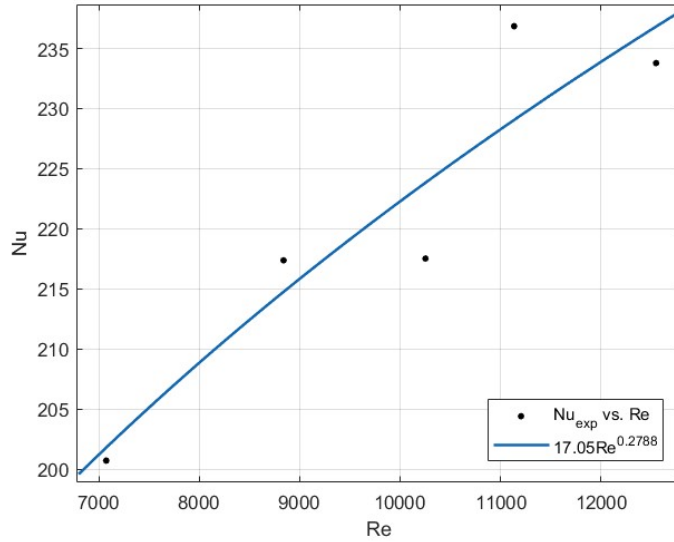


**Figure 4.31:** Experimental correlation between Re and Nu for the planar jet case under consideration

## Chapter 5

# Conclusion and future work

The purpose of this thesis is to develop and validate an inverse method to calculate the heat transfer coefficient between a wall heated by Joule effect and cooled by an impinging jet. The goal is to reproduce in smaller scale the test section of the TROPIC facility at VKI. The design of this test section refers to the cooling system of a combustion chamber of a liquid rocket engine with cooling channels made by additive manufacturing. In the VKI experiments the cooling channel consists of an electrically heated wall and cooled by turbulent ethanol flow. Moreover, the presence of a thick block of insulant material, behind the electrified wall, affects the measurement of the back wall temperature, as studied and proved during this work. This arrangement prevents to evaluate the flow heat transfer coefficient with direct measurement and requires the inverse method developed in this work.

To this end, the 1D transient heat equation is solved both analytically and numerically in dimensionless form. The analytical solution is derived using the method of separation of variables and the solution of the ODE in space is found using the Galerkin projection. The numerical solution featured an implicit time scheme and a second order central scheme for space discretization. A Simplex optimization method is applied to minimize the L2 norm between the value of the inconel back wall temperature, accessible experimentally in the TROPIC test section, and the value obtained by solving the equation. A preliminary sensitivity study showed that the value of  $h$  depends on the heat source value, but not on the heat flux. The solution is very sensitive to the ambient temperature because this influences the velocity of the flow and consequently  $h$ . In fact the most sensitive parameter is  $T_\infty$  as it is shown in table 2.2.

An initial validation of the inverse method is based on transient thermal FEM simulations. The geometry is a simplified version of the experimental test section to assess prior to the experiments the effect of the macor on the thermal history of the inconel bar. The simulations showed that in the cases where macor is present (see figure 4.15) the thermal inertia of the system increases, so it is necessary to include

the value of thermal diffusivity in the optimizer. The first step of the experimental campaign is to understand the effect of the macor on the temperature measurements. It has been shown that having the back thermocouple surrounded by an air chamber allows for a better measurement. In fact, the offset between the  $T_{back}$  and the  $T_{front}$  in a situation of natural convection is smaller. It has also been shown that having the macor glued to the bar allows a more realistic result given the absence of the insulating air layer. Then validation is achieved with experimental results. The experimental test case is a planar air jet ( $7000 \leq Re \leq 13000$ ) impinging on the inconel wall, featuring the same dimensions and material of the TROPIC test section. The local heat transfer coefficient is measured at the jet stagnation point and the inconel bar is heated by Joule effect with constant voltage input.

Future work on the inverse method includes adding bounding values for  $\alpha$ . This is because, as the experimental results show, it makes no physical sense to have a  $\alpha$  value less than the thermal diffusivity of the macor (shown in figure 4.26).

The next step will be to apply the method to VKI's TROPIC facility. In this case, obtaining experimental validation of the method (i.e., calculating  $h$  experimentally) is impossible. So it was necessary to validate the method for a simpler case. For the application of the method to TROPIC experiments, the way the results are acquired, filtered and used by the inverse method could be improved.



# Bibliography

- [1] et Al. S. Soller F. Grauer. «Heat Transfer Phenomena in Additively Manufactured Cooling Channels». In: () (cit. on p. 2).
- [2] Adrian Bejan. *Heat Transfer*. Wiley and Sons, 1993 (cit. on p. 8).
- [3] D A Samoshkin A Sh Agazhanov and Yu M Kozlovskii. «Thermophysical properties of Inconel 718 alloy». In: *Journal of Physics* (2015) (cit. on p. 9).
- [4] Martin Berzins Robert D. Skeel. «A Method for the Spatial Discretization of Parabolic Equations in One Space Variable». In: *Journal on Scientific and Statistical Computing* · (1990) (cit. on p. 13).
- [5] Guido Buresti. «BLUFF-BODY AERODYNAMICS». In: *International Advanced School on WIND-EXCITED AND AEROELASTIC VIBRATIONS OF STRUCTURES* (June 2000) (cit. on p. 36).
- [6] Seyfettin Bayraktar Abdullah Bolek. «HEAT AND FLUID FLOW ANALYSES OF AN IMPINGING JET ON A CUBIC BODY». In: *INTERNATIONAL CONFERENCE ON ENERGY SYSTEMS ISTANBUL* (Dec. 2016) (cit. on p. 36).
- [7] Xiaojun Pa Fangyang Yuan Zhongli Chen. «Simulation of Particle Coagulation and Breakage in a Planar Jet via the DEMM Method». In: *ELVISER* (2015) (cit. on pp. 37, 40).
- [8] R.VISKANTA DT.VADER FP.INCROPERA. «Local convective heat transfer from a heated surface to an impinging, planar jet of water». In: *International Journal of Heat and Mass Transfer* (1991) (cit. on p. 38).
- [9] HOLGER MARTIN. *Heat and Mass Transfer between Impinging Gas Jets and Solid Surfaces*. D 75 Karlsruhe, KaiserstraJe 12, Germany: Institut fur Thermische Verfahrenstechnik der Universitat Karlsruhe ( TH ) 1, 1977 (cit. on p. 38).
- [10] Lianmin Huang and Mohamed S.EL Genk. «Heat transfer of an impinging jet on a flat surface». In: *Pergamon* 37 (Sept. 1993) (cit. on p. 38).

- [11] F. P. INCROPERA D. T. VADER and R. VISKANTA. «Local convective heat transfer from a heated surface to an impinging, planar jet of water». In: *International J. Heat Mass Transfer* (Mar. 1990) (cit. on p. 39).
- [12] Izuru Senaha Seydou Nourou Diop Biram Dieng. «A study on heat transfer characteristics by impinging jet with several velocities distribution». In: *ELVISER* () (cit. on p. 39).
- [13] B. W. WEBB. *Single-Phase Liquid Jet Impingement Heat Transfer*. C.-F. MA (cit. on p. 39).
- [14] J. P. Holman. *Experimental Methods for Engineers*. McGraw-Hill, 2012 (cit. on p. 43).
- [15] Stephanie Bell. *A Beginner's Guide to Uncertainty of Measurement*. National Physical Laboratory, 2001 (cit. on p. 43).



# Appendix A

## Analytical solution development

To find the final analytical solution different steps are used. Here it is possible to find the analytical transient 1D solution of the heat equation with different boundary and initial conditions used to reach the final solution (used in the in the Chapter 2 (2)) with one Robin boundary condition and one Neumann homogeneous boundary condition.

### A.1 1D PDE homogeneous with no source term and homogeneous Neumann BC's in the unit domain and IC=f(x)

The system to solve is

$$\begin{cases} \frac{\partial T(x,t)}{\partial t} = \frac{\partial^2 T}{\partial x^2} \\ \left(\frac{\partial T}{\partial x}\right)_{0,t} = 0 \\ \left(\frac{\partial T}{\partial x}\right)_{1,t} = 0 \\ T(x,0) = x \end{cases} \quad (\text{A.1})$$

Instead of having the Dirichlet boundary conditions fixed to zero, in this problem the boundaries are insulated that means no flux boundary conditions. Assuming that the solution is separable

$$u(x, t) = X(x)T(t)$$

deriving the heat equation in time

$$\frac{\partial T(x, t)}{\partial t} = X(x)\dot{T}(t)$$

and in space

$$\frac{\partial^2 T}{\partial x^2} = X''(x)T(t)$$

substituting this two derivatives to the solution will give

$$X(x)\dot{T}(t) = X''(x)T(t)$$

that means

$$\frac{\dot{T}(t)}{T(t)} = \frac{X''(x)}{X(x)} = \lambda$$

As can be seen, the heat equation (PDE) can be solved with two different ODEs in time and space. Starting from the resolution of the ODE in space, there are three different ways to solve it, depending on the value of  $\lambda$ . It is noted that the relevant case is only the case where  $\lambda = -k_n^2$ . Thus we have

$$X(x) = c_1 \sin(k_n x) + c_2 \cos(k_n x) \quad (\text{A.2})$$

Imposing the boundary conditions show that *if*  $x = 0$   $c_1 = 0$  and *if*  $x = 1$   $\sin(k_n x) = 0$ . This condition leads to  $k_n = n\pi$ . Now, wanting to solve the second ODE in time, we deduce that

$$T(t) = c_3 e^{-k_n^2 t}$$

giving the solution

$$T(x, t) = \sum_{n=0}^{\infty} a_n e^{-k_n^2 t} \cos(k_n x)$$

where  $c_2 c_3 = a_n$ . Using the initial condition gives

$$u(x, 0) = x = \sum_{n=0}^{\infty} a_n \cos(k_n x) = \frac{a_0}{2} + \sum_{n=1}^{\infty} a_n \cos(k_n x)$$

It is possible to recognize that we have a Fourier cosine series and coefficients  $a_0$  and  $a_n$  are chosen such that

$$a_0 = 2 \int_0^1 (x) dx = 1$$

and

$$a_n = 2 \int_0^1 x \cos(k_n x) dx = \frac{2[k_n \sin(k_n) + \cos(k_n) - 1]}{k_n^2}$$

The solution of the PDE is

$$T(x, t) = \frac{1}{2} + 2 \sum_{n=1}^{\infty} \frac{(-1)^n - 1}{k_n^2} e^{-k_n^2 t} \cos(k_n x)$$

## A.2 1D PDE homogeneous with no source term and non homogeneous Neumann BC's in non unit domain with IC

Instead, solving the problem in which the bottom wall is insulated while the top wall is subject to a constant, non-time-dependent heat exchange (meaning heat flux) with the fluid. The system to solve is:

$$\begin{cases} \frac{\partial T(x,t)}{\partial t} = \frac{\partial^2 T}{\partial x^2} \\ \left(\frac{\partial T}{\partial x}\right)_{0,t} = 0 \\ \left(\frac{\partial T}{\partial x}\right)_{L,t} = -\frac{q_{heat\_flux}}{k} \\ T(x,0) = T_0 \end{cases} \quad (A.3)$$

first of all, it is necessary to make the BCs homogeneous by applying the following transformation:

$$T(x, t) = v(x, t) + a(x^2 + 2T) + bx \quad (A.4)$$

This transformation is correct because it causes the starting equation (heat equation) to remain unchanged i.e.

$$\frac{\partial T}{\partial t} = \frac{\partial v}{\partial t} + 2a$$

and

$$\frac{\partial^2 T}{\partial x^2} = \frac{\partial^2 v}{\partial x^2} + 2a$$

so substituting the two expressions for the main equation

$$\frac{\partial T}{\partial t} + 2a = \frac{\partial^2 T}{\partial x^2} + 2a$$

Deriving the transform A.4 drives to

$$\frac{\partial T(x, t)}{\partial x} = \frac{\partial v(x, t)}{\partial x} + 2ax + b$$

and substituting the BCs

$$(1) \quad \frac{\partial T(0, t)}{\partial x} = \frac{\partial v(0, t)}{\partial x} + b = 0 \quad \longrightarrow b = 0$$

and

$$(2) \quad \frac{\partial T(L, t)}{\partial x} = \frac{\partial v(L, t)}{\partial x} + 2aL = -\frac{q_{heat\_flux}}{k} \quad \longrightarrow a = -\frac{q_{heat\_flux}}{2Lk}$$

The transform A.4 becomes

$$T(x, t) = v(x, t) - \frac{q_{heat\_flux}}{2Lk}(x^2 + 2t) \quad (A.5)$$

Then wanting to calculate the new initial conditions for the transformed system

$$v(x, 0) = T(x, 0) + \frac{q_{heat\_flux}}{2Lk}(x^2) = T_0 + \frac{q_{heat\_flux}}{2Lk}(x^2)$$

So the starting system, with non-homogeneous BCs, becomes

$$\begin{cases} \frac{\partial v(x, t)}{\partial t} = \frac{\partial^2 v}{\partial x^2} \\ \left(\frac{\partial v}{\partial x}\right)_{0, t} = 0 \\ \left(\frac{\partial v}{\partial x}\right)_{L, t} = 0 \\ v(x, 0) = T_0 + \frac{q}{2Lk}x^2. \end{cases} \quad (A.6)$$

The resolution of the transformed system is like that of the previous case. The solution of the first ODE is  $X(x) = c_2 \cos(k_n x)$  where this time  $k_n = \frac{n\pi}{L}$ . The solution of the second ODE in time is the same  $T(t) = c_3 e^{-k_n^2 t}$  as it is said before the solution of the transformed system is

$$v(x, t) = \frac{a_0}{2} + \sum_{n=1}^{\infty} a_n e^{-k_n^2 t} \cos(k_n x)$$

coefficients this time, are different due to a different IC. In fact

$$v(x, 0) = T_0 + \frac{q}{2Lk}x^2 = \frac{a_0}{2} + \sum_{n=1}^{\infty} a_n \cos(k_n x)$$

This leads to have

$$a_0 = \frac{2}{L} = \int_0^L (T_0 + \frac{q}{2Lk}x^2) dx = \frac{6T_0 k + Lq_{hf}}{3k}$$

and

$$a_n = \frac{2}{L} = \int_0^L (T_0 + \frac{q}{2Lk}x^2) \cos(k_n x) dx = \frac{2q_{hf}}{Lk k_n^2} (-1)^n$$

By substituting the coefficients found, the solution of the transformed system can be obtained

$$v(x, t) = \frac{a_0}{2} + \sum_{n=1}^{\infty} a_n e^{-k_n^2 t} \cos(k_n x)$$

To obtain the solution of the starting system, it is enough to apply the transformation A.5 which leads to

$$T(x, t) = v(x, t) - \frac{q_{hf}}{2Lk}(x^2 + 2t)$$

### A.3 1D PDE non-homogeneous with no source term and non homogeneous Neumann BC's in non unit domain with a constant IC

In this case the thermal diffusivity is taken into account and the heat equation is no longer linear

$$\begin{cases} \frac{\partial T(x,t)}{\partial t} = \alpha \frac{\partial^2 T}{\partial x^2} \\ \left(\frac{\partial T}{\partial x}\right)_{0,t} = 0 \\ \left(\frac{\partial T}{\partial x}\right)_{L,t} = -\frac{q_{hf}}{k} \\ T(x,0) = T_0 \end{cases} \quad (\text{A.7})$$

In this case the transform becomes

$$u_2(x,t) = T(x,t) - u_1(x,t) \quad (\text{A.8})$$

where

$$u_1(x,t) = \frac{-\frac{q_{hf}}{k}}{2L}x^2 + \frac{c^2(-\frac{q_{hf}}{k})t}{L} = -\frac{q_{hf}}{kL} \left( \frac{x^2}{2} + c^2t \right) \quad (\text{A.9})$$

Wanting to obtain the transformed system and starting from the IC

$$u_1(x,0) = -\frac{q_{hf}}{kL}x^2$$

this lead to have

$$u_2(x,0) = T_0 + \frac{q_{hf}}{kL}x^2$$

and the system A.7 changes into

$$\begin{cases} \frac{\partial u_2(x,t)}{\partial t} = \alpha \frac{\partial^2 u_2}{\partial x^2} \\ \left(\frac{\partial u_2}{\partial x}\right)_{0,t} = 0 \\ \left(\frac{\partial u_2}{\partial x}\right)_{L,t} = 0 \\ u_2(x,0) = T_0 - u_1(x,0) = T_0 - \frac{q_{hf}}{kL}x^2 \end{cases} \quad (\text{A.10})$$

In this case the spatial ODE remains the same ( $X(x) = c_1 \cos(k_n x)$ ), while the temporal ODE is transformed as follows

$$\dot{T}_n(t) = -\alpha k_n^2 T_n(t)$$

Then applying the Fourier cosine series transformation,

$$\sum_{n=0}^{\infty} \dot{T}_n(t) \cos(k_n x) = \sum_{n=0}^{\infty} -\alpha k_n^2 T_n(t) \cos(k_n x)$$

and calling the term  $-\alpha k_n^2 = \lambda_n$  the solution of the second ODE is

$$u_2(x, t) = \frac{a_0}{2} + \sum_{n=1}^{\infty} a_n e^{-\lambda_n^2 t} \cos(k_n x) \quad (\text{A.11})$$

Again to find the value of the coefficients it is important to consider the IC

$$u_2(x, 0) = T_0 + \frac{q_{hf}}{kL} x^2 = \frac{a_0}{2} + \sum_{n=1}^{\infty} a_n \cos(k_n x)$$

Where

$$a_0 = \frac{2}{L} \int_0^L (T_0 + \frac{q}{2Lk} x^2) dx = \frac{6T_0k + Lq_{hf}}{3k}$$

and

$$a_n = \frac{2}{L} \int_0^L (T_0 + \frac{q}{2Lk} x^2) \cos(k_n x) dx = \frac{2q_{hf}}{Lk k_n^2} (-1)^n$$

The solution of the transformed system A.10 will become A.11. Now to return to the equation of the original system A.7 the application of the equation A.8 is important. The solution takes the form

$$T(x, t) = -\frac{q_{hf}}{kL} \left( \frac{x^2}{2} + c^2 t \right) + \frac{a_0}{2} + \sum_{n=1}^{\infty} a_n e^{-\lambda_n^2 t} \cos(k_n x)$$

## A.4 1D PDE non-homogeneous with a constant source term, one homogeneous Neumann BC, one homogeneous Dirichlet BC in non unit domain with a constant IC

In this case, it is considered to have a thermally insulated base while the upper surface of inconel has a constant temperature equal to zero. The system to solve is

$$\begin{cases} \frac{\partial T(x,t)}{\partial t} = \alpha \frac{\partial^2 T}{\partial x^2} + \alpha \frac{\dot{q}_s}{\lambda} \\ \left( \frac{\partial T}{\partial x} \right)_{0,t} = 0 \\ (T)_{L,t} = 0 \\ T(x,0) = T_0 \end{cases} \quad (\text{A.12})$$

It is noted that by doing the dimensional study for the heat equation, the heat source  $\dot{q}_s$  is volumetric with dimensions  $W/m^3$ . This case is similar to the previous one, the only difficulty consist in the expression of the source term as a Fourier series. The solution of the PDE with separable variables is of the type

$$T(x, t) = \sum_{n=0}^{\infty} X_n(x) T_n(t) \quad (\text{A.13})$$

This leads to a new form for the main equation of the heat transfer which becomes

$$\sum_{n=0}^{\infty} X_n \dot{T}_n = \sum_{n=0}^{\infty} \alpha X_n'' T_n + \sum_{n=0}^{\infty} \alpha \frac{\dot{q}_s}{\lambda}$$

As mentioned above, two ODEs must be solved. Starting with the spatial one

$$\frac{X_n''}{X_n} = -k_n^2$$

where the general solution is

$$X_n(x) = c_1 \sin(k_n x) + c_2 \cos(k_n x)$$

Substituting the BCs it is possible to have

$$X_n'(0) = c_1 k_n = 0 \quad \longrightarrow \quad c_1 = 0$$

$$X_n(L) = c_2 \cos(k_n L) = 0 \quad \longrightarrow \quad k_n = \frac{n\pi}{2L}$$

The solution of the first PDE is

$$X_n(x) = c_2 \cos(k_n x) \tag{A.14}$$

Instead, this time the solution in the temporal ODE must take into account the source

$$\dot{T}_n(t) = -c^2 T_n(t) + q_n$$

where  $c^2 = \alpha k_n^2$ ,  $q_n$  is the value of the Fourier transform for the source that could have the form

$$q_n = \frac{2}{L} \int_0^L \frac{\dot{q}_s \alpha}{\lambda} \cos(k_n x) dx = \frac{2\alpha \dot{q}_s}{L k_n \lambda} (\sin(k_n L))$$

This case is a constant coefficient Linear Differential Equations with a constant input witch leads to this type of solution

$$T_n(t) = \left( \frac{q_n}{c^2} + b_n e^{-c^2 t} \right) \tag{A.15}$$

Now substituting the A.14 and A.15 in A.13 and calling  $c_n = \frac{q_n}{c^2} + b_n$  the solution become

$$T(x, t) = \sum_{n=0}^{\infty} c_n e^{-c^2 t} \cos(k_n x)$$

Where  $c_n$  could be find from the IC

$$T(x, 0) = T_0 = \sum_{n=0}^{\infty} c_n \cos(k_n x)$$

and then

$$c_n = \frac{2}{L} \int_0^L T_0 \cos(k_n x) = \frac{2T_0 \sin(k_n L)}{L k_n}$$

### Steady state solution

To verify that the analytical solution is correct, it has to converge to the stationary solution at the end of the transient. This also served to calculate the duration of the transient. The steady state solution is found from the main heat equation

$$\frac{1}{\alpha} u_t = u_{xx} + \frac{\dot{q}_s}{\lambda}$$

Deriving twice

$$u(x) + \frac{\dot{q}_s}{\lambda} \frac{x^2}{2} + c_1 x + c_2 = 0 \quad (\text{A.16})$$

Substituting the BCs

$$x = 0 \quad \frac{\dot{q}_s x}{\lambda} + c_1 = 0 \quad \longrightarrow \quad c_1 = 0$$

and

$$x = L \quad u(L) + \frac{\dot{q}_s L^2}{2\lambda} + c_2 = 0 \quad \longrightarrow \quad c_2 = -u(L) - \frac{\dot{q}_s L^2}{2\lambda}$$

Then the steady state solution will be as A.16 with new coefficients

$$u(x) = u(L) + \frac{\dot{q}_s L^2}{2\lambda} (L^2 - x^2)$$

## A.5 pdpede Solution process

To solve PDEs with *pdepe* function is important to define the equation coefficients  $c, f$  and  $s$ , the initial conditions, the boundary conditions and a mesh of point you would like to use to evaluate the solution on. The solution works in this way:

$$sol = pdepe(m, @heatpde, @heatic, @heatbc, x_s, t_s) \quad (\text{A.17})$$

where *@heatpde* is the function handle that defines the main equation being solved. The *@heatic* is the function handle in which used for the initial condition and is depending only on spatial variable; this means that at the initial time  $t = t_0$  for all the space points, the solution components satisfy the initial condition of the form:

$$u(x, t_0) = u_0 \quad (\text{A.18})$$

The `@heatbc` is the function handle which works as mentioned in the equations (2.35). Note that over two coefficients  $p(x, t, u)$  and  $q(x, t)$  only  $p$  could depend on the solution  $u$ . This function using two coefficients  $q$  and  $p$  for both side: left and right.



# Appendix B

## Calibration of instruments

### B.1 Hot wire calibration

The static calibration has the purpose to compare the voltage with the pressure from the jet. The first thing to do is to connect the probe to the anemometer and follow the power-up procedure specific to each model ( VKI's Guidelines for the instrument shown in the figure B.1 was used for this case). Then, being in the 'hot wire' condition, it is possible to set the anemometer once its resistance is also set to zero.

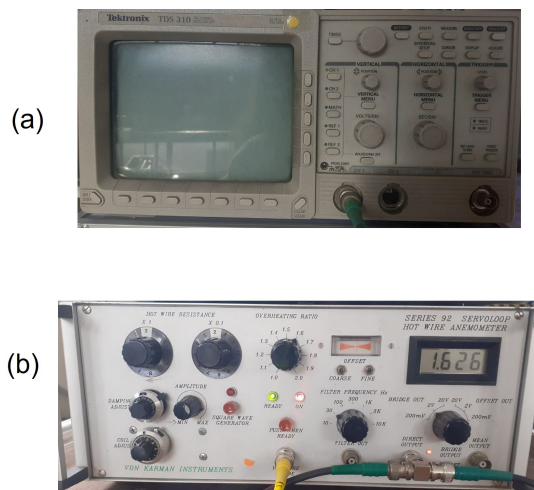


**Figure B.1:** Oscilloscope(a) and anemometer (b)

The calibration nozzle is used to calibrate the probe (hot wire) because it has a special geometry that allows the maximum output pressure to match the 10 V, maximum voltage of the validyne. Noting this, for each upstream pressure,

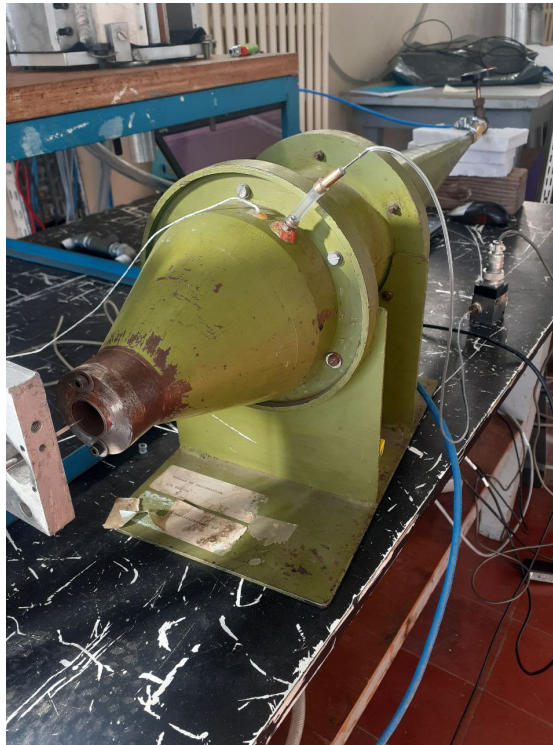


**Figure B.2:** Calibration nozzle

a voltage from the validyne was obtained. Hence, using the calibration curve of the pressure transducer, a precise value of pressure corresponds to each voltage. Knowing the pressure and assuming that the flow is incompressible, it is possible to apply Bernoulli's equation between the inlet and the outlet of the nozzle. This leads to calculate the value of the exit velocity (all the setup it is shown in the figure B.2).

The calibration curve (shown in the figure B.3) is a third-order polynomial between the exit velocity, found from Bernoulli's equation and the recorded voltage of the hot wire acquired by exposing the probe to the flow. Once the probe is calibrated, it can no longer be disconnected.

## B.2 Validyne calibration

Calibration of the pressure transducer (validyne) is done using a special calibrator (component (a) in the figure B.4), which is connected to the validyne (b), which is linked to an interface (LabVIEW (d)), via a demodulator (c). The use of the calibrator allowed a known pressure to be applied to the validyne. Therefore,

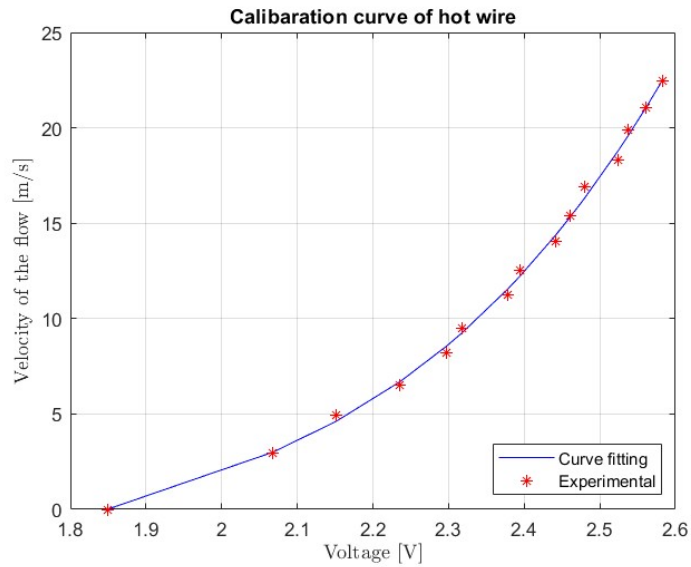


**Figure B.3:** Hot wire calibration curve

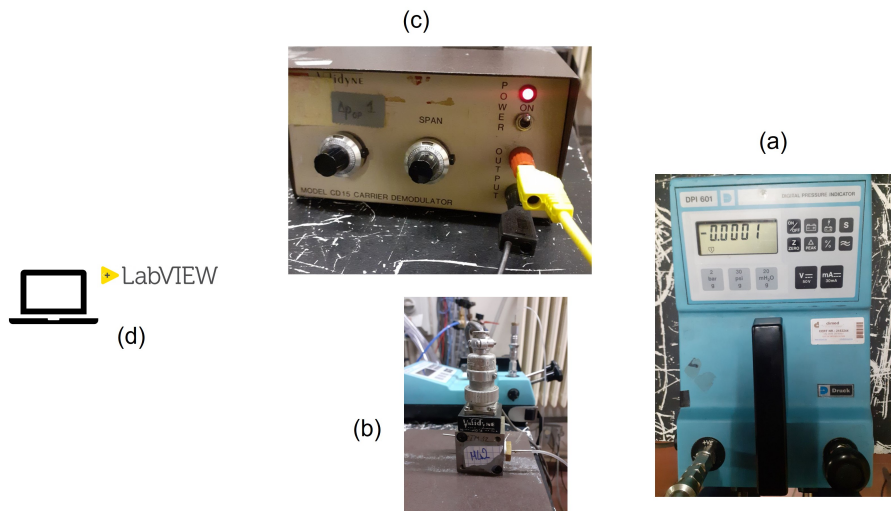


**Figure B.4:** Instruments used for the validyne calibration

the calibration is done by matching a range of pressure values, the range of the potential difference between 0 and 10 Volts. Specifically, the first two values set were the extremes of the range. These are found by adjusting the clock and zero (two clockwise valves) on the demodulator. Hence, the minimum pressure value applicable by the calibrator (0 bar) is linked to 0 V; while the maximum pressure value (acceptable by the validyne membrane) is linked to the value of 10

V. Having accurately set the zero and the maximum allowable value and using different pressures (within the range) via the calibrator, it is possible to record the corresponding volts read on LabVIEW. In this way, the calibration curve can be obtained (see B.5).

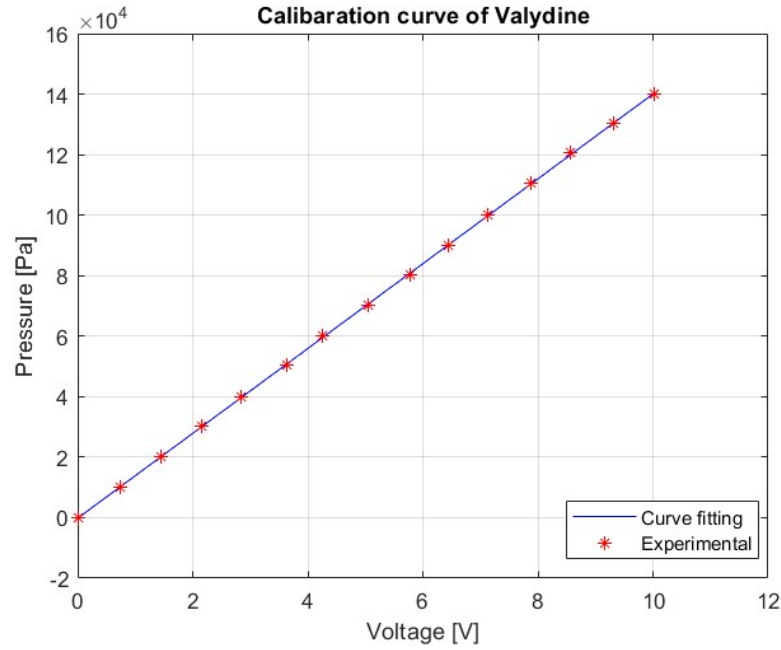


Figure B.5: Valdyne calibration curve

### B.3 Thermocouples calibration

Thermocouple calibration is done using the oil bath (see figure B.6 on the right side). This system allows a certain temperature to be set analogically. Then it is very important to wait for the time needed to stabilize a certain temperature, and then insert a probe called PT100 (figure B.6 on the left side) to make sure that the value shown on the oil bath screen is consistent with the value read by the probe. Thermocouples are inserted to be calibrated. Not only the temperature read by the PT100 is noted, but also the temperature read by the thermocouples. The same process is performed for different temperature values. Then the calibration curve is obtained by linearly interpolating the temperature values read by the probe PT100 and those for the individual thermocouple. The calibration is successful if the line obtained corresponds to the bisector (as shown in the figure B.7).

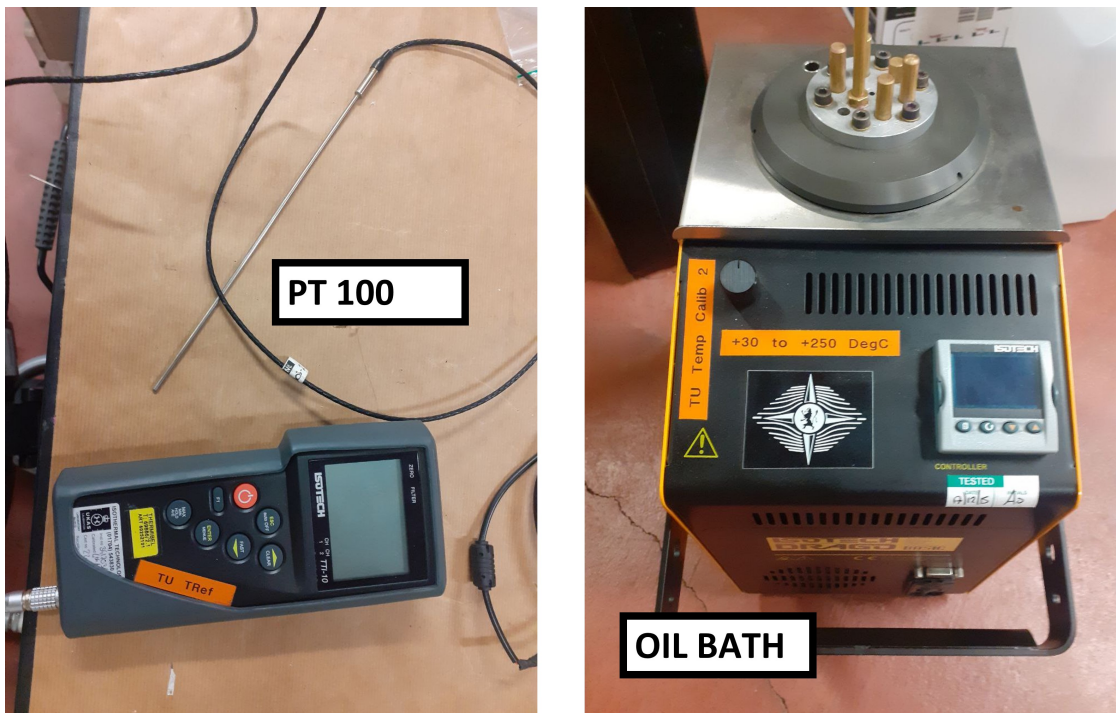


Figure B.6: Instruments used for thermocouple calibration

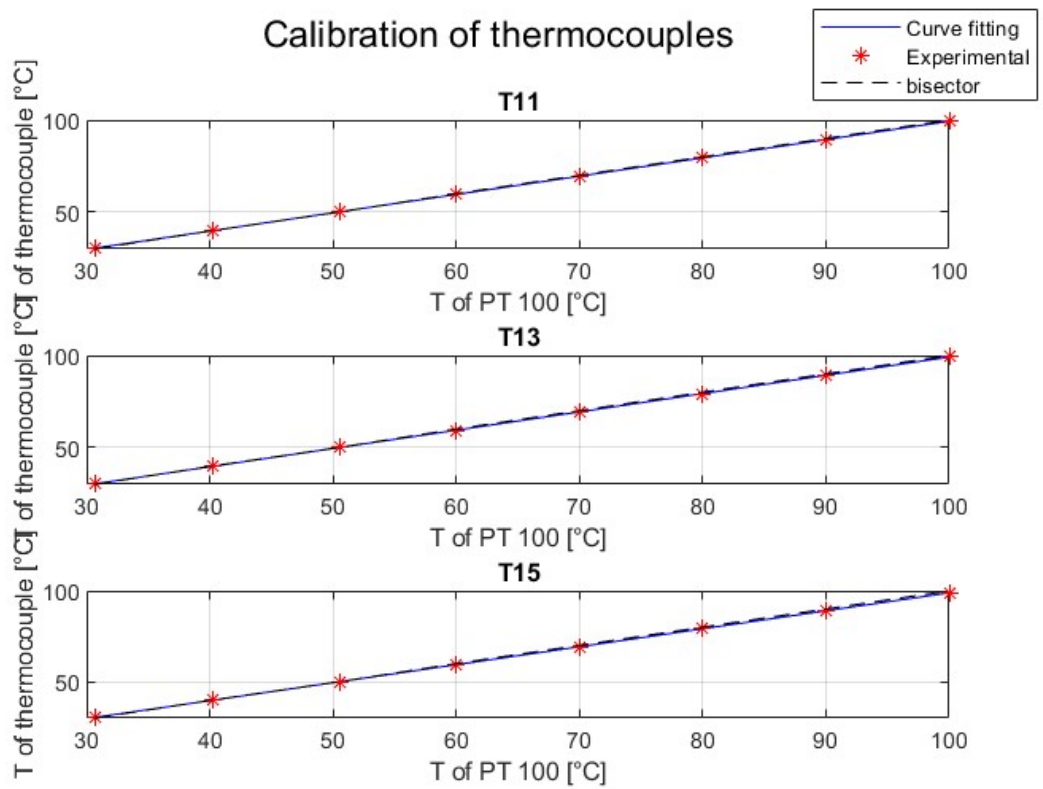


Figure B.7: Thermocouples calibration curve

# Appendix C

## MATLAB code

In this chapter the main codes used is reported.

### 1D Analytical solution

```
1 L = 2*10^-3; %thickness [m]
2 tend = 1400; % numerical time [s]
3 x = linspace(0,L,1400)'; % space vector
4 t = linspace(0.1,tend,1400)'; % time vector
5 T0 = 20+273.15 ; % ambient temperature
6 lambda= 12; % thermal conductivity of
   the matherial [W/m*K]
7 alpha = 3*10^-6; % thermal diffusivity [m^2/s]
   ]
8 Q = 31 ; % heat source [W]
9 Vol = 3.96*10^-6; % volume of the bar [m^3]
10 qs = Q/(Vol); % volumetric heat source
11 h= 2000; % heat transfer coefficient
   [W/m^2 K]
12
13 trif = (L^2)/alpha; % time reference
14 DeltaT = qs*trif*alpha/lambda;
15 Nu = h*L/lambda; % Nusselt number
16 T_inf = 16+273.15; % Jet temperature [K]
17 theta0 = (T0-T_inf)/DeltaT; % scaled initial temperature
18
19 x_adim = x./L; % scaled space variable
20 t_adim = t./(trif); % scaled time variable
21
```

```

22 fun=@(xkn) tan(xkn)-(Nu/xkn); % function used to find the
    eigenvalues
23 soluz = @(xx,tt) 0*xx.*tt;
24 for n=1:100
25     x0 = (pi*(n-1)) + eps;
26     kn = fsolve(fun,x0);
27     qn = 4*((sin(kn))/(sin(2*kn)+(2*kn)));
28     cn = (4*theta0*(sin(kn)))/(sin(2*kn)+(2*kn));
29     bn = cn -(qn/(kn^2));
30     usol=@(xx,tt) ((qn/(kn^2))+(bn*exp(-(kn^2).*tt)).*cos
(kn*xx));
31     soluz = @(xx,tt) soluz(xx,tt)+usol(xx,tt);
32 end
33 % soluz in the temperature solution in fuction of time and
    space :T(x,t)
34 theta = (-(x_adim.^2)/2)+(1/Nu)+(0.5); % scaled
    steady state solution
35 T = DeltaT*soluz(x_adim,t_adim(end))+T_inf; % Solution
    for each x and final time
36 T_steady = DeltaT*theta +T_inf; % Steady
    state temperature

```

### 1D Numerical solution with Experimental/Ansys case

```

1
2 global h0 % heat transfer coefficient
    [W/m^2 K]
3 global T0 % inital temperature of the
    body [K]
4 global lambda % thermal conductivity of
    macor [W/mK]
5 global T_inf % temperature of the jet or
    of the surroundings [K]
6 global q % heat flux through the
    Macor [W/m^2]
7 global time % simulation time
8 global alpha % thermal diffusivity [m^2/s]
9 global Q_source % heat source [W]
10 global Tback_history % back temperature from the
    expermental case
11 global m % Symmetry constant for
    cartesia coord
12 global L % thickness [m]

```

```
13 global tend % numerical time
14 global y % mesh in space
15
16 %%% Germetry's data
17
18 Vol = (2*10^-3)*(33*10^-2)*(6*10^-3); % bar volume [m
    ^3]
19 Q_source = (31/(Vol));
20 lambda = 12;
21 L = 0.002;
22 tend = 100;
23 y = linspace(0,L,tend)';
24 m = 0;
25
26 %%% ANSYS DATA
27
28 aa = importdata("10_03_h2000\Inconel Top.txt"); % read the
    file related to the test
29 T_front = aa.data(:,3)+273.15; % Top
    experimental temperature
30 ee = importdata("10_03_h2000\Inconel Bottom.txt");
31 Tback_history = ee.data(:,3)+273.15;
32 T_inf = 16+273.15;
33 T0 = Tback_history(1,1);
34 cc = importdata("10_03_h2000\Heatflux.txt");
35 q = -cc.data(:,5);
36 time = cc.data(:,2);
37
38 %%% Inverse method
39
40 x0 = [2 1]; % initial
    guess vector
41 options = optimset('PlotFcns',@optimplotfval); % error
    plot
42 %options = optimset('PlotFcns',@optimplotx); % plot of
    changing output values
43 [x,e] = fminsearch(@func,x0,options) % inverse
    method function
44
45 function [e] = func(x)
46     global h0
47     global alpha
48     global time
49     global Tback_history
50     global m
```

```

51 global L
52 global tend
53 global y
54
55 h0 = x(1)*1000;
56 alpha = x(2)*(3.6e-06);
57 sol = pdepe(m,@heatpde,@heatic,@heatbc,y,time); %
numerical solution
58 e = norm(sol(:,1)-Tback_history,2); % norm
of the difference
59 end

```

Functions used from the pdepe solver are

```

1
2 %%% describing the main equation
3 function [c,f,s] = heatpde(y,time,u,dudy)
4
5 global lambda
6 global alpha
7 global Q_source
8 c = 1/alpha;
9 f = dudy;
10 qs = Q_source;
11 s = qs/(lambda);
12
13 end
14
15 %%% describing the boundary conditions
16 function [pl,ql,pr,qr] = heatbc(yl,ul,yr,ur,time)
17 global h0
18 global lambda
19 global T_inf
20 global q
21 global time
22
23 %%% Top BC
24 pr = ((h0)*(ur - (T_inf))) ; % Robin boundary
condition
25 qr = lambda;
26
27 %%% bottom BC

```

```

28     for i=1:size(q)
29         p1 = -q(i);           % Neumann non-homogeneous
30         %p1 = 0;             % Neumann homogeneous
31     end
32     ql = lambda;
33 end
34
35 %% describing the initial conditions
36 function u0 = heatic(y)
37     global T0
38     u0 = T0;
39 end

```

## 2D Numerical solution

```

1  Ly = 2*10^-3;           % tickness of the bar [m]
2  Lz = 33*10^-2;         % third dimension [m]
   used alternatively
3  Lx = 6*10^-3;         % second dimension [m]
   used alternatively
4  alpha = 7*10^-7;      % thermal diffusivity of
   the material [m^2/s]
5  lambda = 12;          % thermal conductivity of
   the matherial [W/m*K]
6  T_inf = 16+273.15;    % Jet temperature [K]
7  T0 = 20+273.15;      % Ambient temerature [K]
8  h = 2000;            % heat flux coefficient [
   W/m^2 K]
9  Q = 31;               % heat source [W]
10 Vol = 3.96*10^-6;    % volume of the bar [m^3]
11 qs = Q/(Vol);        % volumetric heat source
   [W/m^3]
12
13
14 thermalmodel = createpde("thermal","transient-axisymmetric")
   ; % call the model
15 g = decsg([3 4 0 0.006 0.006 0 0 0 0.002 0.002]');
   % create a geometry for 6mmx2mm
16 g = decsg([3 4 0 0.33 0.33 0 0 0 0.002 0.002]');
   % create a geometry for 33cmx2mm

```

```

17 geometryFromEdges(thermalmodel,g);
18
19 %% %Plot the geometry.
20 figure (1)
21 pdegplot(thermalmodel,'EdgeLabels','on',"FaceAlpha",0.5);
22 grid on
23 title 'INCONEL 718 Geometry ';
24
25 %%%thermal properties
26 thermalProperties(thermalmodel,"ThermalConductivity",12,...
27                 "MassDensity",8442 ,...
28                 "SpecificHeat",402);
29
30 %%%% boundary conditions
31
32 coeff = h/lambda;
33 upBC = @(~,state) -coeff.*(state.u - T_inf); % Top Robin BC
34
35 %%% Case a
36
37 % thermalBC(thermalmodel,"Edge",3,"HeatFlux",upBC);
38 % thermalBC(thermalmodel,"Edge",[1,2,4],'HeatFlux',0,'
    Vectorized','on');
39
40 %%%% Case b
41 % coeff2 = 25/lambda;
42 % sideBC = @(~,state) -coeff2.*(state.u - T0);
43 %
44 % thermalBC(thermalmodel,"Edge",3,"HeatFlux",upBC);
45 % thermalBC(thermalmodel,"Edge",[2,4],"HeatFlux",sideBC);
46 % thermalBC(thermalmodel,"Edge",1,'HeatFlux',0,'Vectorized
    ','on');
47
48 %%% Case c
49 % coeff2 = 25/lambda;
50 % sideBC = @(~,state) -coeff2.*(state.u - T0);
51 %
52 % thermalBC(thermalmodel,"Edge",3,"HeatFlux",upBC);
53 % thermalBC(thermalmodel,"Edge",2,"HeatFlux",sideBC);
54 % thermalBC(thermalmodel,"Edge",[1,2],'HeatFlux',0,'
    Vectorized','on');
55
56 %%%% initial conditions
57 thermalIC(thermalmodel,T0); % uniform room temperature in
    the rod is T0

```

```

58
59 % % % constant internal source
60 internalHeatSource(thermalmodel,qs/lambda,"Face",1);
61 %%% mesh definition
62 msh = generateMesh(thermalmodel,"Hmax",Ly/3);
63 tfinal = 1400;
64 tlist = linspace(0,tfinal,1400);
65 x = linspace(0,Lx,length(tlist));
66 y = linspace(0,Ly,length(tlist));
67 result = solve(thermalmodel,tlist);
68 T = (result.Temperature); % solve and find the
    solution T(x,y,t)
69
70
71 %%%%% PLOT
72 figure(1)
73 colorbar
74 pdeplot(thermalmodel,"XYData",T(:,1),"ColorMap",'hot',"
    XYGrid","off")
75 title(sprintf("Temperature at %g s",tlist(1)))
76 xlabel('Length [m]','interpreter','latex')
77 ylabel('Thickness [m]','interpreter','latex')
78 xlim([0 0.35]);
79 ylim([0 0.002]);
80
81 figure(2)
82 colorbar
83 pdeplot(thermalmodel,"XYData",T(:,end),"ColorMap",'hot',"
    XYGrid","off")
84 title(sprintf("Temperature at %g s",tlist(end)))
85 xlabel('Length [m]','interpreter','latex')
86 ylabel('Thickness [m]','interpreter','latex')
87 xlim([0 0.35]);
88 ylim([0 0.002]);
89
90 Y=y; % for each y
91 X = (0)*ones(size(Y)); % want the solution on
    1 x. this case x=0
92 Tintrp = interpolateTemperature(result,X,Y,1:length(tlist));
93
94 figure(3)
95 colormap hot
96 imagesc(tlist,flip(y),Tintrp(:,:,:)')
97 colorbar
98 grid on

```

```
99 xlabel('time [s]')
100 ylabel('Thickness [m]')
101 title('2D solution x=0')
102 hold off
103
104 X1 = (Lx/2)*ones(size(Y)); % want the solution
    on 1 x. this case x=Lx/2
105 Tintrp1 = interpolateTemperature(result,X1,Y,1:length(tlist)
    );
106
107 figure(4)
108 colormap hot
109 imagesc(tlist,flip(y),Tintrp1(:,:,:)')
110 colorbar
111 grid on
112 xlabel('time [s]')
113 ylabel('Thickness [m]')
114 title('2D solution x=Lx/2')
115 hold off
116
117 X2 = (Lx)*ones(size(Y)); %want the solution on
    1 x. this case x=Lx
118 Tintrp2 = interpolateTemperature(result,X2,Y,1:length(tlist)
    );
119
120 figure(5)
121 colormap hot
122 imagesc(tlist,flip(y),Tintrp2(:,:,:)')
123 colorbar
124 grid on
125 xlabel('time [s]')
126 ylabel('Thickness [m]')
127 title('2D solution x=Lx')
128 hold off
129
130
131 % time t=end (primo dopo t=0)
132 Tprint1_3 = interpolateTemperature(result,X,Y,1400); %
    questo xk a length(t)=10000
133 Tprint2_3 = interpolateTemperature(result,X1,Y,1400);
134 Tprint3_3 = interpolateTemperature(result,X2,Y,1400);
135 figure(6)
136 plot(Y/Ly,Tprint1_3(:,:,:)/T_inf,'--r','Marker','v','
    MarkerIndices',1:53:length(Y))
137 hold on
```

```
138 grid on
139 plot(Y/Ly,Tprint2_3(:,:,:)/T_inf,'b')
140 plot(Y/Ly,Tprint3_3(:,:,:)/T_inf,'k:','Marker','o','
    MarkerIndices',1:133:length(Y))
141 plot(Y/Ly,sol(1400,:)/T_inf,'g')
142 plot(Y/Ly,T_steady/T_inf,'-.k')
143 legend('2D x=0 m','2D x=Lx/2','2D x=Lx','1D','Steady')
144 xlabel('$y/L_y$', 'Interpreter','latex')
145 ylabel('$T/T_{jet}$', 'Interpreter','latex')
146 title('Case 1b')
```